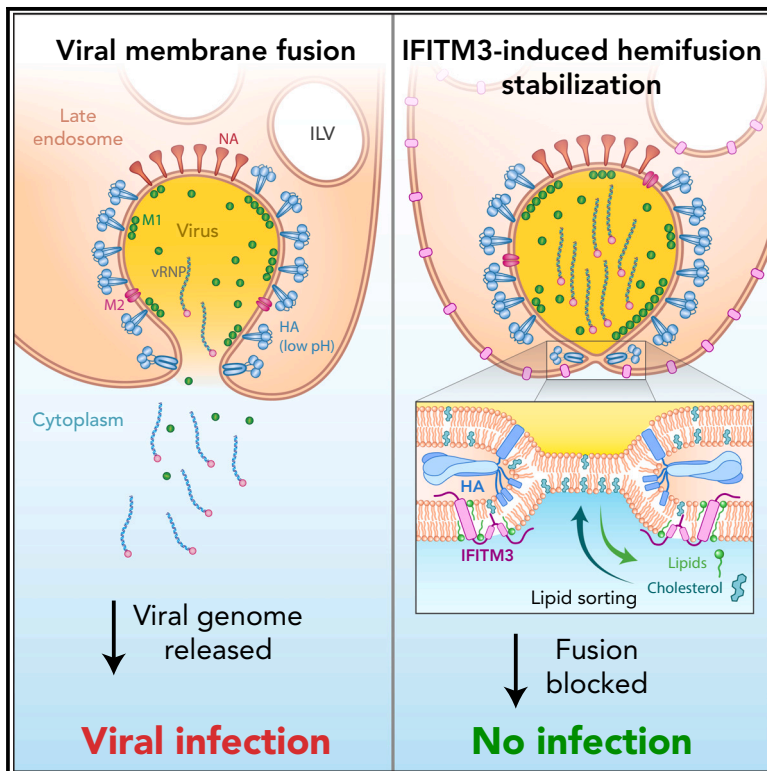


Cell Host & Microbe

IFITM3 blocks influenza virus entry by sorting lipids and stabilizing hemifusion

Graphical abstract



Authors

Steffen Klein, Gonen Golani, Fabio Lolicato, ..., Walter Nickel, Ulrich S. Schwarz, Petr Chlanda

Correspondence

petr.chlanda@
bioquant.uni-heidelberg.de

In brief

Klein et al. examine the broad-spectrum antiviral mechanism of the interferon-induced transmembrane protein 3 (IFITM3) using cryo-electron tomography and computational modeling. They found IFITM3 to modulate the local lipid membrane composition. This blocks influenza A virus endosomal entry by stabilizing the viral membrane fusion in a hemifusion state.

Highlights

- IFITM3 is localized in late endosomes and blocks viral membrane fusion
- IFITM3-induced lipid sorting can increase the energy barrier of viral fusion
- *In situ* cryo-ET confirmed hemifusion stabilization as IFITM3's molecular mechanism
- IFITM3 does not interfere with conformational changes of the viral fusion machinery

Article

IFITM3 blocks influenza virus entry by sorting lipids and stabilizing hemifusion

Steffen Klein,^{1,2,7} Gonen Golani,^{2,3,7} Fabio Lolicato,^{4,5,7} Carmen Lahr,^{1,2} Daniel Beyer,⁴ Alexia Herrmann,⁴ Moritz Wachsmuth-Melm,^{1,2} Nina Reddmann,^{1,2} Romy Brecht,^{1,2} Mehdi Hosseinzadeh,^{1,2} Androniki Kolovou,^{1,2} Jana Makroczyova,^{1,2} Sarah Peterl,^{1,2} Martin Schorb,⁶ Yannick Schwab,⁶ Britta Brügger,⁴ Walter Nickel,⁴ Ulrich S. Schwarz,^{2,3} and Petr Chlanda^{1,2,8,*}

¹Schaller Research Group, Department of Infectious Diseases, Virology, Heidelberg University Hospital, 69120 Heidelberg, Germany

²BioQuant Center for Quantitative Biology, Heidelberg University, 69120 Heidelberg, Germany

³Institute for Theoretical Physics, Heidelberg University, 69120 Heidelberg, Germany

⁴Heidelberg University Biochemistry Center, Heidelberg University, 69120 Heidelberg, Germany

⁵Department of Physics, University of Helsinki, Helsinki, Finland

⁶Electron Microscopy Core Facility, European Molecular Biology Laboratory, 69117 Heidelberg, Germany

⁷These authors contributed equally

⁸Lead contact

*Correspondence: petr.chlanda@bioquant.uni-heidelberg.de

<https://doi.org/10.1016/j.chom.2023.03.005>

SUMMARY

Interferon-induced transmembrane protein 3 (IFITM3) inhibits the entry of numerous viruses through undefined molecular mechanisms. IFITM3 localizes in the endosomal-lysosomal system and specifically affects virus fusion with target cell membranes. We found that IFITM3 induces local lipid sorting, resulting in an increased concentration of lipids disfavoring viral fusion at the hemifusion site. This increases the energy barrier for fusion pore formation and the hemifusion dwell time, promoting viral degradation in lysosomes. *In situ* cryo-electron tomography captured IFITM3-mediated arrest of influenza A virus membrane fusion. Observation of hemifusion diaphragms between viral particles and late endosomal membranes confirmed hemifusion stabilization as a molecular mechanism of IFITM3. The presence of the influenza fusion protein hemagglutinin in post-fusion conformation close to hemifusion sites further indicated that IFITM3 does not interfere with the viral fusion machinery. Collectively, these findings show that IFITM3 induces lipid sorting to stabilize hemifusion and prevent virus entry into target cells.

INTRODUCTION

Perhaps the most decisive step during infection is the release of the viral genome into the cytoplasm for which membrane enveloped viruses rely on their fusion machinery. Many enveloped viruses, such as influenza A virus (IAV), are important human pathogens, and blocking viral entry is one of the most efficient countermeasures the host cell can take. An IAV infection starts with the virus attaching to the host cell by binding the trimeric surface glycoprotein hemagglutinin (HA) to sialic acid residues on the cell surface, followed by clathrin-mediated endocytosis¹ or macropinocytosis.² The acidic environment in late endosomes (LEs) induces complex conformational changes in the HA glycoprotein and triggers the disassembly of the viral matrix 1 (M1) layer. The pre-fusion HA structure undergoes extensive refolding with a loop-to-helix transition of the HA2 domain that leads to the formation of an extended HA intermediate,^{3,4} which anchors the N-terminal fusion peptide into the late endosomal membrane. The extended intermediate folds back into an energetically more stable coiled-coil post-fusion state. The HA re-

folding provides the mechanical work bringing opposing membranes to proximity below 1–2 nm⁵ and forming a hemifusion stalk,^{6–8} which subsequently expands to a hemifusion diaphragm. The diaphragm is a mechanically stressed lipid structure, and transient membrane pores tend to open within it. The magnitude of the energy barrier for pore expansion depends on the lipid composition and determines the stability and dwell time of the hemifusion state. Fusion-pore opening is promoted by lipids with positive, spontaneous curvature (e.g., lysophosphatidylcholine [LPC]) and inhibited by lipids with negative spontaneous curvature (e.g., cholesterol) in the virus and host distal monolayers.⁹ Although HA-mediated membrane fusion has been extensively studied *in vitro* and *in silico*,¹⁰ little is known about how this process is controlled in cells and how host cell restriction factors interfere with this process on the molecular level.

Interferon-induced transmembrane (TM) protein 3 (IFITM3) has evolved as a broad-spectrum cellular restriction factor that blocks cytosolic entry of IAV¹¹ and various late penetrating viruses¹² by interfering with the fusion process. IFITM3 is a small (15 kDa) single-domain TM protein¹³ localized in the

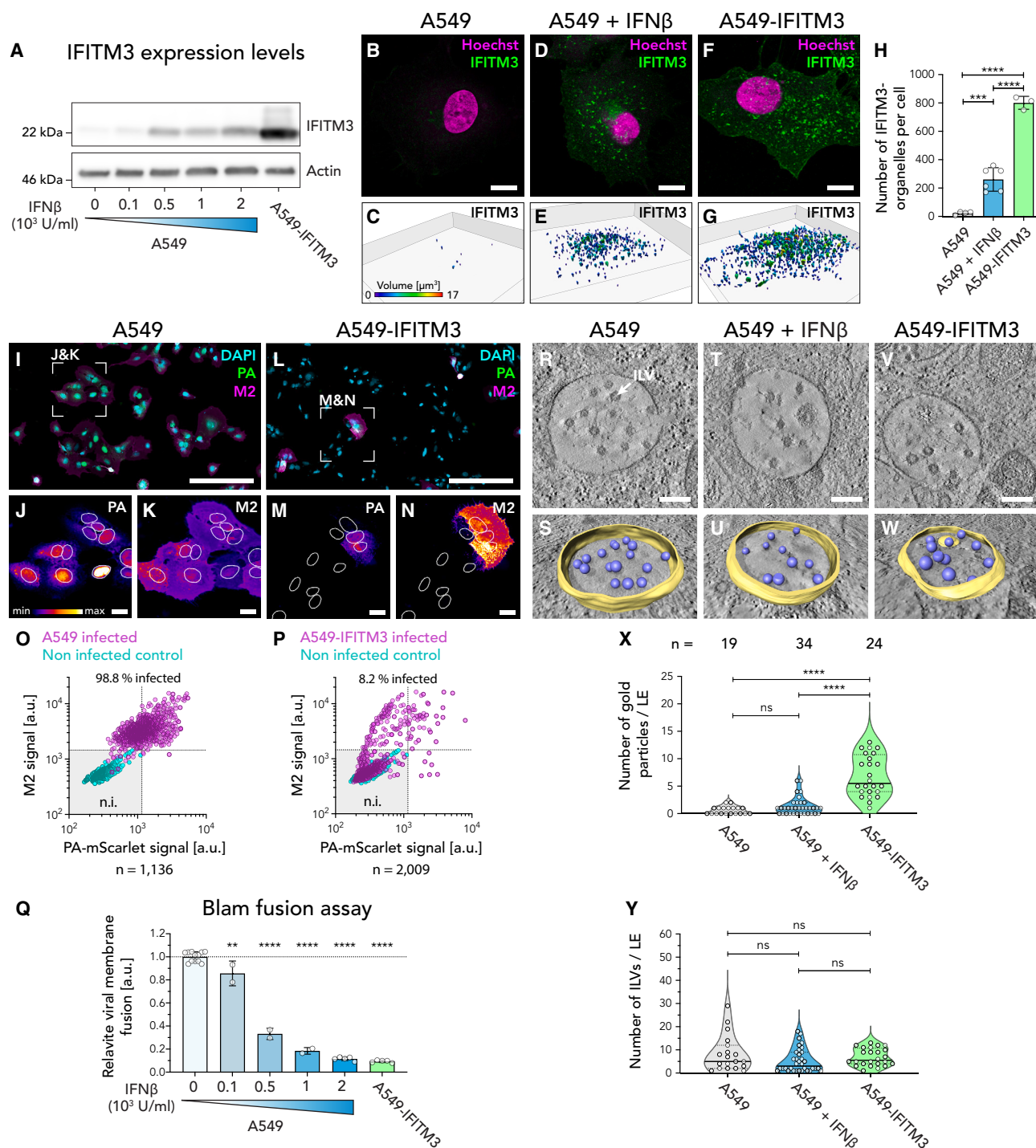


Figure 1. IFITM3 inhibits IAV infection by blocking viral membrane fusion without altering the number of ILVs in the late endosomal lumen (A) Immunoblot analysis of IFN β -1b-treated A549 cells and A549-IFITM3 cells. See Figure S1A for the expression quantification and Figure S1B for the full blot. (B–G) Confocal microscopy analysis of A549 cells (B and C), A549 cells treated with 1 \times 10³ units/mL IFN β -1b (D and E), and A549-IFITM3 cells (F and G). Cells were immunolabeled against IFITM3 (green), and the nucleus was stained with Hoechst 33342 (magenta). The top row (B, D, and F) shows a composite central slice of a representative cell. The bottom row (C, E, and G) shows the three-dimensional segmentation of the IFITM3 signal. Individual objects are color-labeled according to their volume.

(H) The number of individual IFITM3 organelles per cell, as quantified by three-dimensional IFITM3 signal segmentation (C, E, and G). The bar graph shows the mean value with standard deviation (SD). An unpaired t test was performed.

(I–N) IAV infection assay for A549 cells (I–K) and A549-IFITM3 cells (L–N). Cells were infected with the fluorescent reporter virus A/WSN/1933-PA-mScarlet (MOI = 3) (green) and fixed 24 h post-infection (hpi). The viral protein M2 (magenta) was labeled by immunofluorescence, and nuclei were labeled with DAPI (cyan).

(legend continued on next page)

endosomal-lysosomal system.^{14–16} It comprises two amphipathic helices facing the cytosolic side of the endosomal membrane,¹⁷ which are essential for its antiviral properties.¹⁸ IFITM3 is post-translationally modified by S-palmitoylation,¹⁹ essential for the functional incorporation of IFITM3 into the endosomal membrane and its antiviral activity.^{20,21} Fluorescence-microscopy-based live-cell imaging revealed that, although IFITM3 effectively blocks the release of the viral genome into the cytoplasm, lipid mixing between the viral and endosomal membrane could still be observed.²² Based on these data, two alternative models were proposed. In the so-called “hemifusion stabilization” model, IFITM3 interferes with the fusion pore formation in a direct or indirect mode of action, whereas, in the “fusion decoy” model, IFITM3 increases the number of endosomal intraluminal vesicles (ILVs), which may serve as a decoy target for virus membrane fusion.²² *In vitro* experiments suggest that IFITM3 may function by altering the biophysical properties of the membrane²³ or by changing the lipid composition and cholesterol levels of the endosomal membranes.^{24–26} However, despite many studies on IFITM3, the exact mode of action remains to be clarified. It has not yet been addressed on the molecular level and directly inside the infected host cells.

RESULTS

IFITM3 does not alter the number of ILVs in the late endosomal lumen

Although IFITM3 expression can be induced by type I interferon (Figures 1A and S1A–S1C), interferon treatment leads to the induction of additional restriction factors that may inhibit viral entry. Hence, we established an A549 cell line stably overexpressing non-tagged IFITM3 (A549-IFITM3), which showed a significant 3.9-fold increase in IFITM3 expression level compared with A549 cells induced with IFN β -1b (Figures 1A, S1A, and S1B). The stable overexpression of IFITM3 did not induce the expression of IFITM1 or IFITM2 (Figure S1C). Fluorescent confocal microscopy showed that IFITM3 partially colocalizes with the late endosomal marker Rab7 (Pearson's $r = 0.51$, SD = 0.08, $n = 9$) and the lysosomal marker LAMP1 (Pearson's $r = 0.64$, SD = 0.14, $n = 10$) (Figure S2), consistent with previous studies on endogenous IFITM3,^{14–16,27} showing that the cellular localization of IFITM3 in the A549-IFITM3 cell line is unaltered. As

expected, both IFN β -1b treatment and stable IFITM3 expression increased the number of IFITM3-positive cellular organelles in A549 cells (Figures 1B–1H). Three-dimensional segmentation (Figures 1C, 1E, and 1G) revealed a 3.1-fold increase in the number of organelles (Figure 1H) and a moderate but significant 1.3-fold increase in average organelle volume of $0.39 \mu\text{m}^3$ (SD = $0.41 \mu\text{m}^3$, $n = 2,402$) (Figure S1D) when compared with the IFN β -1b treated A549 cell line. To characterize the antiviral effect of the A549-IFITM3 cell line, cells were infected and immunolabeled against M2 (Figures 1I–1P). While A549 cells showed an infection rate of 98.8% ($n = 1,136$) (Figure 1O), the infection rate in A549-IFITM3 was dramatically decreased (11.5-fold) because only 8.2% ($n = 2,009$) of the cells were infected (Figure 1P). These data agree with the previously reported antiviral properties of IFITM3.¹¹ To further validate the antiviral properties of the A549-IFITM3 cell line, we performed a β -lactamase (Blam) cell entry assay utilizing influenza A virus-like particles (VLPs) expressing M1-Blam.²⁸ Our data show an IFN β -1b concentration-dependent decrease in relative viral entry with an up to 8.7-fold decrease. In comparison, A549-IFITM3 showed a relative viral entry inhibition of 10.7-fold (Figures 1Q and S1I). Overall, these data are consistent with previous studies^{14,22} and show that viral-induced membrane fusion in LEs is inhibited in A549-IFITM3 cells.

To test the “fusion decoy” hypothesis,²² we determined morphological changes of LEs in A549-IFITM3 cells by electron tomography (Figures 1R–1Y). Because the “fusion decoy” hypothesis suggested an increase in ILVs, we analyzed LEs in a total of 77 tomograms of A549 cells ($n = 19$), A549 cells treated with 2×10^3 units/mL IFN β -1b ($n = 34$), and A549-IFITM3 cells ($n = 24$). The endosomal membrane and ILVs were 3D segmented (Figures 1S, 1U, and 1W) to quantify the endosomal volume (Figure S1J). Consistent with confocal microscopy data (Figure S1D), late endosomal volume in A549-IFITM3 cells was modestly (1.6-fold) but significantly increased compared with non-treated A549 cells (Figure S1J). Immuno-gold-labeling against IFITM3 showed that LEs in A549-IFITM3 cells displayed a significantly higher (5.3-fold) IFITM3 labeling than A549 cells (Figures 1X and S3). These data are consistent with the increased IFITM3 expression levels of A549-IFITM3 cells (Figure 1A) and show that IFITM3 is specifically localized to multivesicular organelles. Importantly, our data revealed no significant difference in the number of

Composite overview images for both conditions are shown (I and L). For each condition, a magnified area (white squares) for the signals of PA-mScarlet and M2 are shown in the bottom row (J, K, M, and N) using a fire lookup table. Individual nuclei were segmented (indicated with white outlines), allowing for measuring the average signal intensity for PA-mScarlet and M2 in the segmented area.

(O and P) Quantification of infection rate for A549 cells (O) and A549-IFITM3 cells (P). For each segmented nucleus, the signal intensity for PA-mScarlet and M2 is shown as a scatter plot for infected cells (magenta) and non-infected control (cyan). Two thresholds of $M1 \leq 1,150$ a.u. and $PA\text{-mScarlet} \leq 1,450$ a.u. (dotted lines) were defined for non-infected (n.i.) cells (shown as a gray square), and accordingly, all other cells are defined as infected. See Figures S1E–S1H for immunofluorescence images and scatter plots of the non-infected control only.

(Q) Blam-based cell entry assay for IFN β -1b-treated A549 and A549-IFITM3 cells infected with M1-Blam influenza A VLPs. An unpaired t test was performed. See Figure S1I for fluorescence microscopy images of all samples.

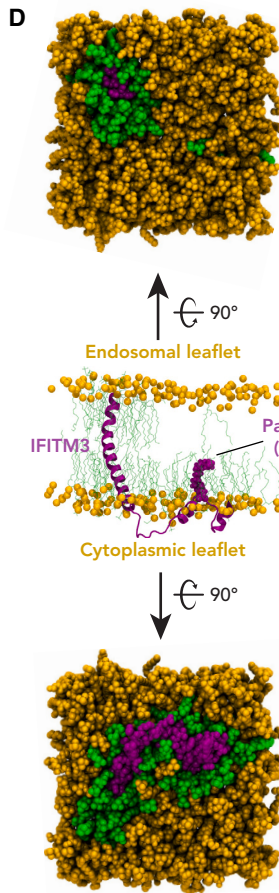
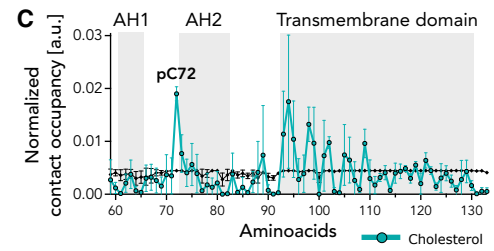
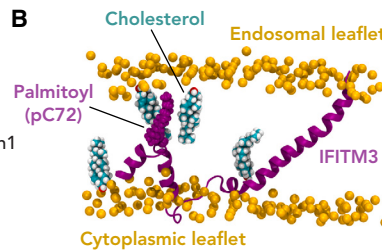
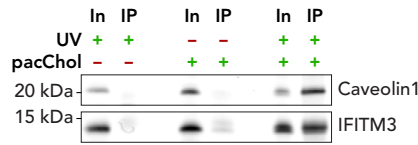
(R, T, and V) Tomographic slices of A549 cells, IFN β -1b-treated A549 cells (T), and A549-IFITM3 cells (V). A representative late endosome was selected for each sample with the typical multivesicular morphology. One ILV is indicated (white arrow in R). 10 slices were averaged (10.9 nm), and low pass filtered (3.09 nm). See Figure S3 for a gallery of late endosomes for each condition.

(S, U, and W) Three-dimensional segmentation of the late endosomes is shown in (R), (T), and (V). The late endosomal membrane (yellow) and individual ILVs (purple) were segmented.

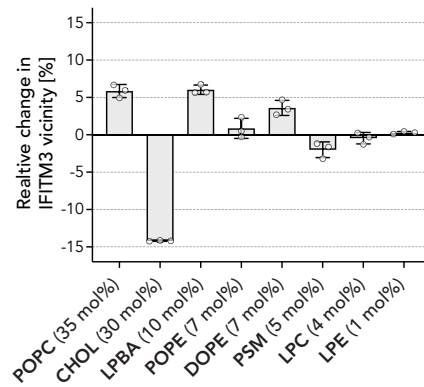
(X) Quantification of anti-IFITM3 immunogold particles per late endosome. See Figure S3 for a gallery of immune-gold-labeled late endosomes.

(Y) Quantification of the number of ILVs per endosome. Statistical significance: * $p < 0.05$, ** $p < 0.01$, *** $p < 0.001$, **** $p < 0.0001$. Scale bars: 10 μm in (B)–(F), 200 μm in (I) and (L), 20 μm in (J), (K), (M), and (N), and 200 nm in (R), (T), and (V).

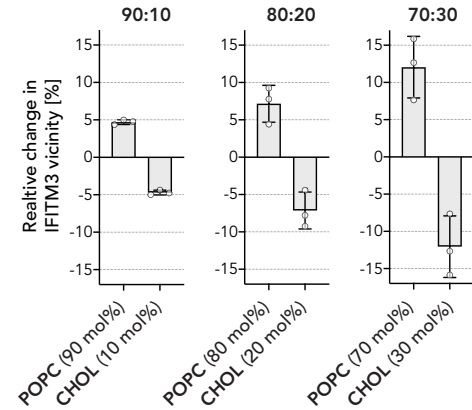
A Cholesterol interaction



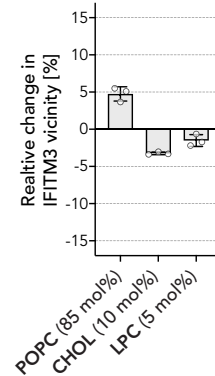
E Endosomal-like membrane



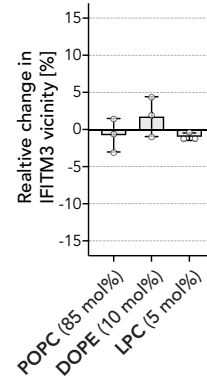
F POPC-CHOL



G POPC-CHOL-LPC



H POPC-DOPE-LPC



I Cholesterol repulsion

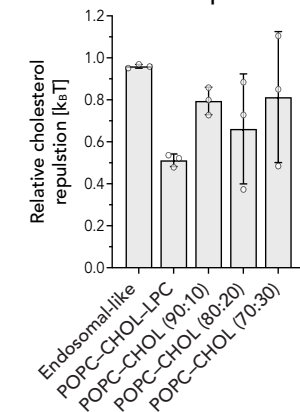


Figure 2. Molecular dynamics simulations predict IFITM3-induced lipid sorting by selective lipid binding

(A) Analysis of IFITM3-cholesterol interactions in A549-IFITM3 cells. Cells were treated with pacChol, UV cross-linked, and immunoblot was performed against IFITM3 after immunoprecipitation (IP). Caveolin1 was used as a positive control. Full blots can be found in [Figures S4A](#) and [S4B](#).

(B) A representative snapshot of the interaction between cholesterol molecules and IFITM3 in a binary POPC-cholesterol (90:10) system. IFITM3 is represented as a ribbon (magenta), and the palmitoyl group of Cys72 is represented as an atom sphere model, having a van der Waals (vdW) radius of their respective atoms. Phosphorus atoms of the POPC head groups are represented as an atom sphere model (orange). POPC tails are not shown. Cholesterol molecules in contact (distance < 0.4 nm) with IFITM3 are represented as an atom sphere model (cyan), with oxygen atoms in red and hydrogen atoms in white. Non-interacting cholesterol molecules are not shown.

(C) Normalized contact occupancy between IFITM3 and POPC (black graph) or cholesterol (cyan graph) in a binary POPC-cholesterol (90:10) model membrane as shown in (B). A contact is defined if the distance between any atoms of IFITM3 and POPC (or cholesterol) is less than 0.4 nm. Data are normalized based on the total number of lipids of each lipid type. The sequence sections for the two amphipathic helix domains (AH1 and AH2) and the transmembrane domain are indicated. Error bars are shown as standard deviation (SD).

(D) A representative snapshot of IFITM3 (magenta), with palmitoylated Cys72, embedded in a late endosomal-like model membrane (orange). The central side view shows IFITM3 as a ribbon model, with the palmitoyl group at Cys72 as an atom sphere model. Lipid tails of lipids in close vicinity to IFITM3 (<0.4 nm) are shown as stick model (green), and all other lipid tails are hidden. The top views of both the endosomal (top) and cytoplasmic (bottom) leaflets are shown. All molecules are shown as an atom sphere model, with IFITM3 in magenta, lipids in close vicinity to IFITM3 (<0.4 nm) in green, and all other lipids in orange.

(legend continued on next page)

ILVs per endosome between A549 cells, IFN β -1b-treated A549 cells, or A549-IFITM3 cells (Figure 1Y), hence contradicting the assumptions of the “fusion decoy” model.

IFITM3 modulates the local lipid composition of the endosomal membrane

We next analyzed the impact of IFITM3 on the lipid composition of these organelles. It has been previously reported that IFITM3 alters the cholesterol level in endosomes.²⁴ To determine whether IFITM3 directly interacts with cholesterol, we performed UV cross-linking using a photo-reactive and clickable cholesterol analog (pacChol) as a probe to map cholesterol-IFITM3 interactions in living cells. Western blot analysis of immunoprecipitated pacChol showed that IFITM3 and cholesterol directly interact (Figure 2A), as reported recently.²⁶

To further characterize the IFITM3-cholesterol interaction, we employed atomistic molecular dynamics (MD) simulations of IFITM3 embedded in different lipid compositions. Because palmitoylated Cys72 is essential for IFITM3's antiviral properties,²¹ this modification was incorporated in all MD simulations. First, we analyzed the contact occupancy for each amino acid of IFITM3 in a binary 1-palmitoyl-2-oleoyl-sn-glycero-3-phosphocholine (POPC)-cholesterol (90:10) model membrane (Figure 2B). Our data revealed that, although most IFITM3 amino acids showed a low probability of interactions with cholesterol, there is an increased interaction probability in the cytosolic region of the TM domain, and the palmitoylated Cys72 displayed the strongest cholesterol-interaction probability of 1.9×10^{-2} (SD = 1.3×10^{-3} , $n = 3$) (Figure 2C). Next, we investigated the IFITM3-cholesterol interactions in a complex membrane environment by simulating IFITM3 in a late endosomal-like membrane^{29,30} composed of eight different lipids (performed 3 times for a cumulative time of 18 μ s). The IFITM3-lipid interaction landscape was investigated by comparing the molar fraction of lipids surrounding IFITM3 with the lipid bulk concentrations at a radial distance of 0.4 nm around IFITM3 (Figure 2D, green lipids). Our data highlight a statistically significant ($p < 0.000001$, Figure S4C) depletion of cholesterol from IFITM3's vicinity by 14.2% (SD = 0.1%, $n = 3$) (Figure 2E). The repelled cholesterol is mainly replaced by the two lipids POPC and lysobisphosphatidic acid (LBPA) (Figure 2E), which showed a statistically significant (Figure S4C) enrichment in IFITM3's vicinity of 5.9% and 6.0%, respectively. To understand if the cholesterol levels in the membrane influence this IFITM3-induced lipid-sorting, we analyzed binary POPC-cholesterol lipid systems at cholesterol concentrations of 10, 20, and 30 mol %. We found that the IFITM3-induced cholesterol depletion activity can be observed in all tested cholesterol concentrations in a linear concentration-dependent manner (Figure 2F). To further analyze whether the IFITM3-induced cholesterol depletion is because of cholesterol's intrinsic negative curvature, we simulated a POPC-cholesterol-LPC (80:10:5) system in which cholesterol depletion, but no LPC accumulation, was observed (Figure 2G). Next, we replaced

cholesterol in this system with 1,2-dioleoyl-sn-glycero-3-phosphoethanolamine (DOPE), a lipid with an intrinsic negative curvature comparable to cholesterol. Surprisingly, DOPE is not depleted in the IFITM3 vicinity (Figure 2H), suggesting that the IFITM3-mediated cholesterol depletion activity is not dependent on the intrinsic curvature of the lipid but rather cholesterol specific. Finally, we calculated the relative repulsion energy of cholesterol from IFITM3 compared with all of the other lipids in the system based on the de-mixing entropy of cholesterol depletion near IFITM3 (Figure 2D, green lipids) and its accumulation in bulk (Figure 2D, orange lipids). We found the repulsion strength in the endosomal-like lipid composition to be 0.96 $k_B T$ (SD = 0.01 $k_B T$, $n = 3$). Repulsions calculated from membrane models with different lipid compositions were similar (Figure 2I), indicating that the repulsion is independent of the cholesterol concentration.

The observed selective cholesterol binding to the TM domain and the palmitoylated Cys72 might be important for the specific localization of IFITM3 to cholesterol-rich late endosomal membranes. However, the local cholesterol repulsion ability of IFITM3 leads to local lipid sorting in the late endosomal membrane.

IFITM3-induced lipid sorting increases the energy barrier for fusion pore formation

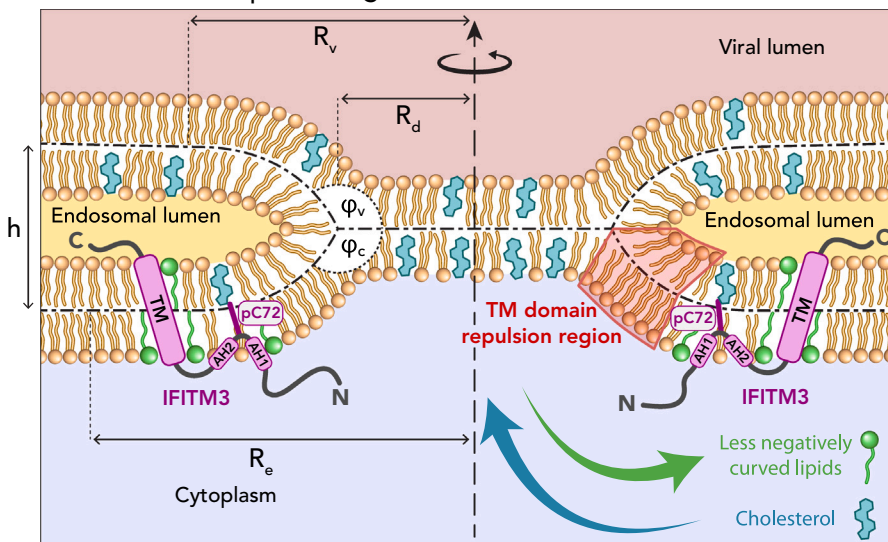
Previous experimental studies revealed that IFITM3 does not affect the initiation of fusion and lipid mixing, but it blocks membrane fusion pore formation.^{22,23,31} We suggest that the observed cholesterol repulsion from the IFITM3 vicinity (Figures 2E–2I) and its accumulation in the virus and hemifusion diaphragm membranes are the primary force behind the fusion inhibition. The hemifusion diaphragm rim is a three-way junction between the endosomal and viral membranes (Figure 3A), characterized by a strong lipid tilt and splay, which decays at a 3–4 nm distance from the rim.^{32–34} As a result, the TM domain of IFITM3 is repelled from it and cannot pass the rim to the diaphragm and virus membranes (Figure 3A, TM domain repulsion region). Because the amphipathic helices and the Cys72 domains of IFITM3 span about 2.5 nm from the TM domain (Figure 3A), it is unlikely that any part of the IFITM3 protein can reach the diaphragm. In such a setting, the hemifusion diaphragm rim and its surroundings act as a semipermeable barrier between the compartments, allowing only lipids to pass but not IFITM3. As a result of IFITM3-induced cholesterol repulsion, cholesterol is likely to be enriched in IFITM3-free regions of the hemifusion diaphragm and virus membranes and be replaced by more positively curved lipids (Figure 3B), causing local lipid-sorting. Thus, the mean intrinsic curvature of the hemifusion diaphragm monolayers shifts to more negative values leading to a decrease in mechanical stress in the diaphragm^{32,34,35} and an increase in the membrane pore line tension,^{36–38} which, in turn, increases the energy barrier of fusion pore expansion and inhibits fusion.

To test this hypothesis, we used continuum modeling of the fusion site,^{32–34} based on the theory of lipid membrane elasticity

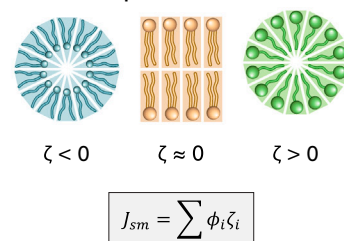
(E–H) Relative changes of lipid concentrations in the vicinity of IFITM3 (<0.4 nm) for different lipid systems: late-endosomal-like lipid system (E); binary POPC-cholesterol lipid system with cholesterol concentrations of 10, 20, and 30 mol % IFITM3 (F); ternary POPC-cholesterol-LPC lipid system (G); and ternary POPC-DOPE-LPC lipid system (H).

(I) Cholesterol repulsion from IFITM3 for all studied membrane systems. All plots in (E)–(I) show the mean of three independent MD simulation runs. Individual values are indicated. The error bar represents the standard deviation (SD).

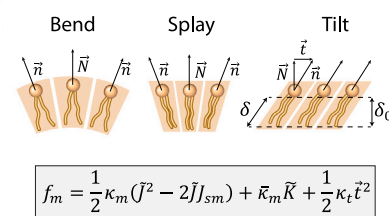
A IFITM3-induced lipid sorting



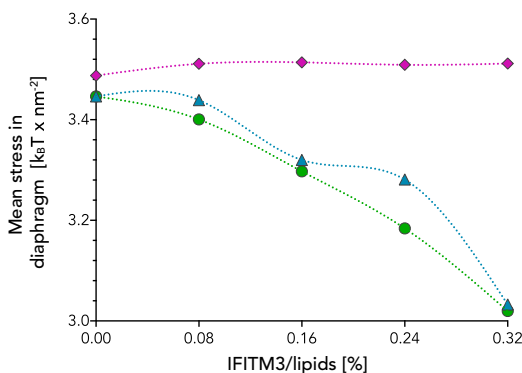
B Intrinsic lipid curvature ζ



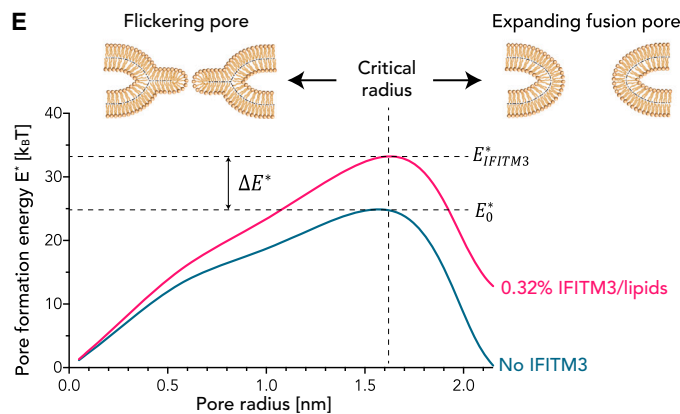
C Lipid splay and tilt



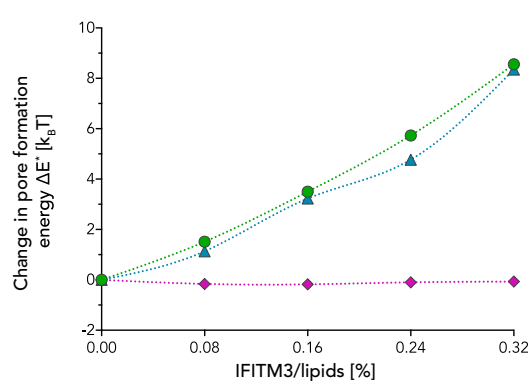
D



E



F



G

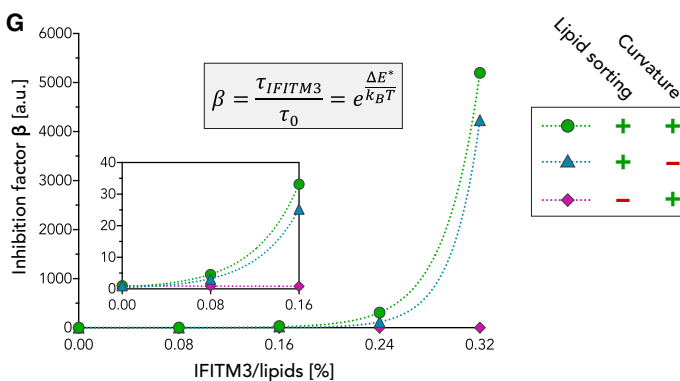


Figure 3. Continuum membrane modeling predicts that IFITM3-induced lipid sorting increases the energy barrier for fusion pore formation and thus stabilizes the hemifusion state

(A) Schematic representation of a hemifusion diaphragm during viral membrane fusion at the late endosome. The viral lumen (red), endosomal lumen (yellow), and cytoplasmic lumen (blue) are indicated. The geometry of the fusion site is defined by: the hemifusion diaphragm radius, R_d ; the distance between the mid-planes of fusing membranes, h ; and the inner angles in the cytosol and virus lumen side, φ_c and φ_v , respectively. The radii of the fusion site, R_v and R_e , are defined as the distance from the center to where tilt and splay deformation vanish. The geometry of the fusion site is not fixed and is subjected to energy minimization. The main structural features of IFITM3 are shown in purple: the transmembrane domain (TM), the two amphipathic helices (AH1 and AH2), and the palmitoylated cysteine 72 (pC72), which interacts with a cholesterol molecule. The “TM domain repulsion region” (dark red) represents the area near the diaphragm rim with a very strong tilt and splay. The TM domain of the IFITM3 is repelled from this region. IFITM3-induced lipid sorting is indicated with the blue and green arrows.

(B) Schematic models of different intrinsic lipid curvatures, ζ . The monolayer spontaneous curvature, J_{sm} , is the averaged sum of all the lipid components with ϕ_i STAR Methods; Equation 5).

(legend continued on next page)

(Figure 3C),^{39,40} and calculated the mechanical stress and energy barrier of membrane fusion pore expansion. We used the relative repulsion between cholesterol and IFITM3 as the “Endosomal-like membrane” composition of $0.96 k_B T$ derived from the MD simulations (Figure 2I) and determined the lipid sorting between the endosome and diaphragm membrane as a function of the IFITM3 mole fraction. We found that cholesterol is enriched in hemifusion diaphragms at $8.3\% / (\text{mol}_{\text{IFITM3}} \%)$ beyond the baseline value of 30% , leading to the reduction of the monolayer spontaneous curvature by $0.031 \text{ nm}^{-1} / (\text{mol}_{\text{IFITM3}} \%)$ (Figure S5A), and an increase of membrane-pore rim line tension by $6 \text{ pN} / (\text{mol}_{\text{IFITM3}} \%)$ (Figure S5A). Next, we simulated the fusion site shape (Figure S5B) and the lipid tilt and splay-related stresses in the diaphragm as a function of the IFITM3 mole fraction (Figure S5C). We found that the mean mechanical stress in the diaphragm decreases by $1.28 k_B T / (\text{nm}^2 \cdot \text{mol}_{\text{IFITM3}} \%)$ (Figure 3D). The energy barrier for pore expansion increases by $26 k_B T / (\text{mol}_{\text{IFITM3}} \%)$ (Figure 3F, sensitivity to cholesterol-IFITM3 relative repulsion presented in Figure S5D and to the cholesterol concentration in Figure S5E). Hence, IFITM3 can inhibit fusion pore expansion because of the IFITM3-cholesterol sorting effect. Considering that cholesterol can undergo spontaneous flip-flop in the absence of a dedicated flippase,⁴¹ we assume that the cholesterol distribution in the hemifusion diaphragm is symmetric.

A recent study reported that the amphipathic helix domain of IFITM3 induces a strong negative membrane curvature,²³ which may influence the outcome of membrane fusion in addition to the effect of lipid sorting. Thus, we next calculated the changes in the mean mechanical stress and energy barrier of fusion-pore expansion when IFITM3-induced negative membrane curvature alone or combined with IFITM3-induced lipid sorting. Overall, IFITM3-induced negative curvature slightly increased the energy barrier of fusion-pore expansion in the presence of lipid sorting (from 26 to $27 k_B T / (\text{mol}_{\text{IFITM3}} \%)$ (Figure 3F). However, in the absence of lipid sorting, IFITM3 had a negligible effect on the energy barrier for pore expansion (Figure 3F). We also tested the possibility that the amphipathic helix domain of IFITM3 penetrates the diaphragm. In such a scenario, IFITM3 cannot induce lipid sorting between the diaphragm and endosomal membrane as it is, on average, equally distributed between the two. We found that the fusion-pore expansion energy barrier increases only by $0.45 k_B T / (\text{mol}_{\text{IFITM3}} \%)$ because of the negative intrinsic curvature of the IFITM3 amphipathic helix. Hence, our findings show that IFITM3-induced lipid sorting is the main effector of fusion pore expansion inhibition. This important lipid sorting activity of

IFITM3 might be partially caused by the ability of IFITM3 to induce negative membrane curvature.²³

As IFITM3 increases the energy barrier of fusion pore expansion, the time required to complete viral membrane fusion in LEs, hereafter termed “dwell time,” increases. We quantified this increase by calculating the ratio between the dwell time in the presence of IFITM3, τ_{IFITM3} , to the dwell time without IFITM3, τ_0 (Figure 3G). Our data showed that even a modest concentration of 0.16% IFITM3 (one IFITM3 molecule per 625 lipids) increases the dwell time by a factor of 33 if we consider both the sorting and direct mechanical effect of IFITM3. In summary, continuum membrane modeling results predict that IFITM3-induced lipid sorting leads to an increased energy barrier for fusion pore formation and thus to a prolonged dwell time in hemifusion.

IFITM3 stabilizes the hemifusion state in LEs

To validate our theoretical model, we utilized *in situ* cryo-electron tomography (cryo-ET), which allows direct visualization of membrane-protein interactions inside cells under native conditions. A549-IFITM3 cells were infected with a fluorescently labeled virus and were plunge-frozen 1 h post-infection (hpi). Using *in situ* cryo-correlative light and electron microscopy (cryo-CLEM),⁴² infected cells were selected for cryo-focused ion beam (cryo-FIB) milling to prepare cryo-lamellae.^{43,44} Cryo-EM of lamellae showed putative endosome-like organelles that were used as sites for tomography acquisition, and subsequent correlation allowed us to validate the presence of labeled virions in these endosomal compartments (Figures 4A–4D and S6). Cryo-ET revealed the ultrastructure of LEs (Figures 4E and 4F; Video S1) with a similar multivesicular structure as observed by ET (Figure 1V), showing protein-coated ILVs (Figure S7). In addition to ILVs, we observed a total of 43 individual viral particles in LEs and lysosomes of four different cells (Figures 4E and S8–S10; Videos S1, S2, S3, and S4), indicating that these viruses are unable to enter the cytoplasm, because IAV membrane fusion should occur within 10–15 min after uptake in the absence of IFITM3.^{1,45,46}

Viral particles showed a characteristic diameter of 87.8 nm ($SD = 7.8 \text{ nm}$, $n = 18$). Intriguingly, IAV particles were regularly bound to small crystal-like structures (Figures 4I and 4J, arrowheads), structurally similar to low-density lipoprotein particles containing a cholesterol ester core⁴⁷ and to structures found in LEs and lysosomes.⁴⁸ All viral particles featured a disorganized HA phenotype comparable to *in vitro* cryo-ET studies of IAV particles at pH 4.9.⁴⁹ The M1 matrix layer was partially disassembled in 83% of the observed viral particles and fully disassembled in 9% , indicating that the observed viral particles in LEs were exposed to a low pH environment. The remaining 8%

(C) Theory of lipid splay-tilt and lipid monolayer energy density, f_m (STAR Methods; Equation 4). Schematic representations of lipid bend, splay, and tilt are shown, with the lipid director, \vec{n} ; the normal to the mid-plane director, \vec{N} ; the lipid tilt director, \vec{t} ; the length of lipid tails, δ ; and relaxed lipid tail length, δ_0 . Monolayer bending rigidity, κ_m ; lipid splay, \bar{J} ; monolayer spontaneous curvature, J_{sm} ; monolayer saddle-splay modulus, $\bar{\kappa}_m$; lipid saddle-splay, \bar{K} ; tilt modulus, κ_t . (D–G) Results of the continuous membrane modeling. The following parameters were used in all simulations: $\kappa_m = 14.4 k_B T$, $\bar{\kappa}_m = -7.2 k_B T$, $\kappa_t = 40 \text{ mN/m}$, $\delta_0 = 1.5 \text{ nm}$, $\zeta_{chol} = -0.5 \text{ nm}^{-1}$, $\zeta_0 = -0.1 \text{ nm}^{-1}$, $\phi_{chol} = 0.3$ and $\lambda_0 = 15 \text{ pN}$. The lipid distribution scenarios used in (D), (F), and (G) are indicated in the legend. (D) Mean stress because of splay and tilt deformations in the diaphragm as a function of IFITM3 concentration. (E) Pore formation energy, E^* , as a function of the pore radius in a model without IFITM3 (blue-green graph) and with a 0.32% IFITM3/lipid ratio (magenta graph). The “with sorting; with curvature” scenario was used here. The critical radius represents the transition from flickering-pore to expanding fusion-pore. (F) Change in fusion-pore formation energy, $\Delta E^* = E^*(\phi_{\text{IFITM3}}) - E_0^*$, as a function of IFITM3 concentration, with E_0^* being the energy barrier without IFITM3 and $E^*(\phi_{\text{IFITM3}})$ being the energy barrier with the IFITM3 mole fraction, ϕ_{IFITM3} . (G) Inhibition factor, β , of IFITM3 (STAR Methods; Equation 18), which describes the ratio between the time of pore opening with IFITM3, τ_{IFITM3} , and without IFITM3, τ_0 , as a function of IFITM3 concentration.

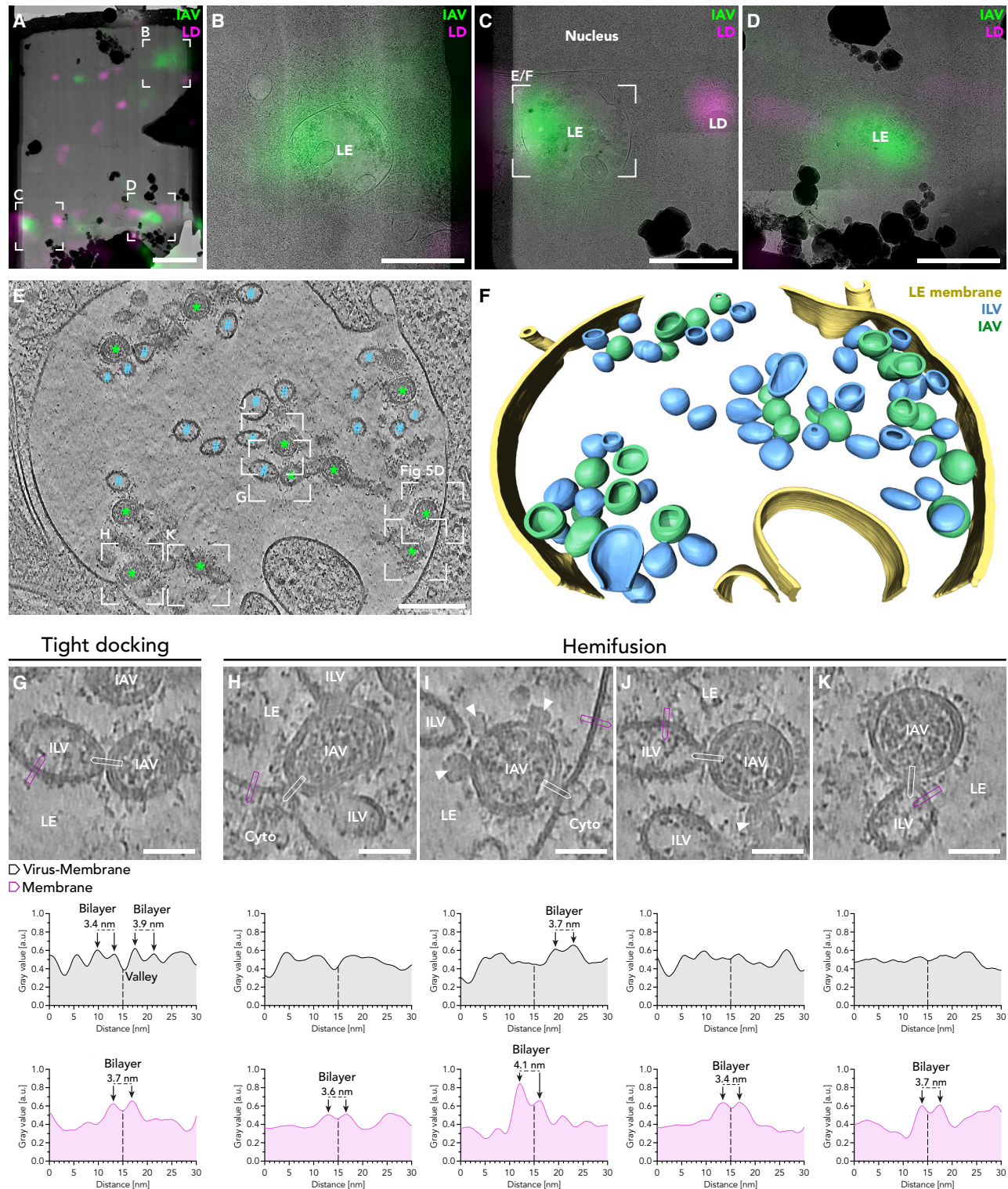


Figure 4. IFITM3 stabilizes hemifusion intermediates during IAV mediated fusion with the late endosomal limiting membrane and ILVs
 (A) Cryo-lamella of an A549-IFITM3 cell infected with fluorescently labeled influenza virus A/WSN/1933-nDiO (MOI = 200, 1 hpi). The fluorescent signal of IAV is shown in green. The LD signal is shown in magenta.
 (B-D) Magnified areas of the correlated cryo-lamella shown in (A). Late endosomes (LEs) with a typical multivesicular morphology were found positive for fluorescent IAV signal. One correlated LD is shown in (C).

(legend continued on next page)

of viral particles showed no sign of disassembly. Importantly, IAVs were frequently observed in close contact with ILVs and the endosomal limiting membrane. These contact sites displayed deformations of the limiting endosomal membrane toward the viral membrane forming a membrane merger, a structure consistent with hemifusion intermediates between viral and endosomal membranes. We observed 21 contact sites between IAV particles and ILVs and 6 contact sites between IAV particles and the limiting late endosomal membrane (Figures S8–S12; Table S2). We classified 15% of all contact sites as tight docking and 85% as hemifusion ($n = 27$) by linear density profiles (Figures 4G–4K and S8–S12). The linear density profiles of the tight docking events showed signal peaks of two juxtaposed phospholipid bilayers separated by a distinct drop in signal, indicating that the two membranes are not in hemifusion. In contrast, linear density profiles of all events classified as hemifusion lacked juxtaposed phospholipid bilayers. The absence of a low-density valley between the viral and endosomal membrane argues for possible lipid exchange between the viral and endosomal membrane, which is in accord with live-cell fluorescence microscopy studies.²² Importantly, these structures resembled liposome membrane deformations, including so-called pinching and hemifusion states formed *in vitro* between influenza virions and liposomes.^{36,50–52} However, extended tight docking reported between liposomes and IAV was not observed. It is plausible that some differences between *in situ* and *in vitro* membrane fusion intermediates arise from the proteins present inside the endosomal membranes. Interestingly, viral membrane curvature at the hemifusion sites appeared largely intact, likely reflecting the rigidity and pressure difference between the virus and cell membrane. The M1 layer was still partially or fully intact in most cases (91%), and it might still provide additional rigidity to the virus envelope that favors the initial bent shape of the virus, as commonly seen in virus-liposome fusion *in vitro*.^{50,51,53} No fused IAV or viral ribonucleoproteins (vRNPs) were observed in the cytosol, illustrating that IFITM3 can effectively block the membrane fusion of most incoming viruses. Most contact sites (78%, $n = 21$) were observed between viral particles and ILVs (Figures 4G, 4J, 4K and S11; Table S2). In contrast, only a smaller fraction (22%, $n = 6$) was found in contact with the limiting late endosomal membrane (Figures 4H, 4I, and S12; Table S2), suggesting that ILVs can frequently serve as a fusion target for IAV. These data show that IFITM3 not only blocks viral entry via fusion with the limiting late endosomal membrane but can also block indirect entry pathways through fusion with ILVs and subsequent back-fusion of ILVs with the limiting late endosomal membrane. Thus, IFITM3 can likely impede the endosomal escape of

different viruses, which are known to hijack the back-fusion pathway⁵⁴ by blocking membrane fusion with ILVs. This is in accord with a recent study showing that IFITM3 prevents ILV back-fusion.⁵⁵

Stabilized hemifusion diaphragms show symmetric geometry and a high energy barrier for fusion pore formation

The hemifusion sites visualized by *in situ* cryo-ET showed an axial symmetry around the central axis, and their geometry could be quantified from our tomograms. Measurements of the hemifusion sites ($n = 17$) (Figures 5A–5C) revealed a narrow average outer angle of 63° ($SD = 12^\circ$) and wide inner viral and cytoplasmic angles of 157° ($SD = 11^\circ$) and 140° ($SD = 13^\circ$), respectively. As no significant differences were observed between opposing contact angles, the hemifusion sites were either formed by symmetric expansions or converged into a favorable symmetric geometry.⁵⁷ The average hemifusion diaphragm diameter measured from the phospholipid head groups was 16.5 nm ($SD = 5.3$ nm, $n = 17$), consistent with stable hemifusion diaphragms observed *in vitro*.⁵⁰ The observed hemifusion site geometry allowed us to assess, based on the geometry of the hemifusion diaphragm, the stress in the hemifusion diaphragm and the fusion-pore formation energy as 113 $k_B T$ ($SD = 44$ $k_B T$, $n = 16$). This energy barrier is higher than the energy barrier estimated by our simulations (25 $k_B T$ with no IFITM3 and 33 $k_B T$ with 0.32% IFITM3, Figure 3E). However, the energy barrier generated by our simulations strongly depends on the lipid composition in the LE and the monolayer tilt and bending rigidities; therefore, an exact comparison between theory and experiment is challenging. For example, the theory predicts an energy barrier of more than 100 $k_B T$ by considering higher cholesterol concentrations (40% instead of 30%, Figure S5E) or a more rigid membrane, as expected for higher cholesterol concentrations (Figure S5F). Therefore, based on the cryo-ET results, it is likely that the cholesterol fraction in the LE in our model is underestimated.

Post-fusion HA is confined in stabilized hemifusion diaphragms

Intriguingly, regular cylindrical densities orthogonal to the hemifusion diaphragms were frequently observed (Figures 5D and 5E, magenta arrow) at both ILV membranes (Figure S11, red arrows) and late endosomal membranes (Figure S12, red arrows). Sub-volume extraction and iterative averaging of potential HA glycoproteins localized at hemifusion diaphragms ($n = 30$) revealed a rod-shaped structure featuring a stalk and head (Figures 5F,

(E) Tomographic slice (5.34 nm thickness) of a late endosome correlated to the IAV fluorescence signal (C). The late endosomal lumen incorporates ILVs (blue hashes) and IAV particles (green asterisks). Reconstructed tomograms were simultaneous iterative reconstruction technique (SIRT)-like filtered and denoised using cryoCARE. See Video S1 for three-dimensional rendering.

(F) The three-dimensional volume segmentation of the tomogram shown in (E). The late endosomal membrane is shown in yellow, IAV particles in green, and ILVs in blue.

(G–K) Magnified areas of reconstructed tomogram in (E), showing interaction sites between IAV particles and cellular membranes. For each example, a line profile with a thickness of 5.34 nm of the virus-membrane interaction (middle row, black) and a membrane (bottom row, magenta) are shown with positions indicated in the tomograms (white square for virus membrane interaction; magenta square for membrane). (G) Line profile of a tight docking event.

(H–K) Line profiles of hemifusion sites between viral and endosomal membranes. For all shown examples, a line profile of the phospholipid bilayer of an endosomal membrane is shown (magenta plots), with each monolayer discernible. The width of each bilayer was determined by measuring the distance between the two maxima and reported in the figure. See Figures S11 and S12 for a gallery of all contact sites in the tomogram (E) and corresponding line profiles. Scale bars: 3 μm in (A), 1 μm in (B)–(D). 200 nm in (E) and (F), and 50 nm in (G)–(K).

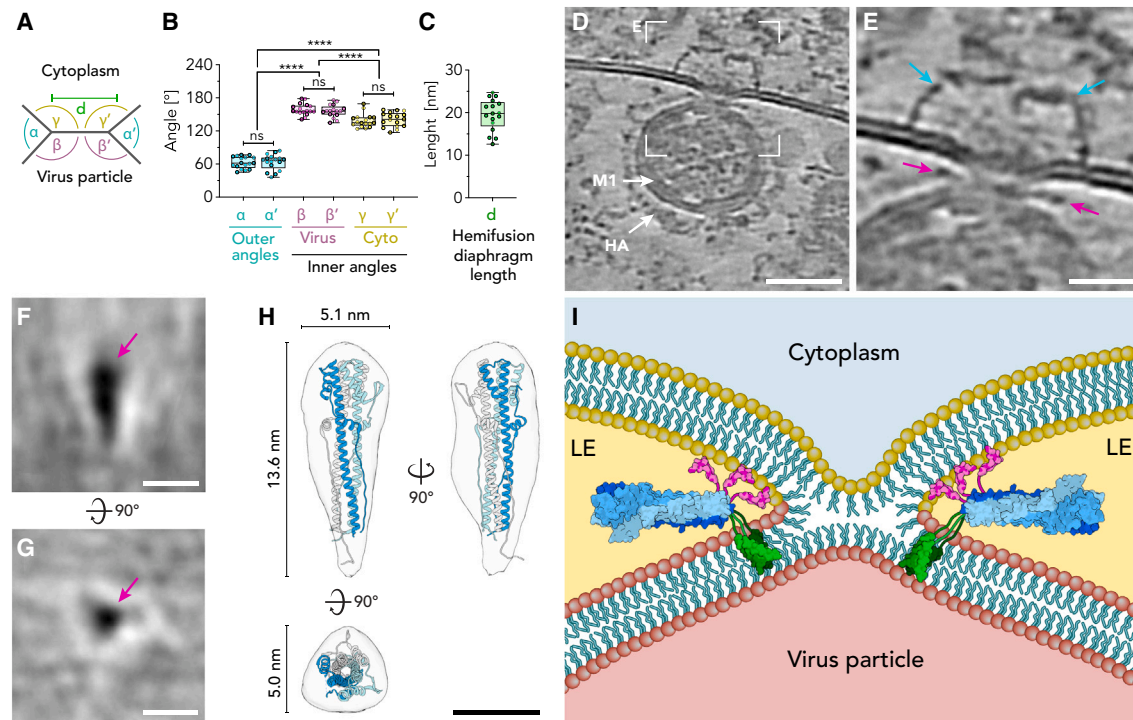


Figure 5. Post-fusion HA glycoproteins are localized at the hemifusion diaphragm

(A–C) The geometry of hemifusion diaphragms was analyzed by measurements of angles (B) and diaphragm size (C) for individual hemifusion sites ($n = 17$). The following angles are defined as indicated in the schematic (A): outer angles (α and α'), inner angles facing the viral lumen (β and β'), and inner angles facing the cytoplasm (γ and γ'). Paired t test was performed to analyze the significance of the difference between pairs of angles and between groups of angles. Data are shown as Box and Whiskers plots indicating the median (center of box), 25% and 75% quartiles (bounds of box), minimum and maximum values (bars), and all data points.

(D) Magnified area of reconstructed tomogram (Figure 4E) showing a stabilized hemifusion site between IAV particle and late endosomal membrane. The image is rotated 90° compared with Figure 4E.

(E) Magnified area of the hemifusion diaphragm between the late endosomal membrane and virus particle (D). Electron-dense structures are localized orthogonal to the hemifusion diaphragm (magenta arrows), representing post-fusion HA glycoproteins at the diaphragm region. Close to the hemifusion site, two OMDPs were observed (cyan arrow).

(F–H) Subtomogram average of post-fusion HA localized at the hemifusion diaphragm. Central slices of the subtomogram average for side-view (F) and top-view (G) are shown. The electron-dense post-fusion HA is localized in the center (magenta arrow). The post-fusion HA2 structure (PDB: 1QU1)⁸ was fitted to the three-dimensional isosurface of the subtomogram average (H). See Figure S13 for all iterative steps of the subtomogram average analysis.

(I) Schematic model of a stabilized hemifusion diaphragm visualizing the membrane configuration and localization of post-fusion HA. Late endosomal phospholipids are shown in yellow and viral phospholipids in red. Lumina of the virus particle, cytoplasm, and late endosome (LE) are indicated. The trimeric post-fusion HA glycoprotein model without fusion peptide (PDB: 1QU1)⁸ is shown in blue, with each monomer shown in a different shade of blue, fusion peptides are shown in magenta (PDB: 1QU1).⁸ The transmembrane domain of HA is shown in green (PDB: 6HJR).⁵⁶ Statistical significance: * $p < 0.05$, ** $p < 0.01$, *** $p < 0.001$, **** $p < 0.0001$. Scale bars: 50 nm in (D), 20 nm in (E), 10 nm in (F) and (G), and 5 nm in (H).

5G, and S13; Video S5) with a dimension of $13.6 \times 5.1 \times 5.0$ nm, overall consistent with the HA post-fusion conformation.⁴ The crystal structure of the post-fusion HA2⁵ was fitted to the electron density of the subtomogram average (Figure 5H) with high accuracy (97.1% atoms inside the isosurface). Hence, the observed density at the hemifusion diaphragm likely represents the viral HA glycoprotein in its post-fusion state. No densities corresponding to HA1 subunits were evident, presumably because of HA1 dissociation at reducing conditions of endosomes.⁵⁸ In addition to the HA2 density, the average revealed both the endosomal and the viral membranes (Figure S13A, green dotted lines), confirming the high symmetric geometry of the hemifusion sites. On two occasions, the outer membrane dome protein (OMDP), a protein complex previously characterized by us,⁴⁸ was observed on the cytosolic site of the hemifu-

sion site (Figures 5D and 5E, cyan arrows). However, because our data show that IFITM3 blocks membrane fusion in the absence of OMDPs, it is unlikely that OMDPs play an important role in the antiviral function of IFITM3.

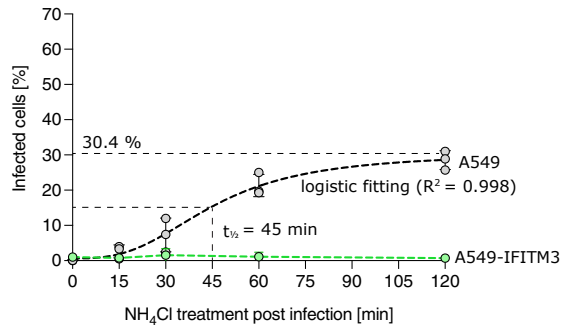
Hence, IFITM3 does not exclude viral fusion machinery from the fusion sites, and it does not interfere with the conformational transitions of the viral fusion protein, which is consistent with previous data showing that IFITM3 does not alter endosomal pH.¹⁶ This argues for the role of the IFITM3-lipid sorting activity in stabilizing the hemifusion state and shows that IFITM3 can inhibit a broad variety of viral fusion proteins.

IAV membrane fusion in non-inhibitory conditions

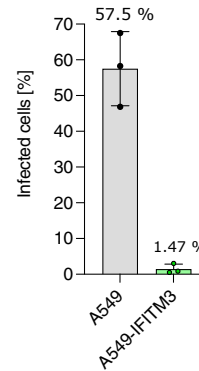
We finally aimed to compare the observed stabilized hemifusion sites in A549-IFITM3 cells (Figures 4 and 5) with non-inhibited

IAV viral entry half-time

A NH₄Cl treated



B Non-treated



IAV membrane fusion in late endosomes of A549 cells

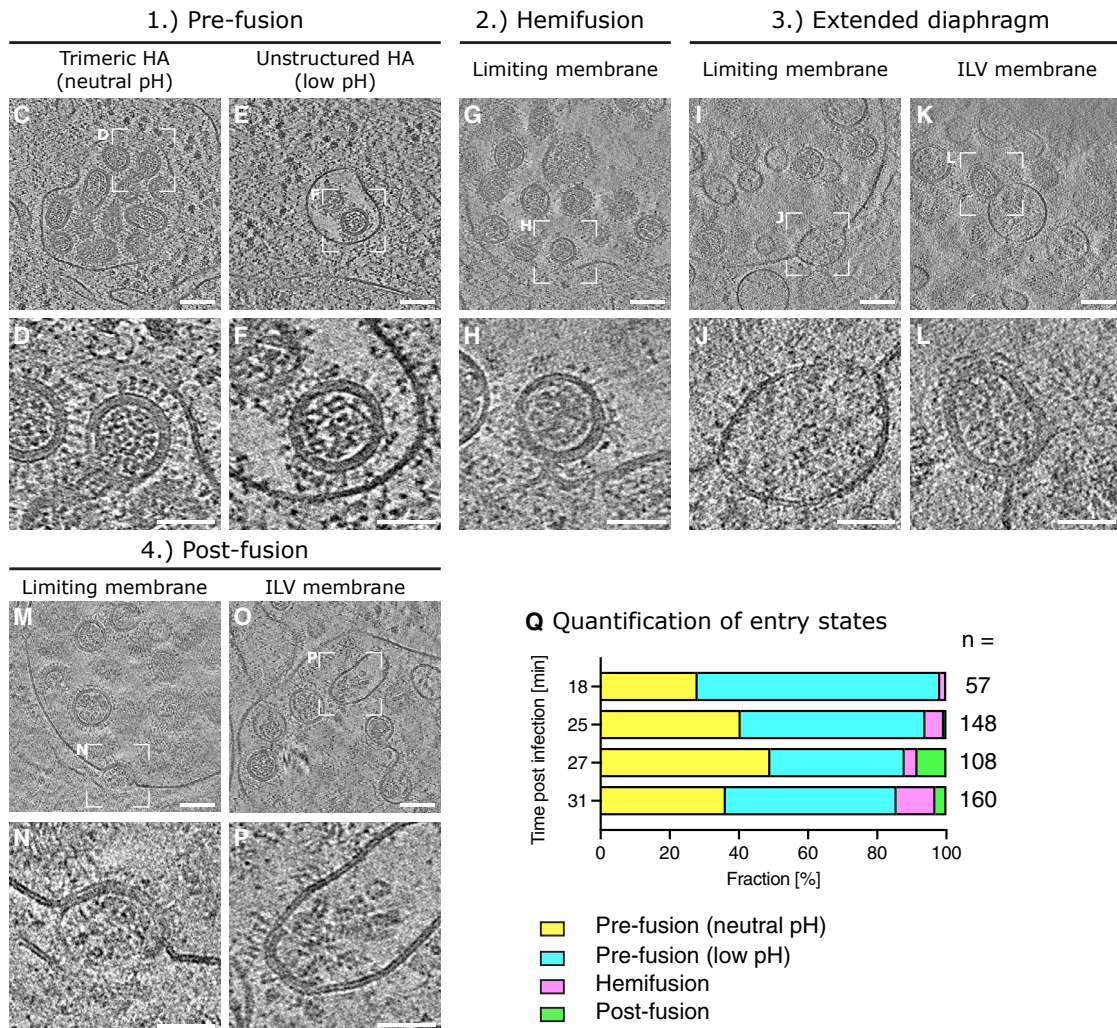


Figure 6. Temporal and structural analysis of IAV cell entry and membrane fusion in A549 cells

(A and B) IAV penetration assay by NH₄Cl add-in time course.

(A) A549 cells (black dotted line) and A549-IFITM3 cells (green dotted line) were infected with A/WSN/1933-PA-mScarlet (MOI = 3). Cells were treated with 50 mM NH₄Cl at different time points post-infection (0, 15, 30, 60, and 120 mpi) and fixed at 12–14 hpi. The percentage of infected cells was determined by fluorescence microscopy (see Figure S14 for a detailed analysis of the individual time points) in two independent experiments. For A549 cells, a four-parameter logistic (4PL)

(legend continued on next page)

IAV membrane fusion in wild-type A549 cells. To this aim, we infected A549 cells that do not express IFITM3 (Figures 1A and S1C) with the same infection conditions as the A549-IFITM3 cells (MOI = 200, 1 hpi). In a total of 9 tomograms of late endosomal organelles from 2 independent experiments, we could not observe any virus particles, indicating that in A549-IFITM3 cells, the observed hemifusion sites at 1 hpi are indeed stabilized by IFITM3.

To structurally characterize viral entry in A549 cells, we determined the timing of IAV membrane fusion in A549 cells by an infection time course (Figures 6A and 6B) in which NH_4Cl was added at different times post-infection. Because NH_4Cl rapidly diffuses through membranes and elevates endosomal pH,⁵⁹ this approach allows estimating the duration of IAV endocytic uptake till the onset of viral fusion.⁶⁰ The number of infected cells over time followed a sigmoidal curve with a half-time of 45 min post-infection (mpi) at which IAV endosomal membrane fusion is completed in 50% of the infected cells.

Based on these data, we structurally characterized IAV membrane fusion in LEs by *in situ* cryo-ET for time points between 18 and 31 mpi at a high MOI of 3×10^4 PFU/cell. In a total of 42 *in situ* cryo-electron tomograms, we captured 473 individual viral particles at different stages of viral entry. As an initial stage, we observed viral particles in early endosomal organelles featuring fully assembled M1 layers and HA spikes in prefusion conformation (40% of virions, $n = 187$), which indicates a neutral pH (Figures 6C and 6D). In addition, we captured virions harboring unstructured HA and partially disassembled M1 layer, indicating that virions were exposed to low pH in late endosomal compartments (51% of the virions, $n = 240$) (Figures 6E and 6F). Similar structural changes of HA glycoproteins and M1 layer were previously reported by *in vitro* cryo-ET studies of IAV particles subjected to low pH.^{36,61,62} We found 7% of the virions ($n = 31$) in a hemifusion state (Figures 6G, 6H, and S15). In a few cases ($n = 5$), we found the hemifusion diaphragm to be extended to a length of more than 200 nm (Figures 6I and 6J), although because of the small number of observations, it remains an open question if hemifusion expansion is a characteristic stage during IAV entry under uninhibited conditions. Finally, we were able to observe post-fusion states for 3% of the viral particles ($n = 15$) at the limiting late endosomal membrane (Figures 6M and 6N), as well as ILVs (Figures 6O and 6P), with vRNPs already present at the cytoplasm or ILV lumen, whereas the unstructured HA localized at the inner leaflet of the endosomal membrane. Quantification of all entry events captured at different time points is summarized in Figure 6Q. Interestingly, we regularly observed patches of assembled M1 layer on the cytoplasmic side of the late endosomal membrane at post-fusion sites, indicating that a fully disassembled M1 layer might not be necessary for IAV membrane fusion. Viral particles in endosomes of A549-IFITM3 cells (Figures 4, 5, and S8–S12) showed a similar morphology to the pre-fusion viral particles with unstructured HA in A549 cells (Figures 6E and 6F),

although with the difference of accumulated hemifusion sites both at the limiting endosomal membrane and ILVs. This is particularly striking, because the stabilized hemifusion sites in A549-IFITM3 cells were observed at a much later time point of 1 hpi, where the majority of virus particles are expected to have already fused in non-inhibitory conditions of A549 cells (Figure 6A).

DISCUSSION

IFITM3 has evolved as a broad and unspecific host countermeasure against a wide range of viruses that enter the cell via the late endosomal pathway, such as IAV, West Nile virus, chikungunya virus, respiratory syncytial virus,¹² Sindbis and Semliki Forest virus,¹⁶ tick-borne encephalitis virus,⁶³ and filoviruses.⁶⁴ Therefore, it is likely to function through general principles of viral-host membrane fusion inhibition. However, despite its substantial medical importance, the underlying principles were not understood. We showed that the number of ILVs in the late endosomal lumen is not modulated by IFITM3, which contradicts the “fusion decoy” model.²² Atomistic MD simulations revealed that cholesterol specifically interacts with the palmitoylated Cys72, which was recently identified as essential for the antiviral properties of IFITM3.²¹ Furthermore, atomistic MD simulations in lipidic systems mimicking an endosomal membrane composition and binary POPC-cholesterol mixtures show that IFITM3, despite the interaction of cholesterol with palmitoylated Cys72, overall repels cholesterol from its vicinity. Cholesterol is being replaced by phospholipids, including LBPA. Interestingly, a recent study suggests that LBPA promotes IAV membrane fusion,⁶⁵ which further indicates that IFITM3 drives local lipid redistribution to disfavor IAV membrane fusion. Because IFITM3 is excluded from the hemifusion diaphragm because of its TM domain and the structure of the hemifusion diaphragm rim, our MD simulations data indicate that IFITM3 can locally modulate the bilayer lipid composition and thereby withdraw fusion-pore driving lipids from the hemifusion diaphragm. Furthermore, the mechanism by which IFITM3 depletes cholesterol from its vicinity does not depend on a particular amino acid region but is instead due to its overall conformational structure. Because IFITM proteins share a similar three-dimensional structure, it is plausible that the mechanism by which IFITM3 depletes cholesterol could be shared within this family of proteins.

Using membrane model systems, previous studies estimated that, although hemifusion takes place within 5–30 s, fusion pore formation can occur in the order of many seconds to minutes (20–200 s).^{51,65–69} Here, conducted continuum membrane modeling suggests that IFITM3-induced lipid sorting increases the energy barrier of fusion pore formation, leading up to 3 orders of magnitude increase in hemifusion dwell time (Figure 3G). Therefore, viruses are trapped in the LE and subjected to degradation by proteases and lipases in the endosomal-lysosomal

curve was fitted to the data ($R^2 = 0.998$), and the half-time for viral penetration was determined to be $t_{1/2} = 45$ min. Because of the low infection rates in A549-IFITM3 cells, curve fitting and determination of the half-time were not possible.

(B) Control infections in the absence of NH_4Cl treatment.

(C–P) Slices of cryo-electron tomograms capturing IAV particles in endosomal organelles at different stages of viral entry. A549 cells were infected with A/WSN/1933-PA-mScarlet (MOI = 3×10^4 PFU/mL) and plunge-frozen between 18 and 31 mpi. See also Figure S15 for a gallery of hemifusion sites.

(Q) Quantification of entry stages found at different times post-infection. Scale bars: 100 nm in (C), (E), (G), (I), (K), (M), and (O) and 50 nm in (D), (F), (H), (J), (L), (N), and (P).

system. Virus degradation is supported by the observation of rod-like structures with a diameter of 13.7 nm consistent with vRNPs presumably released upon viral degradation in LEs in the A549-IFITM3 cell line (Figures S8F and S8G). It remains to be seen whether the previously reported IFITM3 clustering in the membrane, which depends on IFITM3 palmitoylation,^{18,19} enhances a lipid sorting effect and thereby also the dwell time.

We directly visualized stabilized hemifusion during viral-induced membrane fusion in LEs of IFITM3 overexpressing A549 cells using correlative *in situ* cryo-ET, which revealed IAV arrested at the hemifusion state, hence confirming the previously proposed “hemifusion stabilization” hypothesis²² at molecular resolution. In accordance with these data, we could show different IAV entry and fusion events, including post-fusion endosomal escape in A549 wild-type cells under uninhibited conditions. Furthermore, subtomogram averaging revealed post-fusion HA localized close to the hemifusion sites, providing direct evidence that IFITM3 does not affect the fusogenic activity of the viral fusion protein. Because the backfolding of the extended HA intermediate to the coiled-coil post-fusion state is not inhibited, the energy released during this irreversible process was insufficient to overcome the energy barrier for fusion pore formation, supporting the IFITM3-induced lipid sorting as the principal inhibitory mechanism of IFITM3.

Limitations of the study

This study provides *in situ* cryo-ET datasets on viral membrane fusion directly inside LEs. This implies that membrane configurations might not be identified as clearly as in earlier *in vitro* studies using artificial membranes that often lack proteins. Nevertheless, our data quality is sufficiently good to differentiate tight docking events from hemifusion events unambiguously. Intermediates that occur during the transition between tight docking and hemifusion, however, can currently not be distinguished. To enhance the quality of our sampling, we restricted our full atomistic MD simulations to a single IFITM3 monomer embedded in a lipid bilayer with 300 lipids. By imposing this limitation, we ensured statistically consistent lipid distribution across three independent simulations in all systems. However, investigating the impact of IFITM3 clustering on lipid sorting necessitates a larger membrane patch and significantly longer simulation times to achieve convergence. In the future, such simulations could be performed with coarse-grained MD simulations, which have been shown before to be able to describe the function of TM proteins in specific lipid mixtures.⁷⁰ We limited our continuum modeling to the standard pathway of fusion. Although other off-pathway fusion events, such as so-called leaky-fusion, were reported for protein-free liposomal systems at low cholesterol concentrations (below 15 mol %) ^{50,71}, we did not observe any indications of such rupture events in our cell experiments. Furthermore, our continuum modeling only allows us to estimate the fold change resulting from IFITM3 presence, but the absolute time needed to complete the fusion reaction cannot be determined from the model.

STAR★METHODS

Detailed methods are provided in the online version of this paper and include the following:

- **KEY RESOURCES TABLE**
- **RESOURCE AVAILABILITY**
 - Lead contact
 - Materials availability
 - Data and code availability
- **EXPERIMENTAL MODEL AND SUBJECT DETAILS**
 - Human embryonic kidney 293 cells expressing SV40 large T antigen (HEK293T)
 - HEK293T-Master Cell Bank cells (HEK293T-MCB)
 - Madin-Darby canine kidney cells (MDCK)
 - A549 cells
 - A549 cells expressing IFITM3 (A549-IFITM3)
 - Influenza A virus (strain A/WSN/1933)
 - Fluorescently labeled influenza A virus (A/WSN/1933-nDiO)
 - Fluorescent influenza a reporter virus (A/WSN/1933-PA-mScarlet)
- **METHODS DETAILS**
 - Immunoblot analysis
 - Confocal fluorescent light microscopy
 - Colocalization analysis
 - Infection assay using wide-field fluorescent light microscopy
 - Beta-lactamase (Blam) membrane fusion assay
 - Viral entry assay by NH₄Cl add-in time course
 - Transmission electron tomography (ET)
 - Cholesterol-analog cross-linking and immunoprecipitation
 - Molecular dynamics simulations
 - Relative affinity and repulsion of lipid to IFITM3
 - Modeling of membrane fusion and lipid sorting
 - Pore Expansion energy barrier and first passage time
 - *In situ* cryo-correlative light and electron microscopy (cryo-CLEM)
 - Estimation of pore formation energy barrier based on cryo-EM data
 - Subtomogram averaging (STA)
- **QUANTIFICATION AND STATISTICAL ANALYSIS**

SUPPLEMENTAL INFORMATION

Supplemental information can be found online at <https://doi.org/10.1016/j.chom.2023.03.005>.

ACKNOWLEDGMENTS

We want to thank Frank Orth for providing a cover art suggestion used during the submission of the manuscript. We acknowledge access to the infrastructure and support provided by the Infectious Diseases Imaging Platform (IDIP) at the Center for Integrative Infectious Disease Research, Heidelberg, Germany, the Cryo-EM Network at the Heidelberg University (HD-cryoNet) (Germany), the Electron Microscopy Core Facility at EMBL, Heidelberg, Germany, the computational resources at CSC-IT Centre for Science Ltd. (Espoo, Finland), and IT support at BioQuant Heidelberg (Germany). We want to thank Dr. Marco Binder for access to the cDNA library and plasmids for lentiviral production, Prof. Ervin Fodor for providing plasmids for A/WSN/1933 reverse genetics system, and Prof. Andrew Mehle for providing plasmids for the fluorescently tagged PA. We want to thank Jana Koch and Dr. Pierre-Yves Lozach for providing the plasmids for Rab7 and LAMP1 and Prof. Stefan Pöhlmann for providing the plasmids for IFITM1 and IFITM2. We are grateful to Hwayoung Lee, Prof. Wonpil Im, and Prof. Howard Hang for providing us with the Cys72 palmitoylated IFITM3 initial structure for performing atomistic MD

simulations. This work was supported by a research grant from the Chica and Heinz Schaller Foundation (Schaller Research Group Leader Program) to P.C., N.R., R.B., C.L., J.M., and A.K. In addition, this work was funded by the Deutsche Forschungsgemeinschaft (DFG, German Research Foundation) Sonderforschungsbereich (SFB, Collaborative Research Centre) 1129 to Y.S., B.B., U.S.S., P.C., S.P., and S.K.; SFB TRR83 to F.L. and W.N.; DFG Ni 423/10-1 to D.B. and W.N.; TRR186 to B.B.; DFG-FNR EMSIVILIN to P.C. and M.W.-M.; G.G. acknowledges support by the Minerva Stiftung. The authors gratefully acknowledge the data storage service SDS@hd supported by the Ministry of Science, Research, and the Arts, Baden-Württemberg (MWK) and the DFG through grant INST 35/1314-1 FUGG and INST 35/1503-1 FUGG.

AUTHOR CONTRIBUTIONS

Conceptualization, investigation and formal analysis (creating stable cell line and reporter virus, confocal microscopy, Blam assay, immunoblotting, infection assay, NH₄Cl add-in assay, colocalization assay, ET, cryo-CLEM, *in situ* cryo-ET, STA), visualization, writing – original draft, S.K.; investigation and formal analysis (membrane modeling and theory, cholesterol affinity and repulsion model, energy barrier calculation from cryo-ET data), writing – original draft, G.G.; investigation and formal analysis (MD simulations design, computational resources, data curation, methodology), writing – original draft, F.L.; investigation (creation of reporter virus, infection assay, NH₄Cl add-in assay, viral entry assay, western blot analysis), C.L.; investigation and formal analysis (systems preparation and equilibration for MD simulations), D.B.; investigation and formal analysis (cholesterol labeling and IP), A.H.; formal analysis (cryo-ET), M.W.-M.; investigation (creation of stable cell line and reporter virus), N.R.; investigation (creation of stable cell line, Blam assay), R.B.; formal analysis (ET), M.H.; investigation (high-pressure frozen and freeze-substituted [HPF/FS] sample preparation), A.K.; investigation (immunoblotting, immunofluorescence), J.M.; investigation (cryo-EM sample preparation), investigation (ET data acquisition), M.S.; writing – review & editing, Y.S.; writing – review & editing, B.B.; writing – review & editing, W.N.; conceptualization, supervision, writing – review & editing, U.S.S.; conceptualization, investigation and formal analysis (*in situ* cryo-ET), funding acquisition, supervision, writing – original draft, writing – review & editing, P.C.

DECLARATION OF INTERESTS

The authors declare no competing interests.

INCLUSION AND DIVERSITY

We support inclusive, diverse, and equitable conduct of research.

Received: July 6, 2022

Revised: November 15, 2022

Accepted: March 6, 2023

Published: March 31, 2023

REFERENCES

1. Matlin, K.S., Reggio, H., Helenius, A., and Simons, K. (1981). Infectious entry pathway of influenza virus in a canine kidney cell line. *J. Cell Biol.* **91**, 601–613. <https://doi.org/10.1083/jcb.91.3.601>.
2. de Vries, E., Tscherne, D.M., Wienholts, M.J., Cobos-Jiménez, V., Scholte, F., García-Sastre, A., Rottier, P.J.M., and de Haan, C.A.M. (2011). Dissection of the influenza A virus endocytic routes reveals macropinocytosis as an alternative entry pathway. *PLoS Pathog.* **7**, e1001329. <https://doi.org/10.1371/journal.ppat.1001329>.
3. Bullough, P.A., Hughson, F.M., Skehel, J.J., and Wiley, D.C. (1994). Structure of influenza haemagglutinin at the pH of membrane fusion. *Nature* **371**, 37–43. <https://doi.org/10.1038/371037a0>.
4. Benton, D.J., Gambliin, S.J., Rosenthal, P.B., and Skehel, J.J. (2020). Structural transitions in influenza haemagglutinin at membrane fusion pH. *Nature* **583**, 150–153. <https://doi.org/10.1038/s41586-020-2333-6>.
5. Harrison, S.C. (2008). Viral membrane fusion. *Nat. Struct. Mol. Biol.* **15**, 690–698. <https://doi.org/10.1038/nsmb.1456>.
6. Chernomordik, L.V., Zimmerberg, J., and Kozlov, M.M. (2006). Membranes of the world unite! *J. Cell Biol.* **175**, 201–207. <https://doi.org/10.1083/jcb.200607083>.
7. Kemble, G.W., Danieli, T., and White, J.M. (1994). Lipid-anchored influenza hemagglutinin promotes hemifusion, not complete fusion. *Cell* **76**, 383–391. [https://doi.org/10.1016/0092-8674\(94\)90344-1](https://doi.org/10.1016/0092-8674(94)90344-1).
8. Chen, J., Skehel, J.J., and Wiley, D.C. (1999). N- and C-terminal residues combine in the fusion-pH influenza hemagglutinin HA2 subunit to form an N cap that terminates the triple-stranded coiled coil. *Proc. Natl. Acad. Sci. USA* **96**, 8967–8972. <https://doi.org/10.1073/pnas.96.16.8967>.
9. Chernomordik, L.V., and Kozlov, M.M. (2003). Protein-lipid interplay in fusion and fission of biological membranes. *Annu. Rev. Biochem.* **72**, 175–207. <https://doi.org/10.1146/annurev.biochem.72.121801.161504>.
10. Fuhrmans, M., Marelli, G., Smirnova, Y.G., and Müller, M. (2015). Mechanics of membrane fusion/pore formation. *Chem. Phys. Lipids* **185**, 109–128. <https://doi.org/10.1016/j.chemphyslip.2014.07.010>.
11. Brass, A.L., Huang, I.C., Benita, Y., John, S.P., Krishnan, M.N., Feeley, E.M., Ryan, B.J., Weyer, J.L., van der Weyden, L., Fikrig, E., et al. (2009). The IFITM proteins mediate cellular resistance to influenza A H1N1 virus, West Nile virus, and dengue virus. *Cell* **139**, 1243–1254. <https://doi.org/10.1016/j.cell.2009.12.017>.
12. Zani, A., and Yount, J.S. (2018). Antiviral protection by IFITM3 *in vivo*. *Curr. Clin. Microbiol. Rep.* **5**, 229–237. <https://doi.org/10.1007/s40588-018-0103-0>.
13. Ling, S., Zhang, C., Wang, W., Cai, X., Yu, L., Wu, F., Zhang, L., and Tian, C. (2016). Combined approaches of EPR and NMR illustrate only one transmembrane helix in the human IFITM3. *Sci. Rep.* **6**, 24029. <https://doi.org/10.1038/srep24029>.
14. Feeley, E.M., Sims, J.S., John, S.P., Chin, C.R., Pertel, T., Chen, L.M., Gaiha, G.D., Ryan, B.J., Donis, R.O., Elledge, S.J., et al. (2011). IFITM3 inhibits influenza A virus infection by preventing cytosolic entry. *PLoS Pathog.* **7**, e1002337. <https://doi.org/10.1371/journal.ppat.1002337>.
15. Narayana, S.K., Helbig, K.J., McCartney, E.M., Eyre, N.S., Bull, R.A., Eitahla, A., Lloyd, A.R., and Beard, M.R. (2015). The interferon-induced transmembrane proteins, IFITM1, IFITM2, and IFITM3 inhibit hepatitis C virus entry. *J. Biol. Chem.* **290**, 25946–25959. <https://doi.org/10.1074/jbc.M115.657346>.
16. Weston, S., Czieso, S., White, I.J., Smith, S.E., Wash, R.S., Diaz-Soria, C., Kellam, P., and Marsh, M. (2016). Alphavirus restriction by IFITM proteins. *Traffic* **17**, 997–1013. <https://doi.org/10.1111/tra.12416>.
17. Weston, S., Czieso, S., White, I.J., Smith, S.E., Kellam, P., and Marsh, M. (2014). A membrane topology model for human interferon inducible transmembrane Protein 1. *PLoS One* **9**, e104341. <https://doi.org/10.1371/journal.pone.0104341>.
18. Chesarino, N.M., Compton, A.A., McMichael, T.M., Kenney, A.D., Zhang, L., Soewarna, V., Davis, M., Schwartz, O., and Yount, J.S. (2017). IFITM 3 requires an amphipathic helix for antiviral activity. *EMBO Rep.* **18**, 1740–1751. <https://doi.org/10.15252/embr.201744100>.
19. Yount, J.S., Moltedo, B., Yang, Y.Y., Charron, G., Moran, T.M., López, C.B., and Hang, H.C. (2010). Palmitoylome profiling reveals S-palmitoylation-dependent antiviral activity of IFITM3. *Nat. Chem. Biol.* **6**, 610–614. <https://doi.org/10.1038/nchembio.405>.
20. Benfield, C.T., MacKenzie, F., Ritzefeld, M., Mazzon, M., Weston, S., Tate, E.W., Teo, B.H., Smith, S.E., Kellam, P., Holmes, E.C., et al. (2020). Bat IFITM3 restriction depends on S-palmitoylation and a poly-morphic site within the CD225 domain. *Life Sci. Alliance* **3**, e201900542. <https://doi.org/10.26508/lsa.201900542>.
21. Garst, E.H., Lee, H., Das, T., Bhattacharya, S., Percher, A., Wiewiora, R., Witte, I.P., Li, Y., Peng, T., Im, W., et al. (2021). Site-specific lipidation enhances IFITM3 membrane interactions and antiviral activity. *ACS Chem. Biol.* **16**, 844–856. <https://doi.org/10.1021/acscchembio.1c00013>.
22. Desai, T.M., Marin, M., Chin, C.R., Savidis, G., Brass, A.L., and Melikyan, G.B. (2014). IFITM3 Restricts influenza A virus Entry by Blocking the Formation of Fusion Pores following Virus-Endosome Hemifusion.

- PLoS Pathog. 10, e1004048. <https://doi.org/10.1371/journal.ppat.1004048>.
23. Guo, X., Steinkühler, J., Marin, M., Li, X., Lu, W., Dimova, R., and Melikyan, G.B. (2021). Interferon-induced transmembrane protein 3 blocks fusion of diverse enveloped viruses by altering mechanical properties of cell membranes. *ACS Nano* 15, 8155–8170. <https://doi.org/10.1021/acsnano.0c10567>.
24. Amini-Bavil-Olyae, S., Choi, Y.J., Lee, J.H., Shi, M., Huang, I.C., Farzan, M., and Jung, J.U. (2013). The antiviral effector IFITM3 disrupts intracellular cholesterol homeostasis to block viral entry. *Cell Host Microbe* 13, 452–464. <https://doi.org/10.1016/j.chom.2013.03.006>.
25. Kühnl, A., Musiol, A., Heitzig, N., Johnson, D.E., Ehrhardt, C., Grewal, T., Gerke, V., Ludwig, S., and Rescher, U. (2018). Late endosomal/lysosomal cholesterol accumulation is a host cell-protective mechanism inhibiting endosomal escape of influenza A virus. *mBio* 9, e01345–e01318. <https://doi.org/10.1128/mBio.01345-18>.
26. Das, T., Yang, X., Lee, H., Garst, E.H., Valencia, E., Chandran, K., Im, W., and Hang, H.C. (2022). S -Palmitoylation and sterol interactions mediate antiviral specificity of IFITMs. *ACS Chem. Biol.* 17, 2109–2120. <https://doi.org/10.1021/acscchembio.2c00176>.
27. Kummer, S., Avinoam, O., and Kräusslich, H.G. (2019). IFITM3 clusters on virus containing endosomes and lysosomes early in the influenza A infection of human airway epithelial cells. *Viruses* 11, 548. <https://doi.org/10.3390/v11060548>.
28. Tscherne, D.M., Manicassamy, B., and García-Sastre, A. (2010). An enzymatic virus-like particle assay for sensitive detection of virus entry. *J. Virol. Methods* 163, 336–343. <https://doi.org/10.1016/j.jviromet.2009.10.020>.
29. Kobayashi, T., Beuchat, M.H., Chevallier, J., Makino, A., Mayran, N., Escola, J.M., Lebrand, C., Cosson, P., Kobayashi, T., and Gruenberg, J. (2002). Separation and characterization of late endosomal membrane domains. *J. Biol. Chem.* 277, 32157–32164. <https://doi.org/10.1074/jbc.M202838200>.
30. Van Meer, G., Voelker, D.R., and Feigenson, G.W. (2008). Membrane lipids: where they are and how they behave. *Nat. Rev. Mol. Cell Biol.* 9, 112–124. <https://doi.org/10.1038/nrm2330>.
31. Suddala, K.C., Lee, C.C., Meraner, P., Marin, M., Markosyan, R.M., Desai, T.M., Cohen, F.S., Brass, A.L., and Melikyan, G.B. (2019). Interferon-induced transmembrane protein 3 blocks fusion of sensitive but not resistant viruses by partitioning into virus-carrying endosomes. *PLoS Pathog.* 15, e1007532. <https://doi.org/10.1371/journal.ppat.1007532>.
32. Akimov, S.A., Molotkovsky, R.J., Kuzmin, P.I., Galimzyanov, T.R., and Batishchev, O.V. (2020). Continuum models of membrane fusion: evolution of the theory. *Int. J. Mol. Sci.* 21, 1–36. <https://doi.org/10.3390/ijms21113875>.
33. Kozlovsky, Y., Chernomordik, L.V., and Kozlov, M.M. (2002). Lipid intermediates in membrane fusion: formation, structure, and decay of hemifusion diaphragm. *Biophys. J.* 83, 2634–2651. [https://doi.org/10.1016/S0006-3495\(02\)75274-0](https://doi.org/10.1016/S0006-3495(02)75274-0).
34. Golani, G., Leikina, E., Melikov, K., Whitlock, J.M., Gamage, D.G., Luoma-Overstreet, G., Millay, D.P., Kozlov, M.M., and Chernomordik, L.V. (2021). Myomerger promotes fusion pore by elastic coupling between proximal membrane leaflets and hemifusion diaphragm. *Nat. Commun.* 12, 495. <https://doi.org/10.1038/s41467-020-20804-x>.
35. Kasson, P.M., and Pande, V.S. (2007). Control of membrane fusion mechanism by lipid composition: predictions from ensemble molecular dynamics. *PLoS Comput. Biol.* 3, e220. <https://doi.org/10.1371/journal.pcbi.0030220>.
36. Lee, K.K. (2010). Architecture of a nascent viral fusion pore. *EMBO J.* 29, 1299–1311. <https://doi.org/10.1038/emboj.2010.13>.
37. Portet, T., and Dimova, R. (2010). A new method for measuring edge tensions and stability of lipid bilayers: effect of membrane composition. *Biophys. J.* 99, 3264–3273. <https://doi.org/10.1016/j.bpj.2010.09.032>.
38. Chernomordik, L., Chanturiya, A., Green, J., and Zimmerberg, J. (1995). The hemifusion intermediate and its conversion to complete fusion: regulation by membrane composition. *Biophys. J.* 69, 922–929. [https://doi.org/10.1016/S0006-3495\(95\)79966-0](https://doi.org/10.1016/S0006-3495(95)79966-0).
39. Hamm, M., and Kozlov, M.M. (2000). Elastic energy of tilt and bending of fluid membranes. *Eur. Phys. J. E* 3, 323–335. <https://doi.org/10.1007/s101890070003>.
40. Helfrich, W. (1973). Elastic properties of lipid bilayers: theory and possible experiments. *Z. Naturforsch. C* 28, 693–703. <https://doi.org/10.1515/znc-1973-11-1209>.
41. Gu, R.X., Baoukina, S., and Tieleman, D.P. (2019). Cholesterol flip-flop in heterogeneous membranes. *J. Chem. Theor. Comput.* 15, 2064–2070. <https://doi.org/10.1021/acs.jctc.8b00933>.
42. Klein, S., Wachsmuth-Melm, M., Winter, S.L., Kolovou, A., and Chlanda, P. (2021). Cryo-correlative light and electron microscopy workflow for cryo-focused ion beam milled adherent cells. *Methods Cell Biol.* 162, 273–302. <https://doi.org/10.1016/bs.mcb.2020.12.009>.
43. Rigort, A., Bäuerlein, F.J.B., Villa, E., Eibauer, M., Laugks, T., Baumeister, W., and Pfitzko, J.M. (2012). Focused ion beam micromachining of eukaryotic cells for cryoelectron tomography. *Proc. Natl. Acad. Sci. USA* 109, 4449–4454. <https://doi.org/10.1073/pnas.1201333109>.
44. Marko, M., Hsieh, C., Schalek, R., Frank, J., and Mannella, C. (2007). Focused-ion-beam thinning of frozen-hydrated biological specimens for cryo-electron microscopy. *Nat. Methods* 4, 215–217. <https://doi.org/10.1038/nmeth1014>.
45. Dourmashkin, R.R., and Tyrrell, D.A.J. (1974). Electron microscopic observations on the entry of influenza virus into susceptible cells. *J. Gen. Virol.* 24, 129–141. <https://doi.org/10.1099/0022-1317-24-1-129>.
46. Dou, D., Revol, R., Östbye, H., Wang, H., and Daniels, R. (2018). Influenza A virus cell entry, replication, virion assembly and movement. *Front. Immunol.* 9, 1581. <https://doi.org/10.3389/fimmu.2018.01581>.
47. Kumar, V., Butcher, S.J., Öörni, K., Engelhardt, P., Heikkonen, J., Kaski, K., Ala-Korpela, M., and Kovanen, P.T. (2011). Three-dimensional cryoEM reconstruction of native LDL particles to 16Å resolution at physiological body temperature. *PLoS One* 6, e18841. <https://doi.org/10.1371/journal.pone.0018841>.
48. Klein, S., Wimmer, B.H., Winter, S.L., Kolovou, A., Laketa, V., and Chlanda, P. (2021). Post-correlation on-lamella cryo-CLEM reveals the membrane architecture of lamellar bodies. *Commun. Biol.* 4, 137. <https://doi.org/10.1038/s42003-020-01567-z>.
49. Fontana, J., Cardone, G., Heymann, J.B., Winkler, D.C., and Steven, A.C. (2012). Structural changes in influenza virus at low pH characterized by cryo-electron tomography. *J. Virol.* 86, 2919–2929. <https://doi.org/10.1128/JVI.06698-11>.
50. Chlanda, P., Mekhedov, E., Waters, H., Schwartz, C.L., Fischer, E.R., Ryham, R.J., Cohen, F.S., Blank, P.S., and Zimmerberg, J. (2016). The hemifusion structure induced by influenza virus haemagglutinin is determined by physical properties of the target membranes. *Nat. Microbiol.* 1, 16050. <https://doi.org/10.1038/nmicrobiol.2016.50>.
51. Gui, L., Ebner, J.L., Mileant, A., Williams, J.A., and Lee, K.K. (2016). Visualization and sequencing of membrane remodeling leading to influenza virus fusion. *J. Virol.* 90, 6948–6962. <https://doi.org/10.1128/JVI.00240-16>.
52. Calder, L.J., and Rosenthal, P.B. (2016). Cryomicroscopy provides structural snapshots of influenza virus membrane fusion. *Nat. Struct. Mol. Biol.* 23, 853–858. <https://doi.org/10.1038/nsmb.3271>.
53. Mangala Prasad, V., Blijleven, J.S., Smit, J.M., and Lee, K.K. (2022). Visualization of conformational changes and membrane remodeling leading to genome delivery by viral class-II fusion machinery. *Nat. Commun.* 13, 4772. <https://doi.org/10.1038/s41467-022-32431-9>.
54. Le Blanc, I., Luyet, P.P., Pons, V., Ferguson, C., Emans, N., Petiot, A., Mayran, N., Demareux, N., Fauré, J., Sadouli, R., et al. (2005). Endosome-to-cytosol transport of viral nucleocapsids. *Nat. Cell Biol.* 7, 653–664. <https://doi.org/10.1038/ncb1269>.

55. Perrin, P., Janssen, L., Janssen, H., van den Broek, B., Voortman, L.M., van Elsland, D., Berlin, I., and Neefjes, J. (2021). Retrofusion of intraluminal MVB membranes parallels viral infection and coexists with exosome release. *Curr. Biol.* *31*, 3884–3893.e4. <https://doi.org/10.1016/j.cub.2021.06.022>.
56. Benton, D.J., Nans, A., Calder, L.J., Turner, J., Neu, U., Lin, Y.P., Ketelaars, E., Kallewaard, N.L., Corti, D., Lanzavecchia, A., et al. (2018). Influenza hemagglutinin membrane anchor. *Proc. Natl. Acad. Sci. USA* *115*, 10112–10117. <https://doi.org/10.1073/pnas.1810927115>.
57. Risselada, H.J., and Grubmüller, H. (2021). How proteins open fusion pores: insights from molecular simulations. *Eur. Biophys. J.* *50*, 279–293. <https://doi.org/10.1007/s00249-020-01484-3>.
58. Hastings, K.T., and Cresswell, P. (2011). Disulfide reduction in the endocytic pathway: immunological functions of gamma-interferon-inducible lysosomal thiol reductase. *Antioxid. Redox Signal.* *15*, 657–668. <https://doi.org/10.1089/ars.2010.3684>.
59. Ohkuma, S., and Poole, B. (1978). Fluorescence probe measurement of the intralysosomal pH in living cells and the perturbation of pH by various agents. *Proc. Natl. Acad. Sci. USA* *75*, 3327–3331. <https://doi.org/10.1073/pnas.75.7.3327>.
60. Lozach, P.Y., Mancini, R., Bitto, D., Meier, R., Oestereich, L., Överby, A.K., Pettersson, R.F., and Helenius, A. (2010). Entry of bunyaviruses into mammalian cells. *Cell Host Microbe* *7*, 488–499. <https://doi.org/10.1016/j.chom.2010.05.007>.
61. Calder, L.J., Wasilewski, S., Berriman, J.A., and Rosenthal, P.B. (2010). Structural organization of a filamentous influenza A virus. *Proc. Natl. Acad. Sci. USA* *107*, 10685–10690. <https://doi.org/10.1073/pnas.1002123107>.
62. Fontana, J., and Steven, A.C. (2013). At low pH, influenza virus matrix protein M1 undergoes a conformational change prior to dissociating from the membrane. *J. Virol.* *87*, 5621–5628. <https://doi.org/10.1128/JVI.00276-13>.
63. Chmielewska, A.M., Gómez-Herranz, M., Gach, P., Nekulova, M., Bagnucka, M.A., Lipińska, A.D., Rychlowski, M., Hoffmann, W., Król, E., Vojtesek, B., et al. (2022). The role of IFITM proteins in tick-borne encephalitis virus infection. *J. Virol.* *96*, e0113021. <https://doi.org/10.1128/JVI.01130-21>.
64. Huang, I.C., Bailey, C.C., Weyer, J.L., Radoshitzky, S.R., Becker, M.M., Chiang, J.J., Brass, A.L., Ahmed, A.A., Chi, X., Dong, L., et al. (2011). Distinct patterns of IFITM-mediated restriction of filoviruses, SARS coronavirus, and influenza A virus. *PLoS Pathog.* *7*, e1001258. <https://doi.org/10.1371/journal.ppat.1001258>.
65. Mannsverk, S., Villamil Giraldo, A.M., and Kasson, P.M. (2022). Influenza virus membrane fusion is promoted by the endosome-resident phospholipid Bis(monoacylglycerol)phosphate. *J. Phys. Chem. B* *126*, 10445–10451. <https://doi.org/10.1021/acs.jpcc.2c06642>.
66. Floyd, D.L., Ragains, J.R., Skehel, J.J., Harrison, S.C., and van Oijen, A.M. (2008). Single-particle kinetics of influenza virus membrane fusion. *Proc. Natl. Acad. Sci. USA* *105*, 15382–15387. <https://doi.org/10.1073/pnas.0807771105>.
67. Ivanovic, T., Choi, J.L., Whelan, S.P., van Oijen, A.M., and Harrison, S.C. (2013). Influenza-virus membrane fusion by cooperative fold-back of stochastically induced hemagglutinin intermediates. *eLife* *2*, e00333. <https://doi.org/10.7554/eLife.00333>.
68. Liu, K.N., and Boxer, S.G. (2020). Target membrane cholesterol modulates single influenza virus membrane fusion efficiency but not rate. *Biophys. J.* *118*, 2426–2433. <https://doi.org/10.1016/j.bpj.2020.03.021>.
69. Liu, K.N., and Boxer, S.G. (2021). Single-virus content-mixing assay reveals cholesterol-enhanced influenza membrane fusion efficiency. *Biophys. J.* *120*, 4832–4841. <https://doi.org/10.1016/j.bpj.2021.09.023>.
70. Corradi, V., Mendez-Villuendas, E., Ingólfsson, H.I., Gu, R.X., Siuda, I., Melo, M.N., Moussatova, A., DeGagné, L.J., Sejdiu, B.I., Singh, G., et al. (2018). Lipid–protein interactions are unique fingerprints for membrane proteins. *ACS Cent. Sci.* *4*, 709–717. <https://doi.org/10.1021/acscentsci.8b00143>.
71. Haldar, S., Mekhedov, E., McCormick, C.D., Blank, P.S., and Zimmerberg, J. (2018). Lipid-dependence of target membrane stability during influenza viral fusion. *J. Cell Sci.* *132*, 218321. <https://doi.org/10.1242/jcs.218321>.
72. Lawson, C.L., Patwardhan, A., Baker, M.L., Hryc, C., Garcia, E.S., Hudson, B.P., Lagerstedt, I., Ludtke, S.J., Pintilie, G., Sala, R., et al. (2016). EMDDataBank unified data resource for 3DEM. *Nucleic Acids Res.* *44*, D396–D403. <https://doi.org/10.1093/nar/gkv1126>.
73. Sarkans, U., Gostev, M., Athar, A., Behrang, E., Melnichuk, O., Ali, A., Minguet, J., Rada, J.C., Snow, C., Tikhonov, A., et al. (2018). The BioStudies database—one stop shop for all data supporting a life sciences study. *Nucleic Acids Res.* *46*, D1266–D1270. <https://doi.org/10.1093/nar/gkx965>.
74. Giard, D.J., Aaronson, S.A., Todaro, G.J., Arnstein, P., Kersey, J.H., Dosik, H., and Parks, W.P. (1973). In vitro cultivation of human tumors: establishment of cell lines derived from a series of solid tumors. *J. Natl. Cancer Inst.* *51*, 1417–1423. <https://doi.org/10.1093/jnci/51.5.1417>.
75. Hoffmann, E., Neumann, G., Kawaoka, Y., Hobom, G., and Webster, R.G. (2000). A DNA transfection system for generation of influenza A virus from eight plasmids. *Proc. Natl. Acad. Sci. USA* *97*, 6108–6113. <https://doi.org/10.1073/pnas.100133697>.
76. Tran, V., Moser, L.A., Poole, D.S., and Mehle, A. (2013). Highly sensitive real-time in vivo imaging of an influenza reporter virus reveals dynamics of replication and spread. *J. Virol.* *87*, 13321–13329. <https://doi.org/10.1128/JVI.02381-13>.
77. Odon, V., Fros, J.J., Goonawardane, N., Dietrich, I., Ibrahim, A., Alshaiikhahmed, K., Nguyen, D., and Simmonds, P. (2019). The role of ZAP and OAS3/RNaseL pathways in the attenuation of an RNA virus with elevated frequencies of CpG and UpA dinucleotides. *Nucleic Acids Res.* *47*, 8061–8083. <https://doi.org/10.1093/nar/gkz581>.
78. Bindels, D.S., Haarbosch, L., Van Weeren, L., Postma, M., Wiese, K.E., Mastop, M., Aumonier, S., Gotthard, G., Royant, A., Hink, M.A., et al. (2017). MScarlet: A bright monomeric red fluorescent protein for cellular imaging. *Nat. Methods* *14*, 53–56. <https://doi.org/10.1038/nmeth.4074>.
79. Schindelin, J., Arganda-Carreras, I., Frise, E., Kaynig, V., Longair, M., Pietzsch, T., Preibisch, S., Rueden, C., Saalfeld, S., Schmid, B., et al. (2012). Fiji: an open-source platform for biological-image analysis. *Nat. Methods* *9*, 676–682. <https://doi.org/10.1038/nmeth.2019>.
80. Manders, E.M.M., Verbeek, F.J., and Aten, J.A. (1993). Measurement of co-localization of objects in dual-colour confocal images. *J. Microsc.* *169*, 375–382. <https://doi.org/10.1111/j.1365-2818.1993.tb03313.x>.
81. Sternberg, (1983). Biomedical image processing. *Computer* *16*, 22–34. <https://doi.org/10.1109/MC.1983.1654163>.
82. Schmidt, U., Weigert, M., Broaddus, C., and Myers, G. (2018). Cell detection with star-convex polygons. *Lect. Notes Comput. Sci.* *11071*, 265–273. https://doi.org/10.1007/978-3-030-00934-2_30.
83. Jones, D.M., and Padilla-Parra, S. (2016). The β -lactamase assay: harnessing a FRET biosensor to analyse viral fusion mechanisms. *Sensors (Basel)* *16*. <https://doi.org/10.3390/s16070950>.
84. Mastronarde, D.N. (2005). Automated electron microscope tomography using robust prediction of specimen movements. *J. Struct. Biol.* *152*, 36–51. <https://doi.org/10.1016/j.jsb.2005.07.007>.
85. Kremer, J.R., Mastronarde, D.N., and McIntosh, J.R. (1996). Computer visualization of three-dimensional image data using IMOD. *J. Struct. Biol.* *116*, 71–76. <https://doi.org/10.1006/jsbi.1996.0013>.
86. Lee, J., Cheng, X., Swails, J.M., Yeom, M.S., Eastman, P.K., Lemkul, J.A., Wei, S., Buckner, J., Jeong, J.C., Qi, Y., et al. (2016). CHARMM-GUI input generator for NAMD, GROMACS, AMBER, OpenMM, and CHARMM/OpenMM simulations using the CHARMM36 additive force field. *J. Chem. Theor. Comput.* *12*, 405–413. <https://doi.org/10.1021/acs.jctc.5b00935>.
87. Lee, J., Patel, D.S., Stähle, J., Park, S.J., Kern, N.R., Kim, S., Lee, J., Cheng, X., Valvano, M.A., Holst, O., et al. (2019). CHARMM-GUI membrane builder for complex biological membrane simulations with

- glycolipids and lipoglycans. *J. Chem. Theor. Comput.* *15*, 775–786. <https://doi.org/10.1021/acs.jctc.8b01066>.
88. Huang, J., and MacKerell, A.D. (2013). CHARMM36 all-atom additive protein force field: validation based on comparison to NMR data. *J. Comput. Chem.* *34*, 2135–2145. <https://doi.org/10.1002/jcc.23354>.
89. Huang, J., Rauscher, S., Nawrocki, G., Ran, T., Feig, M., de Groot, B.L., Grubmüller, H., and MacKerell, A.D. (2017). CHARMM36m: an improved force field for folded and intrinsically disordered proteins. *Nat. Methods* *14*, 71–73. <https://doi.org/10.1038/nmeth.4067>.
90. Pastor, R.W., and Mackerell, A.D. (2011). Development of the CHARMM Force Field for Lipids. *J. Phys. Chem. Lett.* *2*, 1526–1532. <https://doi.org/10.1021/jz200167q>.
91. Jorgensen, W.L., Chandrasekhar, J., Madura, J.D., Impey, R.W., and Klein, M.L. (1983). Comparison of simple potential functions for simulating liquid water. *J. Chem. Phys.* *79*, 926–935. <https://doi.org/10.1063/1.445869>.
92. Parrinello, M., and Rahman, A. (1981). Polymorphic transitions in single crystals: A new molecular dynamics method. *J. Appl. Phys.* *52*, 7182–7190. <https://doi.org/10.1063/1.328693>.
93. Hoover, W.G. (1985). Canonical dynamics: equilibrium phase-space distributions. *Phys. Rev. A Gen. Phys.* *31*, 1695–1697. <https://doi.org/10.1103/PhysRevA.31.1695>.
94. Nosé, S. (1984). A molecular dynamics method for simulations in the canonical ensemble. *Mol. Phys.* *52*, 255–268. <https://doi.org/10.1080/00268978400101201>.
95. Darden, T., York, D., and Pedersen, L. (1993). Particle mesh Ewald: an $N \cdot \log(N)$ method for Ewald sums in large systems. *J. Chem. Phys.* *98*, 10089–10092. <https://doi.org/10.1063/1.464397>.
96. Essmann, U., Perera, L., Berkowitz, M.L., Darden, T., Lee, H., and Pedersen, L.G. (1995). A smooth particle mesh Ewald method. *J. Chem. Phys.* *103*, 8577–8593. <https://doi.org/10.1063/1.470117>.
97. Hess, B., Bekker, H., Berendsen, H.J.C., and Fraaije, J.G.E.M. (1997). Lincs: A linear constraint solver for molecular simulations. *J. Comput. Chem.* *18*, 1463–1472. [https://doi.org/10.1002/\(SICI\)1096-987X\(199709\)18:12<1463::AID-JCC4>3.0.CO;2-H](https://doi.org/10.1002/(SICI)1096-987X(199709)18:12<1463::AID-JCC4>3.0.CO;2-H).
98. Abraham, M.J., Murtola, T., Schulz, R., Páll, S., Smith, J.C., Hess, B., and Lindahl, E. (2015). GROMACS: high performance molecular simulations through multi-level parallelism from laptops to supercomputers. *SoftwareX* *1–2*, 19–25. <https://doi.org/10.1016/j.softx.2015.06.001>.
99. Humphrey, W., Dalke, A., and Schulten, K. (1996). VMD: visual molecular dynamics. *J. Mol. Graph.* *14*, 33–38. [https://doi.org/10.1016/0263-7855\(96\)00018-5](https://doi.org/10.1016/0263-7855(96)00018-5).
100. Huotari, J., and Helenius, A. (2011). Endosome maturation. *EMBO J.* *30*, 3481–3500. <https://doi.org/10.1038/emboj.2011.286>.
101. Lorent, J.H., Levental, K.R., Ganesan, L., Rivera-Longworth, G., Sezgin, E., Doktorova, M., Lyman, E., and Levental, I. (2020). Plasma membranes are asymmetric in lipid unsaturation, packing and protein shape. *Nat. Chem. Biol.* *16*, 644–652. <https://doi.org/10.1038/s41589-020-0529-6>.
102. Zambrano, F., Fleischer, S., and Fleischer, B. (1975). Lipid composition of the Golgi apparatus of rat kidney and liver in comparison with other sub-cellular organelles. *Biochim. Biophys. Acta* *380*, 357–369. [https://doi.org/10.1016/0005-2760\(75\)90104-6](https://doi.org/10.1016/0005-2760(75)90104-6).
103. Kollmitzer, B., Heftberger, P., Rappolt, M., and Pabst, G. (2013). Monolayer spontaneous curvature of raft-forming membrane lipids. *Soft Matter* *9*, 10877–10884. <https://doi.org/10.1039/C3SM51829A>.
104. Fuller, N., and Rand, R.P. (2001). The influence of lysolipids on the spontaneous curvature and bending elasticity of phospholipid membranes. *Biophys. J.* *81*, 243–254. [https://doi.org/10.1016/S0006-3495\(01\)75695-0](https://doi.org/10.1016/S0006-3495(01)75695-0).
105. Zucker, B., Golani, G., and Kozlov, M.M. (2022). Model for ring closure in ER tubular network dynamics. *Biophys. J.* <https://doi.org/10.1016/j.bpj.2022.10.005>.
106. Kozlov, M.M., and Winterhalter, M. (1991). Elastic moduli for strongly curved monolayers. Position of the neutral surface. *J. Phys. II France.* *1*, 1077–1084. <https://doi.org/10.1051/jp2:1991201>.
107. Hamm, M., and Kozlov, M.M. (1998). Tilt model of inverted amphiphilic mesophases. *Eur. Phys. J. B* *6*, 519–528. <https://doi.org/10.1007/s100510050579>.
108. Dimova, R. (2014). Recent developments in the field of bending rigidity measurements on membranes. *Adv. Colloid Interface Sci.* *208*, 225–234. <https://doi.org/10.1016/j.cis.2014.03.003>.
109. Terzi, M.M., Ergüder, M.F., and Deserno, M. (2019). A consistent quadratic curvature-tilt theory for fluid lipid membranes. *J. Chem. Phys.* *151*, 164108. <https://doi.org/10.1063/1.5119683>.
110. Templer, R.H., Khoo, B.J., and Seddon, J.M. (1998). Gaussian curvature modulus of an amphiphilic monolayer. *Langmuir* *14*, 7427–7434. <https://doi.org/10.1021/la980701y>.
111. May, S., Kozlovsky, Y., Ben-Shaul, A., and Kozlov, M.M. (2004). Tilt modulus of a lipid monolayer. *Eur. Phys. J. E Soft Matter* *14*, 299–308. <https://doi.org/10.1140/epje/i2004-10019-y>.
112. Doktorova, M., Harries, D., and Khelashvili, G. (2017). Determination of bending rigidity and tilt modulus of lipid membranes from real-space fluctuation analysis of molecular dynamics simulations. *Phys. Chem. Chem. Phys.* *19*, 16806–16818. <https://doi.org/10.1039/c7cp01921a>.
113. Safran, S.A., Pincus, P., and Andelman, D. (1990). Theory of spontaneous vesicle formation in surfactant mixtures. *Science* *248*, 354–356. <https://doi.org/10.1126/science.248.4953.354>.
114. Kozlov, M.M., and Helfrich, W. (1992). Effects of a cosurfactant on the stretching and bending elasticities of a surfactant monolayer. *Langmuir* *8*, 2792–2797. <https://doi.org/10.1021/la00047a035>.
115. Akimov, S.A., Volynsky, P.E., Galimzyanov, T.R., Kuzmin, P.I., Pavlov, K.V., and Batishchev, O.V. (2017). Pore formation in lipid membrane I: Continuous reversible trajectory from intact bilayer through hydrophobic defect to transversal pore. *Sci. Rep.* *7*, 12152. <https://doi.org/10.1038/s41598-017-12127-7>.
116. Weaver, J.C., and Chizmadzhev, Y.A. (1996). Theory of electroporation: a review. *Bioelectrochem. Bioenerg.* *41*, 135–160. [https://doi.org/10.1016/S0302-4598\(96\)05062-3](https://doi.org/10.1016/S0302-4598(96)05062-3).
117. Chernomordik, L.V., Kozlov, M.M., Melikyan, G.B., Abidor, I.G., Markin, V.S., and Chizmadzhev, Y.A. (1985). The shape of lipid molecules and monolayer membrane fusion. *BBA Biomembr.* *812*, 643–655. [https://doi.org/10.1016/0005-2736\(85\)90257-3](https://doi.org/10.1016/0005-2736(85)90257-3).
118. Chanturiya, A., Chernomordik, L.V., and Zimmerberg, J. (1997). Flickering fusion pores comparable with initial exocytotic pores occur in protein-free phospholipid bilayers. *Proc. Natl. Acad. Sci. USA* *94*, 14423–14428. <https://doi.org/10.1073/pnas.94.26.14423>.
119. Taupin, C., Dvolaitzky, M., and Sauterey, C. (1975). Osmotic pressure induced pores in phospholipid vesicles. *Biochemistry* *14*, 4771–4775. <https://doi.org/10.1021/bi00692a032>.
120. Schorb, M., Gaechter, L., Avinoam, O., Sieckmann, F., Clarke, M., Bebeacua, C., Bykov, Y.S., Sonnen, A.F.-P., Lihl, R., and Briggs, J.A.G. (2017). New hardware and workflows for semi-automated correlative cryo-fluorescence and cryo-electron microscopy/tomography. *J. Struct. Biol.* *197*, 83–93. <https://doi.org/10.1016/j.jsb.2016.06.020>.
121. Schorb, M., and Sieckmann, F. (2017). Matrix MAPS—an intuitive software to acquire, analyze, and annotate light microscopy data for CLEM. *Methods Cell Biol.* *140*, 321–333. <https://doi.org/10.1016/bs.mcb.2017.03.012>.
122. Wagner, F.R., Watanabe, R., Schampers, R., Singh, D., Persoon, H., Schaffer, M., Fruhstorfer, P., Pitzko, J., and Villa, E. (2020). Preparing samples from whole cells using focused-ion-beam milling for cryo-electron tomography. *Nat. Protoc.* *15*, 2041–2070. <https://doi.org/10.1038/s41596-020-0320-x>.
123. Wolff, G., Limpens, R.W.A.L., Zheng, S., Snijder, E.J., Agard, D.A., Koster, A.J., and Bárcena, M. (2019). Mind the gap: micro-expansion

- joints drastically decrease the bending of FIB-milled cryo-lamellae. *J. Struct. Biol.* 208, 107389. <https://doi.org/10.1016/j.jsb.2019.09.006>.
124. Hagen, W.J.H., Wan, W., and Briggs, J.A.G. (2017). Implementation of a cryo-electron tomography tilt-scheme optimized for high resolution sub-tomogram averaging. *J. Struct. Biol.* 197, 191–198. <https://doi.org/10.1016/j.jsb.2016.06.007>.
125. Eisenstein, F., Yanagisawa, H., Kashihara, H., Kikkawa, M., Tsukita, S., and Danev, R. (2022). Parallel Cryo Electron Tomography on *In Situ* Lamellae (Biophysics). <https://doi.org/10.1101/2022.04.07.487557>.
126. Zheng, S.Q., Palovcak, E., Armache, J.P., Verba, K.A., Cheng, Y., and Agard, D.A. (2017). MotionCor2: anisotropic correction of beam-induced motion for improved cryo-electron microscopy. *Nat. Methods* 14, 331–332. <https://doi.org/10.1038/nmeth.4193>.
127. Buchholz, T.O., Krull, A., Shahidi, R., Pigino, G., Jékely, G., and Jug, F. (2019). Content-aware image restoration for electron microscopy. *Methods Cell Biol.* 152, 277–289. <https://doi.org/10.1016/bs.mcb.2019.05.001>.
128. Castaño-Díez, D., Kudryashev, M., Arheit, M., and Stahlberg, H. (2012). Dynamo: A flexible, user-friendly development tool for subtomogram averaging of cryo-EM data in high-performance computing environments. *J. Struct. Biol.* 178, 139–151. <https://doi.org/10.1016/j.jsb.2011.12.017>.
129. Pettersen, E.F., Goddard, T.D., Huang, C.C., Couch, G.S., Greenblatt, D.M., Meng, E.C., and Ferrin, T.E. (2004). UCSF Chimera - A visualization system for exploratory research and analysis. *J. Comput. Chem.* 25, 1605–1612. <https://doi.org/10.1002/jcc.20084>.
130. Chlanda, P., Schraidt, O., Kummer, S., Riches, J., Oberwinkler, H., Prinz, S., Kräusslich, H.G., and Briggs, J.A.G. (2015). Structural analysis of the roles of influenza A virus membrane-associated proteins in assembly and morphology. *J. Virol.* 89, 8957–8966. <https://doi.org/10.1128/JVI.00592-15>.
131. De Chaumont, F., Dallongeville, S., Chenouard, N., Hervé, N., Pop, S., Provoost, T., Meas-Yedid, V., Pankajakshan, P., Lecomte, T., Le Montagner, Y., et al. (2012). Icy: an open Biologie informatics platform for extended reproducible research. *Nat. Methods* 9, 690–696. <https://doi.org/10.1038/nmeth.2075>.
132. Van Rossum, G., and Drake, F.L. (2009). *Python 3 Reference Manual (CreateSpace)*.

STAR★METHODS

KEY RESOURCES TABLE

REAGENT or RESOURCE	SOURCE	IDENTIFIER
Antibodies		
Actin	Merck, Sigma-Aldrich	A5441; RRID: AB_476744
Caveolin 1 Polyclonal	ThermoFisher Scientific™	PA1-064; RRID: AB_2072027
IFITM1 Monoclonal	Proteintech Group Inc.	60074-1-Ig; RRID: AB_2233405
IFITM2 Monoclonal	Proteintech Group Inc.	66137-1-Ig; RRID: AB_2881536
IFITM3 Polyclonal	Proteintech Group Inc.	11714-1-AP; RRID: AB_2295684
M2	Santa Cruz Biotechnology, Inc.	sc-32238; RRID: AB_627808
Anit-Mouse IgGκ light chain binding protein (m-IgGκ BP)	Santa Cruz Biotechnology, Inc.	sc-516102; RRID: AB_2687626
Goat anti-Rabbit IgG (H+L) Cross-Adsorbed Secondary Antibody, Alexa Fluor™ 680	ThermoFisher Scientific™, Invitrogen	A21076; RRID: AB_2535736
Goat anti-Rabbit IgG (H+L) Highly Cross-Adsorbed Secondary Antibody, Alexa Fluor™ 633	ThermoFisher Scientific™, Invitrogen	A21071; RRID: AB_2535732
Mouse anti-Rabbit IgG-HRP	Santa Cruz Biotechnology, Inc.	sc-2357; RRID: AB_628497
Bacterial and virus strains		
A/WSN/1933(H1N1)	Hoffmann et al. ⁷⁵	N/A
A/WSN/1933(H1N1)-PA-mScarlet	This publication	N/A
<i>E. coli</i> Stellar™ Competent Cells	Takara Bio Inc.	636763
Chemicals, peptides, and recombinant proteins		
1-Hexadecene	Merck, Sigma-Aldrich	822064
Avicel	FMC Corporation	RC-581
Benzonase® Nuclease HC	Merck, Millipore	71206-25KUN
Biotin Azide	ThermoFisher Scientific™	B10184
Bovine Serum Albumin (BSA)	Merck, Sigma-Aldrich	A7030
CellBrite® Green Cytoplasmic Membrane Dye	Biotium	30021
Color Prestained Protein Standard, Broad Range (10-250 kDa)	New England Biolabs	P7719
Color Prestained Protein Standard, Broad Range (11-245 kDa)	New England Biolabs	P7712S
cOmplete™, Mini, EDTA-free Protease Inhibitor Cocktail	ThermoFisher Scientific™, Roche	4693159001
Crystal violet solution, 1%, aqueous solution	Merck, Sigma-Aldrich	V5265
CuSO ₄	Merck, Sigma-Aldrich	203165
CutSmart® Buffer	New England Biolabs	B7204
DAPI	Merck, Sigma-Aldrich	D9542
DMEM	ThermoFisher Scientific™, Gibco	11965092
DMEM, high glucose, GlutaMAX™	ThermoFisher Scientific™, Gibco	61965026
DMEM/F12	ThermoFisher Scientific™, Gibco	11320033
DMSO	Merck, Sigma-Aldrich	D2650
Fetal bovine serum (FBS)	ThermoFisher Scientific™, Gibco	10270-106
Fish skin gelatine (FSG)	Merck, Sigma-Aldrich	G7765
Glutaraldehyde	Merck, Sigma-Aldrich	G5882
Glycine	ThermoFisher Scientific™	10070150
HEPES	Carl Roth GmbH + Co. KG	9105.2
Hoechst 33342	Merck, Sigma-Aldrich	B2261

(Continued on next page)

Continued

REAGENT or RESOURCE	SOURCE	IDENTIFIER
Interferon beta-1a (IFN β -1a)	ImmunoTools GmbH	11343524
Interferon beta-1b (IFN β -1b)	ImmunoTools GmbH	11343543
Laemmli Sample Buffer (4x)	Bio-Rad Laboratories, Inc.	1610747
Bacto™ Yeast Extract (LB)	ThermoFisher Scientific™, Gibco	212750
Lowicryl® HM20 Non-polar, Hydrophobic, -70°C Embedding Kit	Polysciences Inc.	15924-1
Methanol	Honeywell	32213
Opti-MEM medium	ThermoFisher Scientific™, Gibco	31985062
Formaldehyde 37% (PFA)	Bernd Kraft GmbH	BK19916
Sylgard 184	Dow Corning Inc.	1673921
PBS	Merck, Sigma-Aldrich	D8537
Penicillin-Streptomycin (P/S) (10.000 units/ml)	ThermoFisher Scientific™	15140122
Photo-reactive clickable trans-Sterol probe (pacChol)	Merck, Sigma-Aldrich	804657
Pierce™ High Capacity NeutrAvidin™ Agarose	ThermoFisher Scientific™	29202
Polybrene infection reagent	Merck, Sigma-Aldrich	TR-1003-G
Polyethylenimine (PEI)	Polysciences	23966-1
ProLong™ Glass Antifade Mountant	ThermoFisher Scientific™, Invitrogen™	P36982
Protease inhibitor cocktail	Roche	11873580001
Protein-A gold 10 nm	Aurion	PA-80830/1
Puromycin	Merck, Sigma-Aldrich	P8833
Recombinant Human Interferon- β 1 α	ImmunoTools	11343520
Restriction Endonuclease BssHII	New England Biolabs	R0199S
Restriction Endonuclease XbaI	New England Biolabs	R0145S
S.O.C. medium	ThermoFisher Scientific™, Invitrogen™	15544034
SDS	Serva	20765.03
Sodium deoxycholate	D6750-25G	D6750
TBTA	Merck, Sigma-Aldrich	C4706
TCEP	Merck, Sigma-Aldrich	678937
TGS buffer (10x)	Bio-Rad	1610772
Trypsin from bovine pancreas, TPCK-treated	Merck, Sigma-Aldrich	T1426
Trans-Blot Turbo Mini 0.2 μ m PVDF Transfer Packs	Bio-Rad	1704156
TransIT®-2020 Transfection Reagent	Mirus Bio	MIR 5400
TransIT®-293 Transfection Reagent	Mirus Bio	MIR 2700
TransIT®-LT1 Transfection Reagent	Mirus Bio	MIR 2300
Triton™ X-100	Merck, Sigma-Aldrich	X100
Trypsin inhibitor from Glycine max (soybean)	Merck, Sigma-Aldrich	T9128
Tween® 20	Carl Roth GmbH + Co. KG	9127.1
Precision Plus Protein™ All Blue Prestained Protein Standards by Bio-Rad	Bio-Rad	1610373
Uranyl acetate	SERVA Electrophoresis GmbH	77870
Critical commercial assays		
Infusion® HD Cloning Kit	Takara Bio Inc.	639649
CloneAmp™ HiFi PCR Premix	Takara Bio Inc.	638500
Cloning Enhancer	Takara Bio Inc.	639615
Gateway™ LR Clonase™ Enzyme Mix	ThermoFisher Scientific, Invitrogen™	11791019
Tricine gel	ThermoFisher Scientific	EC66252BOX
NucleoSpin Gel and PCR Clean-up Kit	MACHEREY-NAGEL	740609.50

(Continued on next page)

Continued

REAGENT or RESOURCE	SOURCE	IDENTIFIER
QIAprep Spin Miniprep Kit	QIAGEN	27104
Beta-Lactamase Loading Solutions Kit	ThermoFisher Scientific, Invitrogen™	K1085
LiveBLAzer™ FRET B/G (CCF4-AM)	ThermoFisher Scientific, Invitrogen™	K1089
Pierce™ BCA Protein Assay Kit	ThermoFisher Scientific	23227
QIAGEN Plasmid Maxi Kit	QIAGEN	12163
Lenti-X™ GoStix	Takara Bio Inc.	631280

Deposited data

MD simulation data	https://doi.org/10.5281/zenodo.6599836	N/A
<i>In situ</i> cryo-ET data	EMDB: EMD-15130, EMDB: EMD-15131, EMDB: EMD15132, EMDB: EMD-15133, EMDB: EMD-16129, EMDB: EMD-16130, EMDB: EMD-16131, EMDB: EMD-16132, EMDB: EMD-16133	N/A
Line profile measurements	BioStudies: S-BIAD539	N/A
HPF/FS ET data	EMDB: EMD-15705, EMDB: EMD-15707, EMDB: EMD15708	N/A
Fluorescence light microscopy data	BioStudies: S-BIAD539	N/A
Western blot data	BioStudies: S-BIAD539	N/A
MATLAB code for membrane modeling	https://github.com/GonenGolani/Fusion_Solver	N/A

Experimental models: Cell lines

A549	American Type Culture Collection (ATCC)	CCL-185
A549-IFITM3	This publication	N/A
HEK293T	American Type Culture Collection (ATCC)	CRL-3216
HEK293T-MCB	Dr. Marco Binder (DKFZ, Heidelberg, Germany)	N/A
MDCK	Prof. João Amorim (Instituto Gulbenkian de Ciência, Portugal)	N/A

Oligonucleotides

Reverse sequencing primer IRES-rev (TATAGACAAACGCACACCG)	Microsynth	N/A
Forward overhang primer for cloning (CCCAGCCCTGCGCGCGGCGAG CAATGGTGTCCAAGGGTGAAGC)	This publication	N/A
Reverse overhang primer for cloning (AAGCAGTTTTCTAGATCACTTGTA CAGCTCATCCATTCCAC)	This publication	N/A
Forward primer for sequencing (GGCAAACAACAGATGG CTGGCAAC)	This publication	N/A
Reverse primer for sequencing (GTATGCATCTCCACAACACTAGAAGG)	This publication	N/A

Recombinant DNA

pCAGGS-A/Hong Kong/1968-HA	Chlanda et al. ¹³⁰	N/A
pCAGGS-A/Singapore/1957-NA	Chlanda et al. ¹³⁰	N/A
pCAGGS-M1-Blam	Tscherne et al. ²⁸	N/A
pENTR221-clone3728-IFITM3	Dr. Marco Binder (DKFZ, Heidelberg, Germany)	N/A
pCAGGS-IFITM1	Prof. Stefan Pöhlmann	N/A
pCAGGS-IFITM2	Prof. Stefan Pöhlmann	N/A
pWPI-IRES-Puro	Dr. Marco Binder (DKFZ, Heidelberg, Germany)	N/A

(Continued on next page)

Continued

REAGENT or RESOURCE	SOURCE	IDENTIFIER
pWPI-IFITM3	This publication	N/A
pCMV-VSV-G	addgene	8454
psPAX2	addgene	12260
pAdVantage™	Promega	E1711
pHW2000-PB1-WSN	Prof. Ervin Fodor (University of Oxford, UK)	N/A
pHW2000-PB2-WSN	Prof. Ervin Fodor (University of Oxford, UK)	N/A
pHW2000-PA-WSN	Prof. Ervin Fodor (University of Oxford, UK)	N/A
pHW2000-NP-WSN	Prof. Ervin Fodor (University of Oxford, UK)	N/A
pHW2000-NA-WSN	Prof. Ervin Fodor (University of Oxford, UK)	N/A
pHW2000-M-WSN	Prof. Ervin Fodor (University of Oxford, UK)	N/A
pHW2000-NS-WSN	Prof. Ervin Fodor (University of Oxford, UK)	N/A
pHW2000-HA-WSN	Prof. Ervin Fodor (University of Oxford, UK)	N/A
pHW2000-PA-WSN-mScarlet	Andrew Mehle (University of Wisconsin – Madison, USA)	N/A
pcDNA3.4-mScarlet-codon-optimized	This publication	N/A
pHW2000-PA-WSN-mScarlet-codon-optimized	This publication	N/A
pC1-Rab7-eGFP	Dr. Pierre-Yves Lozach (CIID, University of Heidelberg, Germany)	N/A
pN1-LAMP1-eGFP	Dr. Pierre-Yves Lozach (CIID, University of Heidelberg, Germany)	N/A

Software and algorithms

GenSmart™ Codon Optimization, Version Beta 1.0	GenScripts	https://www.genscript.com/gensmart-free-gene-codon-optimization.html
FIJI	Schindelin et al. ⁷⁹	https://imagej.net/software/fiji/
IMOD	Kremer et al. ⁸⁵	https://bio3d.colorado.edu/imod/download.html
Icy	De Chaumont et al. ¹³¹	https://icy.bioimageanalysis.org/download/
Dynamo	Castaño-Díez et al. ¹²⁸	https://wiki.dynamo.biozentrum.unibas.ch/w/index.php/Downloads
LAS X	Leica Microsystems	https://www.leica-microsystems.com/de/produkte/mikroskop-software/p/leica-las-x-ls/
MAPS	Schorb and Sieckmann ¹²¹	https://www.thermofisher.com/de/de/home/electron-microscopy/products/software-em-3d-vis/maps-software.html
Prism	GraphPad Software	https://www.graphpad.com/scientific-software/prism/
Imaris	Oxford Instruments	https://imaris.oxinst.com
Post-correlation cryo-CLEM toolbox	Klein et al. ⁴²	https://github.com/Chlanda-Lab/cryoCLEM
Cryocare	Buchholz et al. ¹²⁷	https://github.com/juglab/cryoCARE_pip
Amira	ThermoFisher Scientific	https://www.thermofisher.com/de/de/home/electron-microscopy/products/software-em-3d-vis/amira-software.html
Motioncor2	Zheng et al. ¹²⁶	https://emcore.ucsf.edu/ucsf-software
MATLAB 2020B	MathWorks	https://www.mathworks.com/products/new_products/release2020b.html
AutoQuant X3	Media Cybernetics, Inc.	https://mediacy.com/image-pro/autoquant-deconvolution/
SerialEM	Mastrorade ⁸⁴	https://bio3d.colorado.edu/SerialEM/download.html

(Continued on next page)

Continued

REAGENT or RESOURCE	SOURCE	IDENTIFIER
Magellan™	Tecan Trading AG	https://lifesciences.tecan.com/software-magellan
Python 3	Van Rossum and Drake ¹³²	https://www.python.org/downloads/
VMD	Humphrey et al. ⁹⁹	https://www.ks.uiuc.edu/Development/Download/download.cgi?PackageName=VMD
GROMACS-2021	Abraham et al. ⁹⁸	https://manual.gromacs.org/2021/download.html

Other

UV irradiation system	Vilber Lourmat GmbH	BIO-SUN
Sonicator	Bandelin Sonorex	N/A
Ultracentrifuge	Beckman Coulter, Inc.	Optima L-90K
Rotor for Optima L-90K	Beckman Coulter, Inc.	SW32
Ultracentrifuge	Beckman Coulter, Inc.	Optima TLX
Rotor for Optima TLX	Beckman Coulter, Inc.	TLA-120.2
Mini-PROTEAN Tetra Vertical Electrophoresis Cell	BioRad	1658005
Trans-Blot® Turbo™ Transfer System	BioRad	1704150
Azure 400 chemiluminescent imager	Azure Biosystems	Azure 400
Plate reader	Tecan Trading AG	Infinite 200
High pressure freezing system	Leica Microsystems	EM ICE
Freeze substitution system	Leica Microsystems	EM AFS2
Sputter coater	Leica Microsystems	EM ACE600
Ultramicrotome	Leica Microsystems	EM UC7
Diamond knife for ultramicrotome, 35° angle	DiATOME	DU3520
14 ml round bottom tube	Greiner Bio-One	187261
0.45 μm CME filter	Carl Roth GmbH + Co. KG	KH55.1
Microscopy cover slip NO. 1	Paul Marienfeld GmbH & Co. KG	0111520
Microscopy slides, 76 × 26 mm	Diagonal GmbH & Co. KG	ISO NORM 8037/1
96 well assay plate, black, clear bottom	Corning Incorporated	3603
Sapphire discs for HPF/FS, Ø 3 × 0.05 mm	Leica Microsystems	16702766
Quantifoil EM grid, 200 mesh gold, R1/4 SiO ₂ film	Plano GmbH, Germany	S211R14A200
EM slot grids 2x1 mm, copper	Gilder	G2010-Cu
Cloning cylinder, glass, 150 μl	Merck, Sigma-Aldrich	C1059-1EA
SP8 with 63×/1.4 NA HC PL APO CS2 oil immersion objective	Leica Microsystems	N/A
CellDiscoverer 7 with 20×/0.95 NA plan-apochromat air objective	Zeiss	N/A
Eclipse Ts2-FL fluorescent microscope equipped with DS-Fi3 camera	Nikon	TS2-FL DS-Fi3
Objective for Nikon Eclipse Ts2: CFI Achrom LWD ADL 20XF (20× / 0.4 NA)	Nikon	MRP46202
Blam-assay filterset for Nikon Eclipse Ts2 (ET Bandpass 395/25, ET dualband beamsplitter DAPI/FITC, ET dualband emitter DAPI/FITC)	Chroma Technology Corporation	ET395/25x 59001bs 59001m
CryoCLEM with 60×/0.9 NA objective	Leica Microsystems	N/A
Cryo-TEM Titan Krios, Gatan K3 camera, GIF	ThermoFisher Scientific	N/A
Cryo-FIB/SEM Aquilos	ThermoFisher Scientific	N/A
TEM Tecnai F30, Gatan OneView 4K camera	FEI	N/A

RESOURCE AVAILABILITY

Lead contact

Further information and requests for resources and reagents should be directed to and will be fulfilled by the lead contact, Petr Chlanda (petr.chlanda@bioquant.uni-heidelberg.de).

Materials availability

All materials are available on request.

Data and code availability

- All plotted values in all main and supplementary figures are provided in [Table S1](#).
- MD simulations parameters and structure files are publicly available at Zenodo. The accession code is listed in the [key resources table](#).
- The MATLAB code for all modeling simulations is publicly available on GitHub. The link is listed in the [key resources table](#).
- Reconstructed tomograms are available at the Electron Microscopy Data Bank (EMDB).⁷² The accession codes are listed in the [key resources table](#).
- Fluorescence microscopy, immunoblot data and line profile measurements are available at the BioStudies database.⁷³ The accession codes are listed in the [key resources table](#).
- Any additional information required to reanalyze the data reported in this work is available from the [lead contact](#) upon request.

EXPERIMENTAL MODEL AND SUBJECT DETAILS

Human embryonic kidney 293 cells expressing SV40 large T antigen (HEK293T)

HEK293T cells were obtained from the American Type Culture Collection (ATCC). Cells were cultured at 37 °C in 5% CO₂ in Dulbecco's modified Eagle medium (DMEM) supplemented with GlutaMAX™-I, 10% fetal bovine serum (FBS), and 1% penicillin/streptomycin (P/S).

HEK293T-Master Cell Bank cells (HEK293T-MCB)

HEK293T-MCB cells were kindly provided by Dr. Marco Binder (DKFZ, Heidelberg, Germany). Cells were cultured at 37 °C in 5% CO₂ in DMEM supplemented with GlutaMAX™-I, 10% FBS, and 1% P/S.

Madin-Darby canine kidney cells (MDCK)

MDCK cells were kindly provided by Prof. João Amorim (Instituto Gulbenkian de Ciência, Portugal). Cells were cultured at 37 °C in 5% CO₂ in DMEM-F12 supplemented with 10% FBS and 1% P/S.

A549 cells

A549 is a cell line derived from carcinomatous lung tissue from a Caucasian male at age 58⁷⁴ and is regularly used as a model cell line for IAV infection studies. Cells were obtained from ATCC and cultured at 37 °C in 5% CO₂ in DMEM-F12 supplemented with 10% FBS and 1% P/S.

A549 cells expressing IFITM3 (A549-IFITM3)

To study the antiviral effect of IFITM3, we established an A549 cell line stably overexpressing IFITM3 using lentiviral transduction, as described in the following section.

Cloning

The IFITM3 gene sequence, including a stop codon, was transferred from a cDNA entry vector (pENTR221-clone3728-IFITM3) to the destination vector pWPI-IRES-Puro. 150 ng of entry and destination vector were added with 1 μl Gateway™ LR Clonase Enzyme Mix (ThermoFisher Scientific, Invitrogen) in a total volume of 5 μl TE buffer (10 mM Tris, 0.1 mM EDTA, pH 8). The reaction was run for 2 hours (h) at 25 °C on a thermocycler.

Transformation

50 μl *E. coli* Stellar™ competent cells (Takara) were combined with 5 μl reaction mix from the cloning step and incubated for 30 min on ice and subsequently heat shocked for 45 sec at 42 °C on a heating block. 450 μl S.O.C. medium (ThermoFisher Scientific, Invitrogen) was added, cells were transferred to a 14 ml round bottom tube and incubated for 1 h at 37 °C on a shaker with 180 rpm. Cells were plated on 1.5% LB agar plates with 50 μg/ml ampicillin and incubated overnight at 37 °C. Individual colonies were picked, added to 50 ml LB media containing 50 μg/ml ampicillin, and incubated for 16 h at 37 °C on a shaker with 180 rpm. Plasmids were purified using the QIAprep Spin Miniprep Kit (QIAGEN), and individual clones were sequenced at Microsynth using the IRES-rev primer (TATAGACAACGCACACCG). The correct insert was validated, and a second 200 ml overnight culture was purified using the Plasmid Maxi Kit (QIAGEN). The new plasmid is named pWPI-IFITM3.

Lentiviral production

All work with infectious lentiviruses was performed under biosafety level 2 (BSL-2) laboratory conditions. Lentivirus was produced using a second-generation packaging system utilizing the envelope plasmid pCMV-VSV-G, the packaging plasmid psPAX2, and the previously cloned transfer plasmid pWPI-IFITM3. For enhanced protein expression, we further used the pAdVantage™ plasmid (Promega). HEK293T-MCB cells were seeded in a 6-well plate with 4×10^5 cells per well in a 2.5 ml cell culture medium (DMEM-GlutaMAX™-I, 10% FBS, 1% P/S) and incubated overnight at 37 °C with 5% CO₂. The transfection mix was prepared as follows for one well: 0.375 μg pCMV-VSV-G plasmid, 0.75 μg psPAX2 plasmid, 1.25 μg pWPI-IFITM3 plasmid, 0.125 μg pAdVantage™ plasmid were added in 250 μl Opti-MEM medium (ThermoFisher Scientific, Gibco). 7.5 μl transfection reagent TransIT-2020 (Mirus Bio) was added and incubated for 30 min at RT. The transfection mix was added to one well of the 6-well plate. 6 h post-transfection, the cell culture medium was replaced with 1.5 ml fresh medium. 48 h post-transfection, lentivirus containing supernatant was harvested and filtered through a 0.45 μm CME filter (Roth). A Lenti-X™ GoStix (Takara) antigen test was used to verify successful lentivirus production.

Transduction

A549 cells were seeded in a 12-well plate with 2×10^4 cells per well in 1 ml cell culture medium (DMEM-F12, 10% FBS, 1% P/S) and incubated overnight at 37 °C with 5% CO₂. 350 μl filtered lentivirus supernatant was supplemented with polybrene infection reagent (Merck, Sigma-Aldrich) in a final concentration of 5 μg/ml. The cell culture medium of A549 cells was removed, and 350 μl lentivirus supernatant was added to the cells. 2 days post-transduction, the antibiotic selection was started with 0.8 μg/ml puromycin. After 2 days of selection, the puromycin concentration was increased to 1.2 μg/ml. The selection was continued for 2 more days until all non-transduced control cells detached from the dish. Selected cells were trypsinized and transferred to a 10 cm cell culture dish and were further grown in a selection medium with 1.5 μg/ml puromycin. Individual cell colonies could be observed after 2 more days. Individual colonies were separated using cloning cylinders (Sigma-Aldrich) and further expanded to establish the monoclonal cell line A549-IFITM3.

Influenza A virus (strain A/WSN/1933)

Reverse genetics

All work with infectious IAV was performed under BSL-2 laboratory conditions. The IAV strain A/WSN/1933 (H1N1) was rescued from a reverse genetics system established by Hoffmann et al.⁷⁵ 4×10^6 HEK293T cells were seeded in a 10 cm cell culture dish and grown overnight in 10 ml complete growth media (DMEM-GlutaMAX™-I, 10% FBS, 1% P/S). The transfection mix was prepared as follows: 2.5 μg of each of the 8 plasmids of the reverse genetics system (pHW2000-PB1-WSN, pHW2000-PB2-WSN, pHW2000-PA-WSN, pHW2000-NP-WSN, pHW2000-NA-WSN, pHW2000-M-WSN, pHW2000-NS-WSN, pHW2000-HA-WSN) were added to a total volume of 2 ml Opti-MEM medium. 60 μl transfection reagent TransIT-293 (Mirus Bio) was added and incubated for 30 min at RT and added to the 10 cm dish with HEK293T cells. After 24 h, the medium was exchanged with FBS-free infection medium (DMEM-GlutaMAX™-I, 1% P/S, 0.3% BSA, 2 μg/ml TPCK-trypsin), and 4×10^6 MDCK cells were seeded in the same cell culture dish to be co-cultured with the transfected HEK293T cells. After 24 h, virus-containing supernatant (P0) was harvested and centrifuged for 10 min with $1,000 \times g$ to remove cell debris. The supernatant was aliquoted, shock frozen in LN₂, and stored at -80 °C until further use.

Virus propagation and purification

6×10^6 MDCK cells were seeded in 30 ml complete growth media (DMEM-GlutaMAX™-I, 10% FBS, 1% P/S) in T175 cell culture flasks and grown overnight. The virus-containing supernatant (P0), recovered from the reverse genetics system, was diluted 1:10 in FBS-free infection media (DMEM-GlutaMAX™-I, 1% P/S, 0.3% BSA, 2 μg/ml TPCK-trypsin). MDCK cells were washed 3 times with PBS. 10 ml of the diluted virus supernatant was added to the cells and incubated for 1 h at 37 °C with 5% CO₂. Cells were washed 1 time with PBS, and 40 ml FBS-free infection medium was added. Cells were grown for 3 days until a cytopathic effect was observed. The virus-containing supernatant (P1) was centrifuged 2 times for 15 min at $2,200 \times g$ to remove cell debris. Cleared supernatant was subsequently sucrose purified: 33 ml of virus-containing supernatant was overlaid on 5 ml of 30% sucrose in HEN buffer (10 mM HEPES, 1 mM EDTA, 100 mM NaCl, pH 7.4) in a thin-walled centrifugation tube and centrifuged for 90 min at $83,018 \times g$, 4 °C using the swing-out rotor SW32 on an Optima L-90K (Beckman Coulter) ultracentrifuge. The supernatant was discarded, and the pellet was resuspended in 1 ml HEN buffer. The sample was centrifuged again for 30 min at $15,728 \times g$, 4 °C using the fixed-angle rotor TLA-120.2 on an Optima TLX (Beckman Coulter) ultracentrifuge. The supernatant was discarded, and the pellet was dissolved in 200 μl HEN buffer. The purified virus was aliquoted, shock frozen in LN₂, and stored at -80 °C until further use.

Plaque assay

1×10^6 MDCK cells per well were seeded in a 6-well plate in 2 ml complete growth medium (DMEM-F12, 10% FBS, 1% P/S) and grown overnight. Dilution series of purified virus stock was prepared in an FBS-free infection medium (DMEM-GlutaMAX™-I, 1% P/S, 0.3% BSA, 2 μg/ml TPCK-trypsin) from 10^{-3} to 10^{-9} . Cells were washed 3 times with PBS, and 800 μl of each virus dilution was added per well. Cells were incubated for 1 h at 37 °C and 5% CO₂, virus dilution was removed, cells were washed 2 times with infection medium and overlaid with 3 ml plaque medium containing Avicel (DMEM-GlutaMAX™-I, 0.5% P/S, 0.15% BSA, 1 μg/ml TPCK-trypsin, 1.2 % Avicel RC-581) per well. After 2 days, the plaque medium was aspirated, and cells were washed 2 times with PBS and fixed with 1% glutaraldehyde (GA) in PBS for 30 min at RT. Cells were washed with PBS and stained with 1% crystal violet solution (Sigma-Aldrich) for 10 min at RT. Cells were thoroughly washed with water, and plaques were counted. For each dilution, virus titer, T_{virus} , was determined by $T_{virus} = \frac{n_{plaque}}{d \cdot V}$, with the number of plaques, n_{plaque} , the dilution factor, d , and the volume of virus dilution, V . The average titer of all wells containing plaques was determined and used as final virus titer.

Fluorescently labeled influenza A virus (A/WSN/1933-nDiO)

For *in situ* cryo-CLEM, we fluorescently labeled A/WSN/1933 IAV using the fluorescent and lipophilic membrane dye neuro-DiO (nDiO). The virus was recovered from a reverse genetics system and purified as described above. 5 μ l of ready to use nDiO solution 'Cellbrite™ Green' (Biotium) was added to 200 μ l purified virus and incubated for 1 h on a rotation wheel at RT. The virus was subsequently purified again by sucrose purification: 200 μ l purified and fluorescently labeled virus was overlaid on 500 μ l of 10% sucrose in HEN buffer in a thick-walled centrifugation tube and centrifuged for 90 min at 107,000 \times g, 4 °C using the swing-out rotor TLS-55 on an Optima Max (Beckman Coulter) ultracentrifuge. The supernatant was discarded, and the pellet was resuspended in 1 ml HEN buffer. The sample was centrifuged again for 30 min at 15,728 \times g, 4 °C using the fixed-angle rotor TLA-120.2 on an Optima TLX (Beckman Coulter) ultracentrifuge. The supernatant was discarded, and the pellet was dissolved in 200 μ l HEN buffer. The fluorescently labeled virus was aliquoted, shock frozen in LN₂, and stored at -80 °C until further use. Viral titer was determined again using the plaque assay as described above.

Fluorescent influenza a reporter virus (A/WSN/1933-PA-mScarlet)

For the infection assay, we established a reporter virus A/WSN/1933 expressing a fluorescently tagged polymerase acidic protein (PA) based on Tran et al.⁷⁶ For increased integration stability of the fluorescent tag in the viral genome, we performed codon optimization of the gene sequence coding for the fluorescent protein mScarlet by substitution of CpG and TpA sites, which are known to be recognized by the Zinc finger antiviral protein restriction factor.⁷⁷

mScarlet codon optimization

The gene sequence coding for mScarlet⁷⁸ was codon-optimized for mammalian gene expression using the GenSmart™ codon optimization algorithm (version 1.0, GenScripts). Subsequently, all CpG and TpA sites in the codon-optimized sequence were manually exchanged without modifying the aminoacidic sequence. This optimized sequence was synthesized and inserted in a pcDNA3.4 plasmid by the GeneArt gene synthesis service (ThermoFisher Scientific). The newly synthesized plasmid is named pcDNA3.4-mScarlet-codon-optimized.

Cloning

Using In-Fusion cloning (Takara), we exchanged the mScarlet of the reverse genetics' plasmid pHW2000-PA-mScarlet (kindly provided by Prof. Dr. Andrew Mehle) with the codon-optimized mScarlet, generated as described above. Overhang PCR was prepared as follows: 1 ng pcDNA3.4-mScarlet-codon-optimized plasmid, 0.2 μ M forward overhang primer (CCCACGCCCTGCGCGGGCAG CAATGGTGTCCAAGGGTGAAGC), 0.2 μ M reverse overhang primer (AAGCAGTTTTCTAGATCACTTGTACGCTCATCCATTCCAC), 12.5 μ l CloneAmp™ HiFi PCR Premix (Takara) and 1 μ l DMSO were mixed in a total volume of 25 μ l H₂O. PCR reaction was run for 35 cycles with denaturation at 98 °C for 10 sec, annealing at 64 °C for 15 sec, and elongation at 72 °C for 10 sec. 8 μ l Cloning Enhancer (Takara) was added to 20 μ l of the PCR product and incubated for 15 min at 37 °C on a thermocycler, followed by an inactivation step at 80 °C for 15 min. The pHW2000-PA-mScarlet plasmid was linearized by restriction digestion: 1 μ g pHW2000-PA-mScarlet plasmid, 1 u XbaI (New England Biolabs), 1.33 u BssHII (New England Biolabs) were added in a total of 50 μ l 1 \times CutSmart buffer (New England Biolabs). The reaction was run for 15 min at 37 °C on a thermocycler, followed by an inactivation step at 65 °C for 20 min. Restriction digestion products were separated on a 0.7% agarose gel, and linearized plasmid was purified from the gel using the NucleoSpin Gel and PCR Clean-up kit (Macherey-Nagel). In-Fusion reaction was prepared as follows: 25 ng PCR fragment with overhang, 50 ng linearized and purified vector, 1 μ l 5 \times In-Fusion Enzyme Mix (Takara) were mixed in a total of 5 μ l H₂O. The reaction was run for 15 min at 50 °C on a thermocycler.

Transformation

50 μ l *E. coli* Stellar™ competent cells (Takara) were combined with 5 μ l In-Fusion reaction product and incubated for 30 min on ice and subsequently heat shocked for 45 sec at 42 °C on a heating block. 450 μ l S.O.C. medium (ThermoFisher Scientific, Invitrogen) was added, cells were transferred to a 14 ml round bottom tube and incubated for 1 h at 37 °C on a shaker with 180 rpm. Cells were plated on 1.5% LB agar plates with 50 μ g/ml ampicillin and incubated overnight at 37 °C. Individual colonies were picked, added to 50 ml LB media containing 50 μ g/ml ampicillin, and incubated for 16 h at 37 °C on a shaker with 180 rpm. Plasmids were purified using the QIAprep Spin Miniprep Kit (QIAGEN), and individual clones were sequenced at Microsynth using a forward primer (GGCAA ACAACAGATGGCTGGCAAC) and reverse primer (GTATGCATCTCCACA ACTAGAAGG). The correct sequence was validated, and a second 200 ml overnight culture was purified using the Plasmid Maxi Kit (QIAGEN). The new plasmid is named pHW2000-PA-WSN-mScarlet-codon-optimized.

Reverse genetics

A fluorescent reporter virus was recovered and purified as described above for the A/WSN/1933 virus using the reverse genetics system established by Hoffmann et al.,⁷⁵ but here the plasmid pHW2000-PA-WSN was exchanged with pHW2000-PA-WSN-mScarlet-codon-optimized.

METHODS DETAILS

Immunoblot analysis

The expression levels of IFITM3 in A549 cells, with and without IFN β -1b treatment, and of the established stable cell line A549-IFITM3 (as described above) were analyzed by immunoblot analysis as described below.

Protein extraction

1×10^6 A549 or A549-IFITM3 cells were seeded in 10 cm cell culture dishes in complete growth medium (DMEM-F12, 10% FBS, 1% P/S). A549 cells were treated with different concentrations of IFN β -1b (0, 100, 500, 1,000, 2,000 units/ml). After 48 h, cells were washed 2 times with ice-cold PBS and lysed with 650 μ l RIPA buffer (50 mM Tris-HCL, 150 mM NaCl, 1% v/v Triton X-100, 0.5% v/v sodium deoxycholate, 0.1% v/v SDS, 1 \times protease inhibitor cocktail (ThermoFisher Scientific, Roche) in H₂O) on ice for 20 min. The cell lysate was centrifuged with 12,000 \times g for 20 min at 4 $^{\circ}$ C to remove cell debris. The protein concentration of the supernatant was quantified using the Pierce™ BCA Protein Assay Kit (ThermoFisher Scientific).

Gel electrophoresis

All samples were diluted in RIPA buffer to a final protein concentration of 0.7 μ g/ μ l. 66.7 μ l 4 \times Laemmli sample buffer (Bio-Rad), supplemented with 0.2 M dithiothreitol, was added to 200 μ l of diluted sample and incubated for 8 min at 90 $^{\circ}$ C on a heating block. 40 μ l of each sample was loaded to a 4 – 15% precast polyacrylamide gel (Bio-Rad). As a size marker, 10 μ l of a broad range color pre-stained protein standard (New England BioLabs) was added to the outer lanes. Samples were separated by gel electrophoresis in 1 \times TGS running buffer (Bio-Rad) for 60 min with 120 V using a Mini-PROTEAN electrophoresis chamber (Bio-Rad).

Western blotting

Separated proteins were transferred from the polyacrylamide gel to a 0.2 μ m PVDF membrane (Bio-Rad) for 7 min with a constant 2.5 A using a Trans-Blot Turbo transfer system (Bio-Rad).

Immunolabeling

PVDF membrane was cut at 26 kDa to analyze the expression of IFITM3 and actin on the same membrane. Membranes were washed 3 times for 5 min in TBS supplemented with 0.1% v/v Tween-20 (TBS-T) and subsequently blocked in 5% BSA in TBS-T for 1 h at RT on a rocker. The lower part of the membrane (0 – 26 kDa) was incubated in primary antibody against IFITM3 (Proteintech) with a dilution of 1:2,000 in TBS-T for 1 h at RT on a rocker. The upper part of the membrane (26 – 250 kDa) was incubated in primary antibody against actin (Sigma-Aldrich) with a dilution of 1:4,000 in TBS-T for 1 h at RT on a rocker. Membranes were washed 3 times for 5 min in TBS-T and incubated with the secondary antibodies: anti-rabbit-HRP (Santa-Cruz) with a dilution of 1:1,000 in TBS-T for the lower part of the membrane (0 – 26 kDa), immunolabelled against IFITM3 or anti-mouse-HRP (Santa-Cruz) with a dilution of 1:1,000 in TBS-T for the upper part of the membrane (26 – 250 kDa), immunolabelled against actin, respectively. Membranes were washed 3 times for 5 min with TBS and were subsequently incubated with Clarity Western ECL substrate working solution (Bio-Rad) for 5 min. Chemiluminescent signal was acquired using the Azure 400 imaging system (Azure Biosystems).

Quantification of protein expression

Individual bands of IFITM3 and actin of each sample were quantified using the Gel Analyzer plugin of FIJI.⁷⁹ IFITM3 signal was normalized to the corresponding actin, and relative IFITM3 expression levels were calculated.

Confocal fluorescent light microscopy

Confocal fluorescent light microscopy analysis was performed to study the impact of IFN β -1b treatment or IFITM3 overexpression on the number and volume of IFITM3 positive organelles in A549 cells.

Immunofluorescence

5×10^4 A549 or A549-IFITM3 cells were seeded on 12 mm microscopy coverslips NO. 1 (Marienfeld) in a 6-well plate in complete growth medium (DMEM-F12, 10% FBS, 1% P/S). The next day, A549 cells were treated with 1×10^3 units/ml IFN β -1b (Immuno Tools). After 24 h IFN β -1b treatment, cells were fixed with 4% PFA in PBS for 15 min and washed 3 times with PBS. PFA was quenched by incubating the cells with 20 mM glycine in PBS for 10 min, followed by 3 washing steps with PBS for 5 min each. Cells were permeabilized by incubation with 0.2% Triton X-100 in PBS for 5 min, followed by 3 washing steps with PBS for 5 min each. Cells were incubated for 1 h with blocking buffer (3% BSA in PBS supplemented with 0.1% Tween-20 (PBS-T)). After 3 short washing steps with PBS-T, cells were incubated for 1 h with primary antibody against IFITM3 (Proteintech) using an antibody dilution of 1:200 in dilution buffer (1% BSA in PBS-T) at RT on a rocker. After 3 washing steps with PBS-T for 5 min each, cells were incubated with the secondary antibody 'goat anti-Rabbit Alexa Fluor™ 633' (ThermoFisher Scientific, Invitrogen) in a dilution of 1:2,000 in dilution buffer for 1 h at RT on a rocker. After 3 washing steps with PBS-T for 5 min each, nuclei were fluorescently labeled by incubation with 1 μ g/ μ l Hoechst 33342 (Sigma-Aldrich) in PBS for 5 min. Cells were washed 3 times with PBS for 5 min each, followed by a short washing step with deionized water. Coverslips were mounted on microscopy slides using 7 μ l ProLong Glass Antifade mounting medium (ThermoFisher Scientific, Invitrogen). The mounting medium was cured for 24 h at RT.

Confocal microscopy

Confocal microscopy data was acquired using the SP8 TCS laser scanning confocal microscope (Leica) equipped with a 63 \times /1.4 HC PL APO CS2 oil immersion objective using a UV laser with an excitation wavelength of 405 nm (for Hoechst 33342) and a helium-neon laser with an excitation wavelength of 633 nm (for Alexa Fluor™ 633) in sequential acquisition mode with 4 \times line accumulation. A pixel size of 60.13 nm was used, and Z-stacks were acquired using a Z-spacing of 200 nm.

Deconvolution

Image stacks were deconvolved with AutoQuant X3 (Media Cybernetics) using a theoretical and adaptive point spread function (PSF) for 10 iterations with the following parameters: lens immersion refractive index 1.515; sample embedding refractive index 1.52; sample distance from coverslip of 0 nm; emission wavelength of 461 nm (for Hoechst 33342) or 647 nm (for Alexa Fluor™ 633) and appropriate settings for the used objective (NA 1.4; objective lens magnification 63 \times).

Segmentation and quantification

The IFITM3 signal of the deconvolved image stacks was segmented in 3 dimensions using the surface segmentation algorithm of Imaris (Verison 9.8.2, Oxford Instruments). The number of segmented objects per cell and the volume distribution of all objects were quantified.

Colocalization analysis

To evaluate the colocalization between IFITM3 and Rab7 or LAMP1 in the A549-IFITM3 cell line, we performed immunofluorescence, confocal microscopy and colocalization analysis as described below.

Transfection

1×10^5 A549-IFITM3 cells were seeded on 12 mm microscopy coverslips NO. 1 (Marienfeld) in a 6-well plate in complete growth medium (DMEM-F12, 10% FBS, 1% P/S). The next day, cells were transfected with either pC1-Rab7-eGFP or pN1-LAMP1-eGFP. A transfection mix was prepared by adding 2.5 μ g plasmid and 7.5 μ l transfection reagent TransIT-LT1 (Mirus) in 250 μ l OptiMEM medium. Transfection mix was added to the cells (250 μ l per well), and incubated for 30 min at RT. Cells were incubated at 37°C, 5% CO₂ for 24 h.

Immunofluorescence

Cells were fixed with 4% PFA in PBS for 30 min and washed 3 times with PBS. Cells were permeabilized by incubation with 0.2% Triton X-100 in PBS for 5 min, followed by 3 washing steps with PBS for 5 min each. Cells were incubated for 1 h with blocking buffer (3% BSA in PBS supplemented with 0.1% Tween-20 (PBS-T)). After 3 short washing steps with PBS-T, cells were incubated for 1 h with primary antibody against IFITM3 (Proteintech) using an antibody dilution of 1:200 in dilution buffer (1% BSA in PBS-T) at RT on a rocker. After 3 washing steps with PBS-T for 5 min each, cells were incubated with the secondary antibody 'goat anti-Rabbit Alexa Fluor™ 633' (ThermoFisher Scientific, Invitrogen) in a dilution of 1:2,000 in dilution buffer for 1 h at RT on a rocker. After 3 washing steps with PBS-T for 5 min each, nuclei were fluorescently labeled by incubation with 1 μ g/ μ l DAPI in PBS for 1 min. Cells were washed 3 times with PBS for 5 min each, followed by a short washing step with deionized water. Coverslips were mounted on microscopy slides using 7 μ l ProLong Glass Antifade mounting medium (ThermoFisher Scientific, Invitrogen). The mounting medium was cured for 24 h at RT.

Confocal microscopy

Confocal microscopy data was acquired using the SP8 TCS laser scanning confocal microscope (Leica) equipped with a 63 \times /1.4 HC PL APO CS2 oil immersion objective using a UV laser with an excitation wavelength of 405 nm (for DAPI), an argon laser with an excitation wavelength of 488 nm (for eGFP) and a helium-neon laser with an excitation wavelength of 633 nm (for Alexa Fluor™ 633) in sequential acquisition mode with 4 \times line accumulation. A pixel size of 72.1 nm was used, and Z-stacks were acquired using a Z-spacing of 200 nm.

Deconvolution

Image stacks were deconvolved with AutoQuant X3 (Media Cybernetics) using a theoretical and adaptive point spread function (PSF) for 10 iterations with the following parameters: lens immersion refractive index 1.515; sample embedding refractive index 1.52; sample distance from coverslip of 0 nm; emission wavelength of 461 nm (for DAPI), 507 nm (for eGFP) or 647 nm (for Alexa Fluor™ 633) and appropriate settings for the used objective (NA 1.4; objective lens magnification 63 \times).

Colocalization analysis

Colocalization analysis between IFITM3 and Rab7, LAMP1 or DAPI was performed by calculating the Pearson's and Manders' correlation coefficients⁸⁰ using the 'coloc2' tool in ImageJ/FIJI⁷⁹ using a manually selected region of interest for each analyzed cell. Before correlation analysis, the background signal was subtracted using a rolling ball algorithm (radius = 30 px)⁸¹ implemented in ImageJ/FIJI.⁷⁹

Infection assay using wide-field fluorescent light microscopy

To analyze the antiviral effect of stable overexpression of IFITM3 in A549 cells, we performed an infection assay using the here established reporter virus A/WSN/1933-PA-mScarlet (see section above) as described below:

Viral infection

5×10^4 A549 or A549-IFITM3 cells were seeded on 12 mm microscopy coverslips NO. 1 (Marienfeld) in a 24-well plate in complete growth medium (DMEM-F12, 10% FBS, 1% P/S). The next day, the cells were infected with a fluorescent report virus A/WSN/1933-PA-mScarlet using an MOI of 3 in serum free DMEM-F12 medium for 1 h at 37°C, 5% CO₂. Cells were washed 3 times with a complete growth medium and incubated at 37°C, 5% CO₂. Cells were fixed at 24 hpi with 4% PFA in PBS for 30 min at RT. After fixation, cells were washed 3 times with PBS.

Immunolabeling

Cells were permeabilized by incubation with 0.2% Triton X-100 in PBS for 5 min, followed by 3 washing steps with PBS for 5 min each. Cells were incubated for 1 h with a blocking buffer (3% BSA in PBS supplemented with 0.1% PBS-T). After 3 short washing steps with PBS-T, cells were incubated for 1 h with primary antibody against M2 (Proteintech) using an antibody dilution of 1:50 in dilution buffer (1% BSA in PBS-T) at RT on a rocker. After 3 washing steps with PBS-T for 5 min each, cells were incubated with DAPI using a 1:1000 dilution (Sigma-Aldrich) and the secondary antibody 'goat anti-Mouse Alexa Fluor™ 633' (ThermoFisher Scientific, Invitrogen) in a dilution of 1,000 in dilution buffer for 1 h at RT on a rocker. Cells were washed 3 times with PBS for 5 min each, followed by a short

washing step with deionized water. Coverslips were mounted on microscopy slides using 7 μ l ProLong Glass Antifade mounting medium (ThermoFisher Scientific, Invitrogen). The mounting medium was cured for 24 h at RT.

Automated high-throughput fluorescent imaging

Wide field microscopy data was acquired using the Celldiscoverer 7 automated microscope (Zeiss) equipped with a 20 \times /0.95 NA PL APO COR objective and Axiocam 712 camera.

Quantification

Stitched composite images were binned 6 times in ImageJ/FIJI and nuclei were segmented using the StarDist plugin in ImageJ/FIJI.⁸² The average signal intensity in the segmented area of each individual nucleus was calculated for M1 and PA-mScarlet. Maximum average signal intensity for M2 and PA-mScarlet of non-infected control cells was determined and set as a threshold to determine infected cells. Each nucleus with an average signal intensity for M2 \leq 1,150 a.u. or PA \leq 1,450 a.u. was counted as infected.

Beta-lactamase (Blam) membrane fusion assay

To analyze the impact of IFN β -1b treatment or IFITM3 overexpression in A549 cells on viral membrane fusion in late endosomes, we utilize a β -lactamase (Blam) based membrane fusion assay using influenza A virus-like particles (VLPs) expressing M1 with covalently bound Blam. Cells were laden with a fluorescence resonance energy transfer (FRET) substrate CCF4-AM (ThermoFisher Scientific, InvitrogenTM), which can be proteolytically cleaved by Blam, resulting in an emission shift from 530 nm to 460 nm,⁸³ enabling the detection of cytoplasmic entry of M1-Blam VLPs.

M1-Blam VLP production

2.7×10^6 HEK293T cells were seeded in 10 ml complete growth medium (DMEM-GlutaMAXTM-I, 10% FBS, 1% P/S) in a 10 cm cell culture dish. Cells were grown overnight at 37 $^{\circ}$ C and 5% CO₂. A transfection mix was prepared as follows: 1.48 μ g pCAGGS-A/Hong Kong/1968-HA plasmid, 1.40 μ g pCAGGS-A/Singapore/1957-NA, 7.12 μ g pCAGGS-M1-Blam plasmid were added to a total volume of 1 ml Opti-MEM medium. 30 μ l transfection reagent PEI (1 μ g/ μ l, Polysciences) was added and incubated for 30 min at RT and added to the 10 cm dish with HEK293T cells. 6 h post transfection, cells were washed with PBS, and 10 ml OptiMEM medium supplemented with 1% P/S was added. After 48 h incubation at 37 $^{\circ}$ C and 5% CO₂, VLP-containing supernatant was harvested and centrifuged at 1,000 \times g for 10 min to remove cell debris. 2.5 μ l TPCK-Trypsin (10 μ g/ μ l, Sigma-Aldrich) was added to the supernatant and incubated for 30 min at 37 $^{\circ}$ C to proteolytically cleave HA. TPCK-Trypsin was subsequently deactivated by adding 7 μ l trypsin inhibitor (5 μ g/ μ l in PBS, Sigma-Aldrich) and incubated for 10 min at 37 $^{\circ}$ C. VLP-containing supernatant was aliquoted, shock frozen in LN₂, and stored at -80 $^{\circ}$ C until further use.

Blam membrane fusion assay

For better cell attachment, a black-walled clear-bottom 96-well plate (Corning) was coated with fibronectin: 25 μ l fibronectin solution (57.2 μ g/ml fibronectin in PBS) was added to each well and incubated for 6 h at RT. The remaining solution was removed, and wells were washed 1 time with PBS. In each well, 1.2×10^4 A549 or A549-IFITM3 cells were seeded in 100 μ l complete growth medium (DMEM-F12, 10% FBS, 1% P/S). The next day, A549 cells were treated with different concentrations of IFN β -1b (0, 100, 500, 1,000, 2,000 units/ml). After 48 h, cells were infected with 190 μ l M1-Blam IAV-VLPs. Infection efficiency was enhanced by spinoculation with 250 \times g for 1 h at RT. Cells were washed with PBS, and 90 μ l Opti-MEM supplemented with 1% P/S and 20 mM HEPES was added to each well. Cells were incubated for 3 h at 37 $^{\circ}$ C and 5% CO₂. 20 μ l of 6 μ M CCF4-AM (ThermoFisher Scientific) in Blam loading solutions (ThermoFisher Scientific) was added to each well, and cells were incubated overnight at 8 $^{\circ}$ C on a cooling block.

Quantification with plate reader

Fluorescent signal was measured using the Infinite 200 plate reader (Tecan) with an excitation wavelength of 410 nm (9 nm bandwidth) and emission wavelengths of 450 nm or 520 nm (20 nm bandwidth) using a manual gain of 160 and 3 \times 3 reads per well with an integration time of 20 μ s and 50 reads per position. The background emission signal of the surrounding medium only was subtracted from each measurement, and the ratio between the 450 nm and 520 nm emission signal was calculated. 450 nm / 520 nm ratios of replicates for each sample were averaged. Averaged ratios were normalized to the ratio of A549 cells and reported as relative membrane fusion inhibition between 0 and 1.

Fluorescent microscopy

After plate reader acquisition, representative images of each well were acquired using the Nikon Eclipse Ts2 fluorescent microscope equipped with a DS-Fi3 camera, 20 \times / 0.4 NA lens, and a custom filter cube optimized for Blam assay image acquisition.

Viral entry assay by NH₄Cl add-in time course

To evaluate the time for influenza A virus entry through the endosomal pathway, we performed a viral infection assay with NH₄Cl treatment at different time points post-infection. As NH₄Cl neutralizes the endosomal system, and thus inhibits viral membrane fusion, the half-time of viral entry can be determined as described below.

Viral infection with NH₄Cl add-in time course

5×10^4 A549 or A549-IFITM3 cells were seeded on 12 mm microscopy coverslips NO. 1 (Marienfeld) in a 24-well plate in complete growth medium (DMEM-F12, 10% FBS, 1% P/S). The next day, the cells were infected with a fluorescent reporter virus A/WSN/1933-PA-mScarlet using an MOI of 3 in serum free DMEM-F12 medium for 1 h on ice, to ensure a synchronized infection. Cells were washed 3 times with cold PBS, and cells were incubated at 37 $^{\circ}$ C, 5% CO₂. Cells were treated with 50 mM NH₄Cl at 0 mpi, 15 mpi, 30 mpi, 60 mpi, and 120 mpi. Cells were fixed at 12 – 14 hpi with 4% PFA in PBS for 30 min at RT. After fixation, cells were washed 3 times with PBS.

Immunolabeling

Cells were permeabilized by incubation with 0.2% Triton X-100 in PBS for 5 min, followed by 3 washing steps with PBS for 5 min each. Cells were incubated for 1 h with a blocking buffer (3% BSA in PBS supplemented with 0.1% Tween-20 (PBS-T)). After 3 short washing steps with PBS-T, cells were incubated for 1 h with primary antibody against M2 (Proteintech) using an antibody dilution of 1:50 in a dilution buffer (1% BSA in PBS-T) at RT. After 3 washing steps with PBS-T for 5 min each, cells were incubated with DAPI using a 1:1,000 dilution (Sigma-Aldrich) and the secondary antibody 'goat anti-Mouse Alexa Fluor™ 488' (ThermoFisher Scientific, Invitrogen) in a dilution of 1:1,000 in the dilution buffer for 1 h at RT on a rocker. Cells were washed 3 times with PBS for 5 min each.

Automated high-throughput fluorescent imaging

Widefield microscopy data was acquired using the Celldiscoverer 7 automated microscope (Zeiss) equipped with a 5×/0.35 NA PL APO objective and Axiocam 712 camera.

Quantification

Stitched composite images were binned 2 times in ImageJ/FIJI, and nuclei were segmented using the StarDist plugin in ImageJ/FIJI.⁸² The average signal intensity in the segmented area of each individual nucleus was calculated for M2 and PA-mScarlet. Maximum average signal intensity for M2 and PA-mScarlet of non-infected control cells was determined and set as a threshold to determine infected cells. Each nucleus with an average signal intensity for M2 ≤ 750 a.u. or PA-mScarlet ≤ 600 a.u. was counted as infected.

Determination of viral entry half-time

The calculated infection rates of three independent experiments were plotted against the NH₄Cl add-in times and a four parameter logistic (4PL) curve was fitted. The inflection point (IC50) was determined and reported as viral penetration at half-time $t_{1/2}$.

Transmission electron tomography (ET)

To analyze the late endosomal morphology and quantify the number of ILVs, we performed ET on high-pressure frozen and freeze-substituted (HPF/FS) cells embedded in HM20 Lowicryl. To assess the localization of IFITM3, on-section immunolabelling with anti-IFITM3 and 10 nm Protein A Gold was performed.

High-pressure freezing (HPF)

2.8×10^5 A549 or A549-IFITM3 cells were seeded on carbon-coated 3 mm sapphire discs (Leica) in a 6-well plate in complete growth medium (DMEM-F12, 10% FBS, 1% P/S). A549 cells were treated with 2×10^3 units/ml IFN β -1b (Immuno Tools). After 24 h IFN β -1b treatment, cells were fixed by HPF: Carrier type A and B (Leica) were coated with 1-hexadecene. Excess 1-hexadecene was removed by blotting with a filter paper (Whatman, No. 1). The 100 μ m deep inner groove of carrier A was filled with a complete growth medium. The sapphire disc with cells was blotted on filter paper (Whatman, No. 1) and placed with the cells facing down on carrier A. Carrier B was placed with the flat site on top to close the sandwich. The sample was subsequently high-pressure frozen using an EM ICE HFP system (Leica).

Automated freeze substitution (AFS) and resin embedding

Lowicryl solution was prepared by adding 34.04 g monomer E, 5.96 g crosslinker D, and 200 mg initiator C (Lowicryl HM20 resin kit, Polysciences Inc.). Freeze-substitution solution was prepared by dissolving 0.1 % uranyl acetate (UA) in acetone. All solutions and high-pressure frozen sapphire discs were loaded to the automated freeze substitution system AFS2 (Leica). A freeze substitution program was performed according to the following table:

Automated freeze substitution program:

Step	T start	T end	Slope	Time	Reagent	Transfer	Agitation	UV
1	-90°C	-90°C		48 h	0.1% UA	stay	off	off
2	-90°C	-45°C	5 °C/h	9 h	0.1% UA	stay	off	off
3	-45°C	-45°C		5 h	0.1% UA	stay	off	off
4	-45°C	-45°C		10 min	Acetone	exch/fill	off	off
5	-45°C	-45°C		10 min	Acetone	exch/fill	off	off
6	-45°C	-45°C		10 min	Acetone	exch/fill	off	off
7	-45°C	-45°C		4 h	10% Lowicryl	mix	on	off
8	-45°C	-45°C		4 h	25% Lowicryl	mix	on	off
9	-45°C	-35°C	2.5 °C/h	4 h	50% Lowicryl	mix	on	off
10	-35°C	-35°C	2.5 °C/h	4 h	75% Lowicryl	mix	on	off
11	-35°C	-35°C		10 h	100% Lowicryl	exch/fill	off	off
12	-35°C	-35°C		10 h	100% Lowicryl	exch/fill	off	off
13	-35°C	-35°C		10 h	100% Lowicryl	exch/fill	off	off
14	-35°C	-35°C		48 h	100% Lowicryl	stay	off	on

(Continued on next page)

Continued

Step	T start	T end	Slope	Time	Reagent	Transfer	Agitation	UV
15	-35°C	20°C	5	9 h	100% Lowicryl	stay	off	on
16	20°C	20°C		48 h	100% Lowicryl	stay	off	on
17	20°C	20°C		72 h	100% Lowicryl	stay	off	off

Ultramicrotomy

Lowicryl embedded samples were trimmed and cut with a diamond knife (DiATOME) using a UC7 ultramicrotome (Leica) to obtain sections with 250 nm nominal thickness. Sections were placed on 2 × 1 mm copper slot grids (Gilder) with 1% formvar film, sputter-coated with 2 nm carbon using ACE600 sputter coater (Leica).

Immunolabeling

Sections were blocked for 30 min in blocking solution (PBS supplemented with 0.8% BSA and 0.1% FSG) and incubated for 1 h with the primary antibody against IFITM3 (Proteintech), using an antibody dilution of 1:5 in blocking buffer. Sections were washed 5 times for 5 min each with PBS. Samples were incubated for 1 h with 10 nm Protein-A Gold (PAG) (Aurion) diluted 1:50 in a blocking buffer. Sections were washed 5 times for 5 min each with PBS and subsequently 5 times for 2 min in H₂O.

Tilt series acquisition

Tilt series were acquired on a 300 keV transmission electron microscope (TEM) Tecnai F30 (FEI), equipped with a Gatan OneView 4K camera, from +60° to -60° tilt with 1° steps using a pixel spacing of 1.03 nm using the SerialEM software.⁸⁴

Segmentation and quantification

Tomograms were reconstructed in a batch with patch tracking and R-weighted back projection using the IMOD software package.⁸⁵ To remove bias in data analysis, a de-identified dataset was created. All late endosomes in the reconstructed tomograms were segmented in three dimensions using the IMOD software package.⁸⁵ The endosome was manually segmented every 10 computational slices using the sculpt drawing tool. Segmented sections were interpolated to generate a volume. Volume segmentation was meshed and the total volume inside the mesh was calculated. The number of ILVs was manually counted for each late endosome. The ILV density was calculated for each late endosome by dividing the number of ILVs by the volume of the late endosome.

Cholesterol-analog cross-linking and immunoprecipitation

A549-IFITM3 cells were seeded in 10 cm cell culture dishes at a density of 4 × 10⁶ cells per dish in a complete growth medium (DMEM-F12, 10% FBS, 1% P/S). After 24 h, cells were labeled with a pacChol (Sigma-Aldrich) with a final concentration of 6 μM for 30 min at 37 °C and 5% CO₂. As a control, 0.096 v/v% DMSO was used. After 2 washing steps with phosphate-buffered saline (PBS) supplemented with 1mM MgCl₂ and 0.1 mM CaCl₂, UV crosslinking was performed using the BIO-SUN device (Vilber Lourmant) with 5 J/cm² for 20 min. Cells were lysed using 500 μl lysis buffer (PBS with 1% Triton X-100, 0.1% SDS, 2× protease inhibitor cocktail, 0.125 units/μl benzonase) per 10 cm dish for 1 h at 4 °C on a rotary wheel. The lysate was centrifuged for 15 min at 4 °C with 16,000 × g. 39 μl Biotin click reaction working solution (1,000 μM CuSO₄, 100 μM Biotin-azide, 1,000 μM TCEP, 100 μM TBTA) was added to 500 μl of lysate supernatant and incubated for 3 h at 37 °C on a shaker with 1,000 rpm. Click-reaction was stopped by adding 4 ml of ice-cold methanol. The sample was centrifuged for 20 min at 4 °C with 3,000 × g. The supernatant was discarded, and the pellet was washed 2 times with ice-cold methanol and subsequently air-dried. Pellet was resuspended in 15 μl of 4% SDS in PBS and dissolved by sonication. The sample was diluted 1:40 in PBS with 1% Triton X-100 for further analysis. 20 μl high capacity NeutrAvidin (Sigma-Aldrich) agarose beads were added to 600 μl sample and incubated overnight at 4 °C. The sample was centrifuged for 3 min at 4 °C with 3,000 × g. Beads were washed 3 times with PBS supplemented with 1% Triton X-100. The sample was eluted with 20 μl Laemmli buffer and further analyzed by immunoblotting using anti-IFITM3 (1:2,000) and anti-Caveolin1 (1:1,000) antibodies on a pre-cast 10 – 20% Tricine gel (ThermoFisher Scientific). The 'Precision Plus' (Bio-Rad) prestained protein size marker was used.

Molecular dynamics simulations

The initial IFITM3 structure (residues 59 – 133) and its orientation in the membrane was kindly provided by Emma H. Garst.²¹ IFITM3 was inserted into model membranes using the CHARMM-GUI Membrane Builder web interface.^{86,87} First, the palmitoyl group was added at Cys72 during the membrane builder system building process. Next, several potassium or chloride atoms were added to neutralize the systems. Finally, KCl salt at a concentration of 150 mM was added to mimic the intracellular environment. Protein, lipids, and salt ions were described using the CHARMM36m force field.^{88–90} For water, we used the TIP3 model.⁹¹

Equilibration of the systems was conducted with CHARMM-GUI standard protocol. Briefly, all the systems were subjected to energy minimization using the steepest descent algorithm. After minimization, we ran six steps of equilibration runs where we gradually reduced the force constant applied to restrain the positions of the protein and the lipids. For the production run, we employed the Parrinello-Rahman barostat⁹² with a semi-isotropic pressure coupling scheme and a time constant set to 5.0 ps to maintain the pressure constant. The pressure was set to 1.0 bar and the isothermal compressibility to 4.5 × 10⁻⁵ bar⁻¹. The temperature was maintained at 310 K using the Nose-Hoover thermostat^{93,94} with a time constant of 1.0 ps. Electrostatic interactions were handled using the PME method.^{95,96} The cut-off length of 1.2 nm was used for electrostatic (real space component) and van der Waals interactions. Hydrogen bonds were constrained using the Lincs algorithm.⁹⁷ Finally, periodic boundary conditions were applied in all directions.

The simulations were carried out using an integration time step of 2 fs with coordinates saved every 100 ps. Due to the presence of 8 different lipid types, the late endosomal-like membrane systems were simulated for 6 microseconds, whereas the binary and tertiary lipid mixtures were simulated for 1 microsecond. All simulations have been carried out using the GROMACS-2021 software.⁹⁸ The images were rendered using VMD.⁹⁹

Late endosomal membrane composition

The evaluation of the lipid composition in the late endosome is highly inaccurate and should be considered a rough estimation since the lipid composition changes as the endosome matures. Moreover, the ILVs and the limiting membrane have different lipid compositions.¹⁰⁰ The cholesterol/phospholipids ratio decreases from 1/1 at the early endosome to 1/2 in the late.³⁰ The major phospholipids head groups in the late endosome are²⁹ phosphatidylcholine (PC) 48.2%, phosphatidylethanolamine (PE) 19.8%, lysobisphosphatidic acid (LBPA) 15.7%, Sphingomyelin (SPH) 9.2%, phosphatidylinositol (PI) 4.1% and phosphatidylserine (PS): 2.4%. The level of acyl chain saturation is unknown in the late endosome, so we estimate it based on the known values in the plasma membrane.¹⁰¹ The majority of LBPA tails, which is not present in the plasma membrane, are 18:1 (~ 92%).²⁹ Finally, the percentage of lysolipids (excluding LBPA) is about 4 – 5% in all the cell organelles examined.¹⁰² The used late endosomal-like lipid composition used for MD simulation is summarized in the following table:

Complex lipid composition mimicking the late endosomal membrane:

Abbreviation	Full name	Mole percent	Intrinsic curvature	References for intrinsic curvature
POPC	1-palmitoyl-2-oleoyl-sn-glycero-3-phosphocholine	35.1	-0.02	Kollmitzer et al. ¹⁰³
POPE	1-palmitoyl-2-oleoyl-sn-glycero-3-phosphoethanolamine	7.3	-0.32	Kollmitzer et al. ¹⁰³
DOPE	1,2-dioleoyl-sn-glycero-3-phosphoethanolamine	7.3	-0.35	Fuller and Rand ¹⁰⁴
PSM	Palmitoylsphingomyelin	5.3	-0.13	Kollmitzer et al. ¹⁰³
LBPA	Lysobisphosphatidic acid	9.9	Negative, exact value unknown	Kobayashi et al. ²⁹
CHOL	Cholesterol	29.8	-0.5	Kollmitzer et al. ¹⁰³
LPC16	Lysophosphatidylcholine	4.0	0.15	Fuller and Rand ¹⁰⁴
LPE16	Lysophosphatidylethanolamine	1.3	0.03	Fuller and Rand ¹⁰⁴

Enrichment/Depletion analysis

For enrichment/depletion analysis, we calculate the number of lipids (for each lipid type) within a radial cut-off distance of 0.4. In addition, the molar fractions of lipids surrounding IFITM3 have been calculated with respect to the lipid bulk concentrations (lipids above the radial cut-off distances). The analysis was carried out employing the 'gmx select' and in-house python scripts. The first 20 ns have been considered as equilibration time and then excluded from the analysis. The standard deviation is reported in the error bar with $n = 3$.

Normalized contact occupancy

Over time, the number of contacts has been calculated using the 'gmx mindist' GROMACS analysis tool. A contact is defined if the distance between any atoms of IFITM3 and POPC (or cholesterol) is less than 0.4 nm. Data are normalized based on the total number of lipids of each lipid type. The first 200 ns have been considered as equilibration time and then excluded from the analysis. The error bar is shown as the standard deviation.

Relative affinity and repulsion of lipid to IFITM3

We calculate the relative affinity and repulsion of different lipid species to IFITM3 by considering the two competing forces governing the lipid distribution – the direct interaction between lipid to IFITM3 and the demixing entropy that resists it. To do so, we use the following assumptions: Each monolayer is composed of M number of different lipid species, and each lipid species has n_j lipids in each monolayer. No lipid flip-flop was observed during the MD simulations; therefore, we prohibit it in the following derivation. We define two regions in each monolayer – the immediate vicinity of the IFITM3 (Figure 2B, green) and the bulk (Figure 2B, orange), given by the superscripts b (bound) and f (free), respectively. Lipids can freely diffuse between the regions, but since the lipids are closely packed and have a high stretching-compression modulus, we assume their density and number in each region are fixed, N^b and N^f , respectively. Therefore, the free energy can only be relaxed by lipid exchange between the bound and free regions, Δn_j , which must satisfy the following requirement:

$$\sum_{j=1}^{j=M} \Delta n_j = 0. \quad (\text{Equation 1})$$

The total free energy that is associated with the lipid's interaction energy with IFITM3 and mixing entropy is given by

$$F = \sum_{j=1}^{j=M} \left[n_j^b \left(u_j + k_B T \cdot \ln \frac{n_j^b}{N^b} \right) + k_B T \cdot n_j^f \cdot \ln \frac{n_j^f}{N^f} \right]. \quad (\text{Equation 2})$$

To find the equilibrium distribution, we minimize Equation 2 with respect to Δn_j while maintaining the constraint of a fixed number of lipids and Equation 1, which can be done numerically. However, MD simulations found that most lipid exchange is due to cholesterol repulsion from IFITM3. Therefore, we consider cholesterol exchange with all of the other lipids combined. With that, Equation 2 is minimized by allowing only the exchange of Δn cholesterol with any other lipid. The relative repulsion of cholesterol is given by

$$\Delta u = u_{Chol} - u_0 = k_B T \ln \left[\frac{n_{Chol}^f \cdot N^b - n_{Chol}^b}{n_{Chol}^b \cdot N^f - n_{Chol}^f} \right] \quad (\text{Equation 3})$$

with $n_{cho}^{b,f}$ and $N^{b,f}$ the number of cholesterol and the total number of lipids in the free or bound areas (donated by the super-script b or f), respectively. u_0 is the averaged interaction energy of IFITM3 with all other lipids except cholesterol and u_{cho} is the interaction energy with cholesterol. This procedure is performed separately on the luminal and cytosolic facing and monolayers to find the relative repulsion of each, Δu_l and Δu_c , respectively. We also performed this procedure on the two monolayers combined to find the relative repulsion of cholesterol to IFITM3 in the membrane.

Modeling of membrane fusion and lipid sorting

Membrane elasticity theory

We use a continuum approach based on lipid tilt and splay theory to model the lipid deformations in the hemifusion diaphragm and its vicinity. Previous works present the theory and related computations in detail.^{32–34,105} In short, the hemifusion diaphragm is modeled as a membrane surrounded by the virus and endosome membranes, and the diaphragm rim represents the merger of the three (Figure 6A). Each membrane comprises two lipid monolayers that contact along a joint mid-plane. The deformation of the lipids in each monolayer is described by their tilt, splay, and saddle-splay.^{39,40} All are defined with respect to the monolayer dividing plane. Here we take the distance from the membrane mid-plane to the monolayer dividing plane to be $\delta = 1.5 \text{ nm}^{106}$ and explicitly assume that they are parallel.

Lipid tilt deformation is generated due to the shearing of the hydrocarbon tails in the vicinity of the diaphragm rim. It is defined as $\vec{t} = \frac{\vec{n}}{\vec{n} \cdot \vec{N}} - \vec{N}$, with \vec{n} the lipid director and \vec{N} the normal to monolayer dividing plane,³⁹ as presented in Figure 3C. Splay deformations originate from the curvature deformations and the lateral change of the lipid tilt.^{39,107} Mathematically, the lipid splay tensor is defined as the covariant derivative of the lipid director, $\tilde{b}_\alpha^\beta = \nabla_\alpha n^\beta$, where the sub- and superscripts denote, respectively, the co- and contravariant components in the local coordinate basis of the monolayer dividing plane and Hamm and Kozlov.³⁹ Lipid splay is the trace of the splay tensor, defined as $\tilde{J} = \tilde{b}_\alpha^\alpha$, where the summation is performed over repeating indices. In the absence of tilt, lipid splay has the meaning of the sum principal curvatures, c_1 and c_2 , referred to as total curvature, $J = c_1 + c_2$. Similarly, lipid saddle-splay is a generalization of Gaussian curvature, $K = c_1 \cdot c_2$, in the presence of both bending and tilt deformations. In co-contra variant form, it is the determinant of the splay tensor,³⁹ $\tilde{K} = \det \tilde{b}_\alpha^\beta$. The elastic energy density is given by

$$f_m = \frac{1}{2} \kappa_m (J^2 - 2\tilde{J}J_{sm}) + \bar{\kappa}_m \tilde{K} + \frac{1}{2} \kappa_t \vec{t}^2 \quad (\text{Equation 4})$$

with κ_m , κ_t and $\bar{\kappa}_m$ the monolayer's bending, tilt, and saddle-splay rigidities, respectively. Their values are estimated from the literature to be $14.4 \text{ k}_B T$,¹⁰⁸ $-7.2 \text{ k}_B T$,^{109,110} and 40 mN/m ,^{111,112} respectively. The spontaneous monolayer curvature, J_{sm} , is determined by the monolayer constituting lipids and proteins intrinsic curvatures, ζ_j , and their relative mol fractions, ϕ_j . With j being index representing the different components. The overall spontaneous monolayer curvature is the sum of its components^{103,113,114}

$$J_{sm} = \sum \zeta_j \phi_j. \quad (\text{Equation 5})$$

However, since IFITM3 is strongly repelling cholesterol, we consider the membrane to be composed of just two lipid subgroups – cholesterol with intrinsic curvature of $\zeta_{cho} = -0.5 \text{ nm}^{-1}$ and all of the other lipid species grouped have the mean intrinsic curvature of $\zeta_0 = -0.1 \text{ nm}^{-1}$, we term the second group 'background' lipids.

The overall elastic energy is found by integrating the energy density in Equation 4 over the area of the monolayers

$$U_E = \int_{all} f_m dA - U_e^{pre} \quad (\text{Equation 6})$$

The elastic energy is with respect to the pre-fusion configuration of two flat non-interacting membranes, U_e^{pre} . The equilibrium shape of the fusion site is found by minimizing Equation 6, as explained in the following.

IFITM3-induced lipid sorting

In addition to lipids, the endosomal membrane contains uniformly distributed IFITM3 proteins that repel cholesterol and attract other lipids. The virus and diaphragm membranes do not contain IFITM3 because the diaphragm rim acts as a semi-permeable barrier that

allows only lipids to pass. The formation of the IFITM3-free region allows the system to relax some of the relative repulsion energy between cholesterol and IFITM3 at the cost of entropic demixing energy.

To calculate the magnitude of exchange, we consider two membrane domains with a total of N lipids. One domain represents all the lipids that are closely bound to IFITM3 with $N^b = N_{IFITM3} \cdot n_{inter}$ lipids, N_{IFITM3} is the total number of IFITM3 proteins in the endosome and n_{inter} the number of lipids interacting with each, as found in MD simulations ($n_{IFITM3} = 52$ was used in all simulations as the value found in the ‘late endosome composition’). The second domain contains the remaining lipids $N^f = N - N^b = N - N_{IFITM3} \cdot n_{inter}$. As explained above, we consider two subgroups of lipids: N_{chol} cholesterol lipids and $N_0 = N - N_{chol}$ background lipids. The relative repulsion of the two to IFITM3 is $\Delta u = u_{chol} - u_0$. The number of cholesterol lipids is n_{chol}^f and the number of background lipids is $n_0^f = N^f - n_{chol}^f = N - N_{IFITM3} \cdot n_{inter} - n_{chol}^f$ in the free domain. The lipid numbers in the bound domain are $n_{chol}^b = N_{chol} - n_{chol}^f$ and $n_0^b = N^b - n_{chol}^b = N_{IFITM3} \cdot n_{inter} - N_{chol} + n_{chol}^f$. To find the equilibrium distribution, one can use a similar procedure leading to Equation 3 to have

$$\Delta u = k_B T \ln \left[\frac{n_{chol}^f}{N_{chol} - n_{chol}^f} \cdot \frac{N_{IFITM3} \cdot n_{inter} - N_{chol} + n_{chol}^f}{N - N_{IFITM3} \cdot n_{inter} - n_{chol}^f} \right]. \quad (\text{Equation 7})$$

We define the mole fractions: $\phi_{IFITM3} = N_{IFITM3}/N$, $\phi_{chol} = N_{chol}/N$, and $\phi_{chol}^f = n_{chol}^f/N^f = n_{chol}^f/(N - N_{IFITM3} \cdot n_{inter})$ and rewrite Equation 7 as

$$\Delta u = k_B T \ln \left[\frac{\phi_{chol}^f}{1 - \phi_{chol}^f} \cdot \frac{\phi_{IFITM3} \cdot n_{inter} - \phi_{chol} + \phi_{chol}^f (1 - \phi_{IFITM3} \cdot n_{inter})}{\phi_{chol} - \phi_{chol}^f (1 - \phi_{IFITM3} \cdot n_{inter})} \right]. \quad (\text{Equation 8})$$

The total cholesterol mole fraction is estimated based on the known literature to be $\phi_{chol} = 0.3$ in the late endosome,³⁰ Δu is found based on the MD simulation as described above and ϕ_{IFITM3} is the free parameter of the model. We find ϕ_{chol}^f by rearranging Equation 8 and solving the quadratic equation

$$\phi_{chol}^2 (1 - \phi_{IFITM3} \cdot n_{inter}) \left(1 - e^{-\frac{\Delta u}{k_B T}} \right) - \phi_{chol}^f \left[1 - \phi_{IFITM3} \cdot n_{inter} \left(1 - e^{-\frac{\Delta u}{k_B T}} \right) + \phi_{chol} \left(1 - e^{-\frac{\Delta u}{k_B T}} \right) \right] + \phi_{chol} = 0. \quad (\text{Equation 9})$$

The magnitude of lipid exchange is defined as the change of cholesterol level from the baseline levels with no IFITM3 in the endosome $\Delta \phi = \phi_{chol}^f - \phi_{chol}$.

Next, we derive the spontaneous curvature in the endosome, virus, and diaphragm monolayers. Since the relative affinities of lipids to IFITM3 are similar on the luminal and cytosolic sides, we consider the magnitude of the lipid exchange to be the same in both leaflets. In addition, because the typical time in hemifusion is in the order of seconds while the flip-flop time of cholesterol is measured in milliseconds, we also assume the system to be in equilibrium with respect to lipid flip-flop.

The virus and hemifusion diaphragm have the lipid composition of the ‘free’ domain, and their monolayer spontaneous-curvature is (Equation 5)

$$J_{sm}^{v,d} = (1 - \phi_{chol}^f) \zeta_0 + \phi_{chol}^f \zeta_{chol}. \quad (\text{Equation 10})$$

The endosomal membrane contains patches of both free and bound domains since IFITM3 proteins are dispersed in it. However, since the IFITM3 freely diffuse and are uniformly distributed, the lipids are also uniformly distributed on time-average. So, although IFITM3 triggers a local change in lipid composition in its immediate vicinity (< 1 nm), we treat the endosomal membrane as a smooth continuum and average over these spatial fluctuations. Moreover, we also consider the endosomal membrane much larger than the virus, so the enrichment of cholesterol in the virus has a negligible effect on the cholesterol mole fraction in the endosome. Lastly, we account for possible intrinsic curvature of the amphipathic helix domain of IFITM3 that was recently reported²³ in the ‘with sorting and curvature’ and ‘no sorting; with curvature’ scenarios. Specifically, we attribute the intrinsic curvature of $\zeta_{IFITM3}^c = -0.62 \text{ nm}^{-1}$ to the cytosolic side because there the amphipathic helices are located.²³ Given all of that, the endosome cytosolic facing monolayer spontaneous-curvature is (Equation 5)

$$J_{sm}^{c,endo} = \zeta_0 (1 - \phi_{chol} - \phi_{IFITM3}) + \zeta_{chol} \phi_{chol} + \zeta_{IFITM3} \phi_{IFITM3}. \quad (\text{Equation 11})$$

Here we also assumed for simplicity that the amphipathic helix domain has the same projected area as a lipid. The luminal-facing side of IFITM3 contains a transmembrane domain, which does induce any curvature to our knowledge. Therefore, the endosome luminal-facing monolayer spontaneous curvature is (Equation 5)

$$J_{sm}^{l,endo} = \zeta_0 (1 - \phi_{chol} - \phi_{IFITM3}) + \zeta_{chol} \phi_{chol}. \quad (\text{Equation 12})$$

In the ‘with sorting; no curvature’ scenario, we set $\zeta_{IFITM3} = 0$. We also tested the possibility that the amphipathic helices of IFITM3 penetrate the hemifusion diaphragm. In such a case, there is no sorting. The monolayer spontaneous-curvature of the diaphragm cytosolic facing monolayer is equivalent to the endosomal one.

Pore Expansion energy barrier and first passage time
The magnitude of fusion-pore formation energy barrier

A membrane pore must open and expand in the hemifusion diaphragm to complete the fusion reaction.^{115,116} The driving force for fusion pore expansion is the removal of lipids from the highly stressed region in the diaphragm and their migration to the more relaxed surrounding membrane. The energy gained by this process is given by

$$U_{removal} = \int (f_{Dia}^l + f_{Dia}^c) \cdot dA \quad \text{(Equation 13)}$$

with f_{Dia} being the position-dependent energy density in the diaphragm monolayers (Equation 4). The superscripts l and c represent the diaphragm luminal and cytosolic facing monolayers, respectively. The integral in Equation 13 is done over the pore area of size A . The fusion pore expansion is resisted by the energetic cost of forming the pore rim, $U_{pore\ rim} = \lambda L$, with λ to pore rim line tension and L the pore rim length. The line tension depends strongly on the lipid composition. In a two-lipid component system, the effect of the relative mol fraction change, $\Delta\phi$, is given by¹¹⁷

$$\lambda = \lambda_0 - \pi\kappa_m(\zeta_{chol} - \zeta_0)\Delta\phi. \quad \text{(Equation 14)}$$

The first term in Equation 14, λ_0 , accounts for the contribution to line tension independent of change in lipid composition. It includes all the other lipid deformations in the pore rim. Its value is estimated as $\lambda_0 = 15$ pN for a membrane containing 30% cholesterol based on theoretical considerations¹¹⁵ and experiments.³⁷ The energy needed for pore expansion is the sum of the energy cost of creating the pore rim and the energy gained by the removal of lipids (Equations 13 and 14)

$$E_{pore} = U_{pore\ rim} - U_{removal} \quad \text{(Equation 15)}$$

The pore-opening energy, E_{pore} , is characterized by the critical pore radius, ρ^* , smaller pores tend to close while larger tend to expand infinitely (Figure 3E). The energy of pore expansion at the critical size is the pore expansion energy barrier,

$$E^* = \max[E_{pore}] \quad \text{(Equation 16)}$$

The dwell time in hemifusion

Thermal fluctuations determine the dynamics of the pore size; small pores flicker in size until they eventually reach the critical size beyond which they irreversibly expand.¹¹⁸ The mean time needed for the pore size to cross the energy barrier was already described in detail in earlier works, primarily for uniformly stressed membranes¹¹⁹ but also in the specific case of pores in the hemifusion diaphragm³⁴

$$\tau = \tilde{\tau} \cdot e^{\frac{E^*}{k_B T}} \quad \text{(Equation 17)}$$

with $\tilde{\tau}$ being a pre-exponent factor that depends on an unknown microscopic time constant. We evaluate the efficiency of IFITM3 in inhibiting fusion by calculating the ratio between the typical time for pore expansion with and without IFITM3, τ_{IFITM3} and τ_0 respectively

$$\beta = \frac{\tau_{IFITM3}}{\tau_0} = \exp\left(\frac{E_{IFITM3}^* - E_0^*}{k_B T}\right) \quad \text{(Equation 18)}$$

Here we assume that $\tilde{\tau}$ is unchanged by slight changes in lipid composition, and the change in the diaphragm area available for fusion is negligible. We term β as the ‘inhibition factor’ and the difference in pore expansion energy barrier due to IFITM3 presence as $\Delta E^* = E_{IFITM3}^* - E_0^*$.

Numerical computation

Our computation aims to estimate the inhibition factor of IFITM3. The computation is divided into two steps. First, we calculate the equilibrium shape of the hemifusion diaphragm by minimizing Equation 6 using an iterative approach. The membranes’ mid-planes and tilt angles are gradually changed until minimal energy configuration is found. The geometry of the fusion site is described by the junction angles (Figure 3A), φ_v and φ_c , the diaphragm size R_D , fusion site size at the virus and endosome sides R_r^{endo} and R_r^v , and the distance between the virus and endosome, h , is also subjected to energy minimization. The process is repeated from different initial configurations to ensure that minimal energy is genuinely found.

Next, based on the resulting equilibrium configuration and the adjusted lipid composition in the diaphragm, we calculate the energy barrier of pore expansion, ΔE^* , (Equation 16), and the inhibition factor β (Equation 18). The pore is more likely to initially form close to the diaphragm rim, where the stress is maximal. However, our computations show that the critical pore size is comparable to the size of the diaphragm, making the energy barrier mostly independent of the starting position. Therefore, to facilitate the computations, we assume that the fusion pore growth starts at the center of the diaphragm and radially expands. We also assume that the diaphragm’s shape is unaffected by the growth of the pore. All computations are done using self-written MATLAB code, which is available on GitHub (https://github.com/GonenGolani/Fusion_Solver).

In situ cryo-correlative light and electron microscopy (cryo-CLEM)

In situ cryo-CLEM was performed on cryo-FIB milled samples based on a previously established method,^{42,48} as described below:

Sample preparation

1.8 × 10⁵ A549 or A549-IFITM3 cells were seeded on glow-discharged 200 mesh gold grids with a holey SiO₂ film with R1/4 spacing (Quantifoil) placed in a 35 mm dish and cultured in 2 ml complete growth medium (DMEM-F12, 10% FBS, 1% P/S). To facilitate grid handling, the 35 mm dish was coated with polydimethylsiloxane Sylgard 184 (Dow Corning) as described in Klein et al.⁴² The next day, cells were infected with fluorescently labeled IAV (A/WSN/1933-nDiO) using an MOI of 200. Virus stock was diluted to a final concentration of 5 × 10⁶ PFU/ml in the infection medium (DMEM-F12, 20 mM HEPES). EM grids were blotted on filter paper (Whatman No. 1) and placed on Parafilm. 20 μl of the virus dilution was added onto the grid and incubated for 30 min at 12 °C on a cooling plate to allow viral cell attachment. EM grid was washed 5 times with infection medium and was subsequently incubated for 1 h at 37 °C, 5% CO₂ in the complete growth medium, supplemented with 100 nM Lipi-Blue (Dojindo) to fluorescently label lipid droplets. 1 hpi, infected cells were washed 2 times with complete growth medium, grids were manually blotted on filter paper (Whatman No. 1) and a defined volume of 3 μl complete medium was added to the grid to ensure identical blotting conditions. Grid was subsequently blotted and vitrified by plunge freezing in liquid ethane using the EM GP2 automated plunge freezing device (Leica) using the following settings: 70% air humidity, 25 °C air temperature, -183 °C ethane temperature, 3.5 sec blotting from the back using a filter paper (Whatman No. 1).

Cryo-light microscopy (cryo-LM)

Fluorescent signal of the plunge frozen samples were acquired on the cryoCLEM wide-field microscope (Leica Microsystems)¹²⁰ equipped with a 50x/0.9 NA objective. A 1.2 × 1.2 mm area of the center of each grid was mapped, acquiring a volume stack of 30 μm thickness with a Z-spacing of 300 nm using the LAS X Navigator software (Leica). Image stacks were deconvolved with AutoQuant X3 (Media Cybernetics) using a theoretical and adaptive point spread function (PSF) for 100 iterations with the following parameters: lens immersion refractive index 1; sample embedding refractive index 1.31; sample distance from coverslip of 0 nm; emission wavelength of 460 nm (for Lipi-Blue) or 525 nm (for nDiO) and appropriate settings for the used objective (NA 0.9; objective lens magnification 50x). For cryo-correlative light and electron microscopy (cryo-CLEM), lamellae were mapped again by cryo-LM after cryo-TEM and correlated with the cryo-TEM map of the lamella using the post-correlation cryo-CLEM toolbox.⁴²

Cryo-focused ion beam milling (cryo-FIB)

Samples were mapped by cryo-scanning electron microscopy (cryo-SEM) on an Aquilos dual-beam cryo-focused ion beam-scanning electron microscope (cryo-FIB-SEM) (Thermo Fisher Scientific) with a cryo-stage cooled to -180 °C. The cryo-LM map of the grid was correlated to the cryo-SEM map using the MAPS Software (Thermo Fisher Scientific).¹²¹ Infected cells were selected for milling. A protective organo-metallic platinum layer was applied for 5 sec to the grid and cells were milled gradually in 5 steps with a stage angle between 15° and 18° using a Gallium ion beam.¹²² The nominal thickness of the milled lamella at the last milling step was 150 nm. A milling pattern including micro-expansion joints was used to minimize lamella bending.¹²³

Cryo-electron tomography (cryo-ET)

Cryo-ET data was acquired on a Krios cryo-TEM (Thermo Fisher Scientific) operated at 300 keV equipped with a K3 direct electron detector (Gatan) and Quanta Gatan Imaging Filter (Gatan) with an energy slit set to 20 eV. Lamellae were mapped using SerialEM⁸⁴ at 8,700× (pixel spacing of 10.64 Å) using a defocus of -50 μm to localize multivesicular organelles which were selected for acquisition. Tilt series were acquired with SerialEM⁸⁴ using a dose-symmetric tilting scheme¹²⁴ with the zero angle set to 8° and a nominal tilt range of 68° to -52° with 3° increments using the following settings: Target focus of -3 μm, electron dose per record of 3 e⁻/Å² and a magnification of 33,000× (pixel spacing of 2.67 Å). Automated tilt series acquisition was performed in SerialEM⁸⁴ using the Navigator with either a realign-to-item function or scripts for Parallel Cryo Electron Tomography (PACE).¹²⁵

Tomogram reconstruction

Individual movie frames were split into even and odd and subsets were drift corrected using Motioncor2.¹²⁶ Even and odd datasets were reconstructed in parallel with identical settings in etomo as part of the IMOD software package⁸⁵ using patch tracking for tilt series alignment. CTF estimation and 3D CTF-correction were performed in etomo. Tomogram was reconstructed using weighted back projection with a simultaneous iterative reconstruction technique (SIRT)-like filter equivalent to 5 iterations and dose-weighting filter. Denoising was performed using the reconstructed tomograms from the even and odd datasets employing the Noise2Noise algorithm implemented in the CryoCare software package¹²⁷ on non-binned data.

Volume rendering

The reconstructed and denoised tomogram volume was segmented in 3 dimensions using the Amira software (Thermo Fisher Scientific). First, a non-local means and membrane enhancement filter were applied. Membranes were automatically segmented using the Top-hat tool. The automated segmentation was manually refined by removing falsely segmented areas. In addition, missing parts of the limiting late endosomal membrane, ILVs and the viral membranes were manually segmented. The number of direct interactions between the viral particles and ILVs or the limiting late endosomal membrane were quantified.

Analysis of hemifusion symmetry

For each hemifusion site at the limiting late endosomal membrane or at ILVs in the endosomal lumen the length of the hemifusion diaphragm and the inner and outer angles (as defined in Figure 4A) were measured. The tomogram was resliced using the slicer tool in IMOD⁸⁵ to position the hemifusion site on a single X-Y plane. All individual angles were measured using the 'angle tool' in ImageJ/FIJI.⁷⁹ To measure the hemifusion diaphragm length, a line profile with 10 pixel width was plotted. The average signal of the late endosomal lumen was subtracted. The difference between the zero-crossing points was determined and reported as the diaphragm length. Thus, the measurement includes the phospholipid monolayers.

Estimation of pore formation energy barrier based on cryo-EM data

We use the theory described above to estimate the magnitude of the fusion-pore formation energy barrier based on the cryo-EM data. The stress in the diaphragm depends only on the geometry of the fusion site and specifically on the tilt magnitude at its rim, given by

$$t_0 = \tan\left[\frac{\pi - \varphi}{2}\right] \quad (\text{Equation 19})$$

With φ the inner angle of the fusion site either and the virus or cytoplasmic side (Figure 5A). Since we assume that the diaphragm is axially symmetric and no significant differences were observed between opposing angles, we take the inner angle as the average $\varphi_c = \frac{c+c'}{2}$ and $\varphi_v = \frac{b+b'}{2}$ (Figure 5B). The lipid tilt propagates towards the center of the diaphragm and vanishes at its center. The tilt radial dependence can be approximated³⁴

$$\vec{t}(\rho) = -t_0 \frac{I_1(l^{-1}\rho)}{I_1(l^{-1}R_D)} \hat{\rho} \quad (\text{Equation 20})$$

With I_n the modified Bessel functions of the first kind, ρ the radial coordinate, $l = \sqrt{\frac{\kappa_m}{\kappa_t}} = 1.2$ nm the tilt decay length. The diaphragm mid-plane radius, R_D , is related to the measured diaphragm diameter (Figure 5C) by $R_D = \frac{g-L}{2}$. With L the membrane thickness measured from headgroups to headgroups of opposing monolayers and g the distance between head groups at the diaphragm rim. We take L to be 6 nm based on our cryo-EM data. The change in tilt induces lipid splay, and saddle-splay is given by³⁴

$$\tilde{J} = -\frac{t_0}{2ll_1(l^{-1}R_D)} \left[l_0(l^{-1}\rho) + 2\frac{l}{r}I_1(l^{-1}\rho) + l_2(l^{-1}\rho) \right] \quad (\text{Equation 21})$$

$$\tilde{K} = \frac{t}{r} \frac{\partial t}{\partial r} = \frac{t_0^2}{2rl} \frac{I_1(l^{-1}r)}{I_1^2(l^{-1}R_D)} [l_2(l^{-1}\rho) + l_0(l^{-1}\rho)] \quad (\text{Equation 22})$$

We use Equations 19, 20, 21 and 22 to calculate the tilt, splay, and saddle-splay in each monolayer separately and the membrane stress using Equation 4. Finally, each fusion site's pore formation energy barrier is calculated using Equation 16.

Subtomogram averaging (STA)

To characterize the state of the influenza A fusion protein HA, which was regularly found at the hemifusion sites, we performed subtomogram averaging. In total, 30 individual putative HA densities at hemifusion sites were identified and extracted using a dipole model in Dynamo¹²⁸ using a box size of 192 pixel (equals 51.28 nm). An initial reference model was created by averaging all subvolumes with the orientations extracted by the dipole model. Azimuth angles were randomized to evenly distribute the missing wedge of the individual subvolumes during initial model creation. The first averaging was calculated without symmetry operation (C1) using a spherical mask (Figure S14A). The resulting average of the first STA was used as a new template for the second average, using a tight mask around the central density corresponding to the HA. In the second average, a C3 symmetry operation was applied (Figure S14B) and the same numerical parameters were used. An overview of used parameters can be found in the following table:

Numerical parameters for STA calculation in Dynamo.

	Round 1	Round 2	Round 3	Round 4
Iterations	1	1	1	1
References	1	1	1	1
Cone aperture [°]	120	30	10	2
Cone Sampling [°]	30	10	2	0.5
Azimuth rotation range [°]	360	90	30	5
Azimuth rotation sampling [°]	90	30	5	1
Refine	2	2	2	2
Refine factor	2	2	2	2
High pass filter [pixel]	2	2	2	2
Low pass filter [pixel]	32	32	32	32
Symmetry	C1 / C3	C1 / C3	C1 / C3	C1 / C3
Particle dimensions	192	192	192	192
Shift limits in X, Y and Z [pixel]	12, 12, 12	6, 6, 6	4, 4, 4	2, 2, 2

(Continued on next page)

Continued

	Round 1	Round 2	Round 3	Round 4
Shift limiting way	1	2	2	2
Separation in tomogram	0	0	0	0
Basic MRA	0	0	0	0
Threshold parameter	0.8	0.8	0.8	0.8
Threshold modus	5	5	5	5

An isosurface of the final average of the STA was created using USCF Chimera.¹²⁹ The post-fusion structure of HA2 (PDB: 1QU1)⁸ was fitted to the isosurface using the 'Fit in Map' function in USCF Chimera. The number of atoms inside and outside of the isosurface were quantified.

QUANTIFICATION AND STATISTICAL ANALYSIS

Image acquisition and quantification of ILV in late endosomes (Figures 1R–1Y) was done blinded. An unpaired T-test was utilized to analyze the significance of differences in the following figure panels: Figures 1H, 1Q, 1X, 1Y, S1C, S3C, and S3D–S3F. Paired T-test was utilized to analyze the significance of differences in the following figure panels: Figure 5B.